POLITECNICO DI MILANO

DEPARTMENT OF ENERGY

DOCTORAL PROGRAM IN ENERGY AND NUCLEAR SCIENCE AND TECHNOLOGY

DEVELOPMENT OF AN ADVANCED MULTI-DIMENSIONAL CFD FRAMEWORK FOR MODELING LOW TEMPERATURE COMBUSTION IN DIRECT INJECTION COMPRESSION IGNITION ENGINES

Doctoral Dissertation of:

Amin Maghbouli

Supervisors:

Prof. Gianluca D'Errico

Prof. Tommaso Lucchini

Tutor:

Prof. Angelo Onorati

The Chair of the Doctoral Program:

Prof. Carlo Enrico Bottani

2017 - XXIX Cycle STEN

"It's your road and yours alone ...

... Others may walk it with you, but no one can walk it for you."

Rumi*

*Jalal ad-Din Muhammad Rumi, known as $Mawlānā$, was a Persian poet.

Acknowledgments

It has been a quite long journey since I have started my PhD career and I am very lucky to meet, live, learn, and enjoy my time with my caring friends and esteemed professors. Initially, earnest thanks to Politecnico di Milano for providing me opportunity and financial support during my PhD studies.

I would like to sincerely appreciate my tutor Prof. Angelo Onorati for his very kind considerations even before starting my studies in PoliMi. His guidance and help during the PhD time was always full of enthusiasm and uplifting. My hearty acknowledgment goes to Prof. Gianluca D'Errico and Prof. Tommaso Lucchini, my supervisors, for their unlimited help, understanding, and teaching me state-of-art concepts of reacting flows and internal combustion engines. Thanks for spending your invaluable time, ideas, and directing my research during our uncountable number of meetings and discussions. I am very gifted to have supervisors and more importantly friends such as you.

My regards also go to the rest of teaching staff of our IC engine group in PoliMi. Prof. Ferrari, Prof. Montenegro, Prof. Piscaglia, Dr. Cerri, Dr. Della Torre, and Dr. Montorfano you are among the most qualified researchers I have ever met. Sincere thanks also go to our student union in IC engine group. I am very happy for making lifetime friends with Yan, Ehsan, Keyvan, Roberto, Javier, Lorenzo(s), Isabella, Filippo, Davide, Luca and Marco. Without your help and understanding this could not reach to an end.

Also, I am thankful to my former supervisors: Prof. Yang Wenming, Prof. Siaw Kiang Chou and Dr. An Hui from National University of Singapore for their support and encouragements to pursue my PhD studies.

During my PhD I have connected to Engine Combustion Network (ECN) research through very kind and helpful people. Special thanks go to Dr. Louis-Marie Malbec from IFPEN and Dr. Mark Musculus and Dr. Ethan Eagle from Sandia National Labs. Thanks for sharing experimental data with me and for your insightful help and time on our participation in ECN Spray B topic and joint publications.

I am very grateful to Prof. Bart Somers from Eindhoven University of Technology during my PhD visiting period. His insightful help and ideas for research on low temperature partially premixed combustion is highly appreciated. Prof. Philip de Goey and Prof. Jeroen van Oijen, thanks for your kind guidance and our discussions on my research matters. I would also like to thank my friends in TUe: Mohammad, Noud, Miao, Nard, Aromal, Denis, Yiğit, Berşan, Uğur, Shuli, Peter-Christian, Zhen, Marjan, and many others for being such amazing friends during my stay in Netherlands.

Last but not the least, I would like to express my highest gratitude to my beloved family. Mom, Dad, and my lovely Sisters, thanks for your enduring love and patience for this quite lengthy time I have not been home. Without your love, understanding, and support exploring this winding road was impossible. You are my favorite everything.

Abstract

The main objective of this work is to study combustion characteristics of reacting high pressure liquid sprays and compression ignition Diesel engines under conventional and low temperature operating modes by development of a robust computational framework. This has been done under RANS turbulence modeling methodology and Lagrangian Droplet Eulerian Flow formulations of multi-dimensional computational fluid dynamics modeling perspective.

Initially, Conical and Spray Oriented grids were introduced for non-reacting liquid spray simulations and noticeable enhancement of air-fuel mixing process and better representation of the scalar dissipation rates were depicted. It was shown that a reliable non-reacting simulation is the perquisite of accurate results for reacting liquid spray simulations. In this regard, uncertainties from the liquid spray simulations should be minimized. For instance, it was shown that occurrence of cavitation can highly alter the spray properties, breakup, evaporation, air-fuel mixing, and subsequent combustion. It was discussed for fuels that are more prone to cavitation, care must be taken both in experimental observation and measurements and numerical model selection and application.

Then attention was given to the reactive simulations of Engine Combustion Network *Spray A* and *Spray B* configurations. Two well known combustion closures, models based on well-mixed assumption and flamelet concept, with enhanced applicability were selected. After extensive validations over wide range of operating conditions in case of ambient temperature, density, oxidizer level, and injection pressures, a detailed

combustion phasing analysis and mathematical reasoning of observed model-to-model differences were made. Detailed discussions were carried out on how embedded Turbulence Chemistry Interactions (TCI) can enhance the ignition delay times and flame lift-off length and alter the combustion phasing mechanism compared to the closures without considering TCI.

Lastly, study was focused on modeling of Partially Premixed Compression Ignition (PPCI) engines as an advanced Low Temperature Combustion (LTC) mode. It was discussed how air-fuel mixture stratification levels can modify the history of pressure and heat release rate. Delay time between first and second stage combustion tends to reduce by further moving to high air-fuel mixture stratification levels. This can introduce much better control over PPCI combustion heat release once the engine needed thermal load was provided.

All the computational efforts in this work were implemented within the OpenFOAM® framework, as a contribution to the library *Lib-ICE*, developed by the Internal Combustion Engine Group of the Energy Department of Politecnico di Milano.

Sommario

L'obiettivo principale di questo lavoro è quello di studiare le caratteristiche del processo di combustione con spray liquidi in bomba ad alta pressione e nei motori Diesel sia in modalità di funzionamento convenzionali che a bassa temperatura, sviluppando una robusta metodologia numerica. Questo è stato fatto attraverso un approccio RANS per la soluzione della turbolenza e una formulazione Lagrangiana-Euleriana del flusso multi-dimensionale. Inizialmente, griglie coniche e orientate secondo lo spray sono stati introdotte per la simulazione di spray liquidi evaporanti non-reagenti e la valutazione del processo di miscelazione aria-combustibile e la distribuzione dello scalar dissipation rate.

È stato dimostrato che una affidabile simulazione del flusso non reagente è la prerogativa essenziale per accurati risultati delle simulazioni reagenti. A riguardo, le incertezze associate alle simulazioni del getto di liquido devono essere minimizzate. Per esempio, è stato dimostrato che il verificarsi della cavitazione durante l'iniezione del combustibile liquido può altamente alterare le proprietà del getto, la rottura, l'evaporazione, la miscelazione aria-carburante e la successiva combustione. Si è discusso come i combustibili che sono più inclini alla cavitazione richiedono opportune metodologie di analisi sperimentale e numerica.

L'attenzione poi è stata data alle simulazioni reagenti delle configurazioni *Spray A* e *Spray B* dell'Engine Combustion Network. Due ben noti modelli di combustione rispettivamente basati su ipotesi di miscelazione omogenea e flamelet sono stati selezionati. Dopo lunghe validazioni in una vasta gamma di condizioni operative con differenti

temperature ambiente, densità, ossigeno e pressioni di iniezione, una dettagliata analisi delle fasi di combustione e delle differenze dovute al modello scelta è stata svolta. Sono state condotte approfondite discussioni su come l'inclusione dell'interazione chimica-turbolenza possa migliorare la stima dei tempi di ritardo di accensione e del lift-off della fiamma ed influenzare il processo di combustione.

Infine, lo studio si è concentrato sulla modellazione di motori PCCI, con carica parzialmente premiscelata, una modalità avanzata di combustione a bassa temperatura (LTC). E' stato discusso come i livelli di stratificazione miscela aria-combustibile possano modificare l'evoluzione della pressione e del rilascio di calore. Il tempo di ritardo tra la prima e la seconda fase di combustione tende a ridurre adottando elevati livelli stratificazione della miscela aria-combustibile. Questo può permettere una migliore controllo del rilascio di calore di combustione a pari carico motore. Tutte le simulazioni numeriche di questo lavoro sono stati svolte usando il codice OpenFOAM®, includendo la libreria *Lib-ICE*, sviluppata dal gruppo di Motori a Combustione Interna del Dipartimento di Energia del Politecnico di Milano.

Publications

List of publications related to the discussed topics of reacting sprays and Diesel engine combustion:

- Maghbouli, A., Lucchini, T., D'Errico, G., Izadi Najafabadi, M., Somers, B.
  "Numerical and experimental investigation of PPCI combustion at extreme charge stratification levels"
  SAE World Congress, *submitted*, 2017.
- Maghbouli, A., Lucchini, T., D'Errico, G., Izadi Najafabadi, M., Somers, B.
  "Effects of Charge Stratification on Controllability of PPCI Engine Combustion"
  Applied Energy, *submitted*, 2017.
- Maghbouli, A., Lucchini, T., D'Errico, G., Onorati, A., Malbec, L.M., Musculus, M.P. and Eagle, W.E.
  "Parametric Comparison of Well-Mixed and Flamelet n-dodecane Spray Combustion with Engine Experiments at Well Controlled Boundary Conditions"
  SAE Technical Paper No. 2016-01-0577, 2016. DOI: 10.4271/2016-01-0577
- Maghbouli, A., D'Errico, G., Lucchini, T.
  "Numerical Modeling of Non-premixed Turbulent Spray Flames"
  36^{th} International Symposium on Combustion, August 2016, Seoul, South Korea, WiPP ID#: 1P112_7933.
- Maghbouli, A., Lucchini, T., D'Errico, G. and Onorati, A.
  "Effects of grid alignment on modeling the spray and mixing process in direct injection Diesel engines under non-reacting operating conditions"
  Applied Thermal Engineering. Vol. 91, pp.901-912. 2015. DOI: 10.1016/j.applthermaleng.2015.07.051
- Maghbouli, A., Lucchini, T., D'Errico, G. and Onorati, A.
  "Numerical Simulation of Non-reacting Diesel Fuel Sprays under Low Temperature Late Injection Operating Condition"
  Energy Procedia. Vol. 81, pp.960-966. 2015. DOI: 10.1016/j.egypro.2015.12.154

- Lucchini, T., Della Torre, A., D'Errico, G., Montenegro, G., Fiocco, M. and Maghbouli, A.
  "Automatic mesh generation for CFD simulations of direct-injection engines"
  SAE Technical Paper No. 2015-01-0376, 2015. DOI: 10.4271/2015-01-0376
- Maghbouli, A., Lucchini, T., D'Errico, G.
  "Tabulated Kinetics for Diesel Combustion Modeling: Preliminary validation with constant-volume and engine experiments"
  SAE 2016 - International Multidimensional Engine Modeling User's Group Meeting, 2016.
- Lucchini, T., D'Errico, G., Montenegro, G., Cerri, T., Della Torre, A., Maghbouli, A., Onorati, A.
  "Comprehensive validation of OpenFOAM based libraries for IC engine simulations with ECN test cases"
  SAE 2015 - International Multidimensional Engine Modeling User's Group Meeting, 2015.

Contents

List of Figures

List of Tables

CHAPTER 1

Introduction

1.1 Roles of Internal Combustion Engines

High dependence of transportation and power generation units on Internal Combustion (IC) engines now has reached over a century-long time span. In 2012, sixty million cars have been made in the globe, with the increase of a 50% over a decade ago [1]. The main motive factor for this trend is high thermal efficiency and high power output-to-volume ratio of the internal combustion engines. On the contrary, ever increasing fuel prices and depleting petroleum reserves have endangered their viability. IC engines are considered for contributing approximately one fourth of annual emitted greenhouse gases in the US as well as contributors of Nitric Oxides (NO_x) and Particulate Matter (PM) emissions. In this context, alternative power generation units and technologies such as fuel-cells and hybrid-automobiles do not seem to completely take the role of internal combustion engines in the near future. In case of Diesel engines, a considerable deal of research is concentrated both on introduction of new combustion modes to achieve Low Temperature Combustion (LTC) such as: Homogeneous Charge Compression Ignition (HCCI), Partially Premixed Compression Ignition (PPCI), Reactivity

Controlled Compression Ignition (RCCI) and on optimization of air fuel mixing and increasing combustion efficiency by applying higher injection pressures. Bio-fuels on the other hand, are introduced as sustainable energy sources and alternatives for fossil fuel [2,3]. These aspects should meet daily market's ever demanding high output power and noticeably strengthened emission legislation.

Diesel engines are used in light and heavy duty applications. In heavy duty applications, the most important factor that has caused Diesel engines to surpass gasoline engines, is their lower fuel consumption associated with high specific output power and torque. The modern optimized Diesel engines are 20-40% more fuel efficient than their gasoline counterpart. This improved efficiency is partly due to the fact that load control is achieved without throttling the intake air flow as is required in the stoichiometric SI engine, reducing breathing or pumping losses. In Diesel engines instead, load control is achieved by varying the amount of injected fuel into the cylinder. Despite the fact that Diesel engines fulfill the daily increasing power demand and seem to be a promising tool to achieve efficient fuel consumption, conventional Diesel cycle suffers from high levels of NO_x and Soot emissions at high engine loads, and low thermal efficiency and high levels of Unburned Hydro Carbon (UHC) emissions at lower engine load conditions [4]. This is why there has been a significant amount of researches worldwide to optimize and introduce new technologies in order to minimize emissions from Diesel combustion while providing acceptable output power. In near future, new generation of Diesel engines will directly benefit from engine downsizing techniques, improved direct-injection systems, advanced in-cylinder combustion phasing, and extended utilization of bio-fuels and additives. Hence, the foreseeable future of Diesel engine combustion system will become more challenging in optimization perspectives.

1.2 Experiments and Modeling of Diesel Engines

Engine experiments are expensive and difficult to perform in the belligerent engine environment. However, they are highly essential to provide insights into processes that can lead to engine optimization. Diagnostics methods such as Chemiluminescence and Planar Laser Induced Fluorescence (PLIF) [5] provide detailed information about in-cylinder spatial and temporal distributions of important species. By optical access to the combustion chamber, details of the flow field can be obtained using Particle Image Velocimetry (PIV) [6] or Phase Doppler Anemometry (PDA) [7] techniques for spray

drop size and velocity analysis. Engine experiments also provide valuable information for understanding engine processes. For instance, shock tube and rapid compression machine experiments [8] provide needed data about the ignition characteristics of fuels. Constant volume combustion vessel experiments provide information about spray vaporization, air-fuel mixing, spray ignition, flame lift-off and fuel effects on particulate (soot) formation and oxidation [9]. Initial and boundary conditions of such experiments are set to cover the regimes of temperature, mixture fraction, turbulence, pressure and composition (including Exhaust Gas Recirculation, EGR) of interest in internal combustion engines [10]. However, current experiments need further enhancements to provide quantitative data for critical areas such as dense Diesel spray near the injector orifice or OH^* and OH Chemiluminescence while ignition and lifted flame sequences, respectively.

Although experiments are essential tools to study, understand, and optimize engines, the range of their applicability in terms of economy, time and available infrastructures is the matter of debate. Nowadays, with the advent of powerful computers with high computational power, numerical modeling has proved to be a strong tool having flexibility and low cost. Generally speaking, the mathematical framework for engine modeling can be classified into two main groups: thermodynamic and Computational Fluid Dynamics (CFD) models. Thermodynamic models assume energy equation as the main conservation equation and are subdivided into single and multi-zone models [11–13]. The physical processes such as turbulent flow field are not modeled directly and instead, empirical correlations with numerous constants are used. In CFD models, temporal and spatial variations of the flow filed, pressure, composition, temperature and turbulence inside combustion chamber are accounted by *Transport Phenomena* [14]. In engine configuration (due to pretty large dimensions of the combustion chamber), it is impractical to solve governing conservation equations in all length and time scales. Hence, variety of sub-models are applied in the CFD models to simulate different aspects of in-cylinder processes such as turbulence, combustion, and etc. Among these, the combustion model has been found to be the most important one since it is directly related to in-cylinder pressure and Heat Release Rate (HRR).

Linking IC engine experimental and numerical research, Engine Combustion Network (ECN) [15] is an international forum which promotes collaborations among researchers with making publicly available a large set of experimental and numerical

data. The ECN experiments include well-defined boundary condition, standardized injectors, and compare results from various experimental and modeling approaches to enhance understanding of combustion in practical applications. ECN configurations for constant volume vessel and engine setups will be used in this thesis as experimental references.

1.3 Motivation, Objectives, and Strategy

As it was mentioned, despite the fact that emerging of Diesel engines dates back to over a century, there is still needed research on comprehensive understanding of their combustion and emission formation processes. This is mainly driven by two motive factors of limited fossil fuel resources and health and environmental awareness on emissions. Parallel to engine experiments, comprehensive CFD calculations with enhanced submodels are necessary in optimization purposes in ever limiting emission legislation. Introduction of the new advanced concepts in Diesel engines are mainly concentrated on different modes of Diesel combustion by increasing controllability over the heat release of the Diesel cycle and combustion phasing [16, 17]. Needed optimization in such modes requires a detailed understanding of underlying physical and chemical processes occurring while injection and combustion. CFD can effectively be used in such an aspect and provides useful tool on further optimization purposes.

Main objective of this thesis is paying a particular attention to the turbulent combustion models under non-premixed turbulent combustion configurations. In particular, differences of turbulent combustion closure with and without considering Turbulence-Chemistry Interactions (TCI) and its role on modeling non-premixed and Low Temperature Combustion (LTC) will be highlighted and quantitatively shown by numerical simulation results. Numerical platform for all the modeling and simulations throughout the thesis is based on OpenFOAM® technology [18] and Lib-ICE [19, 20] which is a set of source code libraries and solvers for simulation of gas exchange, liquid spray, air-fuel mixing and combustion for variety of experimental configurations developed in ICE Group of Politecnico di Milano.

1.4 Structure of the Dissertation

Thesis is mainly divided to two parts of theory and applications. In the first part, Chapters 1 to 3, after an introduction in the first chapter, needed fundamentals on turbulent

combustion and liquid spray modeling are discussed in the second Chapter. Chapter 2 is also for mathematical description and modeling assumptions of the applied spray sub-models and turbulent combustion closures. Numerical framework for model development, implementation and their use is discussed in Chapter 3. Second part of the thesis, Chapters 4 to 7, is for representing the modeling results for practical combustion configuration and experimental validation. Chapter 4 is for the results of non-reacting sprays as the perquisite for reacting conditions. Results of Multi-Zone Well-Mixed (MZWM) and Multiple Representative Interactive Flamelet (MRIF) models for *Spray A* constant volume vessel and *Spray B in engines* are discussed and compared in Chapter 5 and 6, respectively. Chapter 7 further discusses numerical modeling efforts on the new concepts of LTC such as HCCI and PPCI modes. Finally, Chapter 8 provides conclusions of the thesis and implications for the future studies.

CHAPTER 2

Fundamentals

Numerical modeling of turbulent combustion within IC engines is a multi-discipline problem which involves wide variety of physical and chemical concepts. For numerical modeling and expecting reliable and valid results from simulations, sufficient knowledge of each concept is needed and then the main focus can be given to an specific part. This chapter tries to briefly address the main areas of interest in the field of turbulent combustion simulations with emphasis on IC engines.

2.1 Transport Phenomena for Reactive Fluid Flow

Transport phenomena in engineering problems is generally attributed to the steady or time dependent solution of a set of conservation equations for momentum and scalars together with additional auxiliary equations. In their instantaneous and spatially-resolved forms, these equations have very well-defined foundations and they represent a large number of problems that are encountered in a very broad range of engineering applications [21, 22].

For a general variable ϕ, the conservative form of all fluid flow equations, including

equations for scalar quantities such as temperature and chemical species concentrations and vector quantity such as velocity can be written in the following form:

$$\frac{\partial(\rho\phi)}{\partial t} + div(\rho \mathbf{u}\phi) = div(\Gamma grad\phi) + S_\phi \tag{2.1}$$

where ρ is gas phase density, *t* is time, ***u*** is velocity vector in x, y, and z dimensions of Cartesian coordinates, and S_ϕ is source term for variable ϕ. Equation 2.1 is so-called transport equation for property ϕ. It represents the various transport processes: the rate of change ϕ and the convective term on the left hand side and the diffusive term and the source term (due to Combustion, Spray, and etc.) respectively on the right hand side. In this context conservation of mass, momentum and energy for compressible flow of a reactive spray can be written as below:

• Conservation of mass:

$$\frac{\partial \rho}{\partial t} + div(\rho \mathbf{u}) = \dot{\rho}^{Spray} \tag{2.2}$$

• Conservation of species mass fractions:

$$\frac{\partial \rho Y_i}{\partial t} + div(\rho \mathbf{u} Y_i) - div(\mu \; grad \, Y_i) = S^{Spray} + S^{Combustion} \tag{2.3}$$

Y_i is mass fraction of *i* chemical specie, μ is dynamic viscosity and on S^{Spray} and $S^{Combustion}$ are the source terms due to liquid spray and combustion, respectively.

• Conservation of momentum:

$$\frac{\partial(\rho \mathbf{u})}{\partial t} + div(\rho \mathbf{u}\mathbf{u}) + \frac{\partial p}{\partial \mathbf{x}} - div(\mu \; grad \, \mathbf{u}) = F^{Spray} \tag{2.4}$$

p is pressure and F^{Spray} is momentum exchange source with liquid spray.

• Conservation of energy:

$$\frac{\partial(\rho h)}{\partial t} + div(\rho \mathbf{u} h) - div(\alpha \; grad \; h) = \dot{Q}^{Spray} + \dot{Q}^{Combustion} + \frac{Dp}{dt} \tag{2.5}$$

h is enthalpy, α is the thermal diffusivity, and Q^{Spray} and $Q^{Combustion}$ are source terms due to cooling evaporation and enthalpy change due to combustion.

Large number of practical combustion devices are operating under turbulent flow conditions where after exceeding from critical Reynolds number, Re_{crit}, fluid flow will shift to turbulent flow which eventually leads to a radical change of the flow character.

The motion becomes intrinsically unsteady and velocity and all other flow properties vary in a random and chaotic way. In this condition velocity for instance can be decomposed into a steady mean value $\boldsymbol{U}$ with a fluctuating component $\boldsymbol{u}'(t)$ if RANS approach is applied. Mentioned conservation equations needed further derivation for turbulent conditions using time-averaged or density-weighted or Favre-averaged derivations on their all variables. This is not repeated here and the reader can refer to [23, 24].

2.2 Turbulence

Turbulence generates eddies in the flow with a wide range of length and time scales. In case if reactive flow, this is two-folded: First, turbulence increases the mixing processes and thereby enhances combustion. Second, combustion releases heat and thereby generates flow instability by buoyancy and gas expansion, which then enhances the transition to turbulence [25]. The methods to model or directly solve for turbulent flow time and length scales can be grouped into the following three categories:

2.2.1 Direct Numerical Simulation (DNS)

The most accurate approach to simulate both laminar and turbulent flows would be to solve the Navier Stokes equations directly on a discretized grid that is fine enough to resolve the smallest length scales of the flow problem. This method is called DNS and represents the simplest approach from a conceptual point of view. The smallest length scales are defined by the size of *Kolmogorov* eddies, that are important for dissipation of turbulent kinetic energy [23]. Kolmogorov length scale becomes smaller by increasing Reynolds number of the flow. For a typical Reynolds number within IC engines, DNS calculations require grid size about 10 μm and with additional time required for chemistry calculations, it is not feasible to conduct DNS simulations with available computational power. Nevertheless, DNS can be used to perform fundamental studies of the flame structure with lower Reynolds numbers and small scale configurations.

2.2.2 Large Eddy Simulation (LES)

LES is an intermediate form of turbulence calculations which tracks the behavior of the larger eddies. It involves space filtering of the unsteady Navier Stokes equations prior to the computations, which solves the larger eddies and rejects the smaller eddies. Consequently, the behavior of the smaller eddies needs to be described by appropriate

semi-empirical sub-models. This procedure seems reasonable since the large eddies contain the major fraction of energy and are much more important in the transport of the conserved quantities. The selection of the cutoff length scale is not straightforward as in many problems the Reynolds number and thus the characteristic length scales are not constant over the entire geometric domain. In simulation time perspective, while LES is less costly than DNS, it is still very expensive for IC engine simulations. However, LES is used to model reactive sprays in constant volume vessels [26–28].

2.2.3 Reynolds Averaged Navier Stokes (RANS)

In this approach attention is focused on the mean flow and the effects of turbulence on mean flow properties. Prior to the application of numerical methods, the Navier Stokes equations are time-averaged or Favre-averaged. Extra terms appear in the time-averaged flow equations due to the interactions between various turbulent fluctuations. These extra terms are modeled with classical turbulence models such as $k-\epsilon$ model. This model focuses on the mechanisms that affect the turbulent kinetic energy by considering a transport equation for turbulent kinetic energy, k, and its dissipation ϵ. RANS is the least time expensive method of determining turbulent flow characteristics and has been extensively applied in IC engine simulations [29–35].

Turbulence Length Scales

Number of length scales have been defined for turbulent flows, but here integral length scale and the Kolmogorov length scale are briefly discussed. Integral length scale, l, represents the mean size of the large eddies that contain most of the turbulent kinetic energy and can be correlated to the velocity fluctuations measured at x and $x + r$, where r is separative distance:

$$l = \int_0^\infty \frac{\overline{u'(x,t)u'(x+r,t)}}{\sqrt{\overline{u'^2(x,t)}}\sqrt{\overline{u'(x+r,t)}}}\, dr \tag{2.6}$$

and Kolmogorov length scale, η, corresponds to the size of the smallest eddies in a turbulent flow. In this scales viscous forces dominate and due to energy cascade concept turbulent kinetic energy of the eddies is dissipated into the heat. By dimensional analysis [36], η can be determined from the rate of kinetic energy dissipation, ϵ, and kinematic viscosity, ν as below:

$$\eta = (\frac{\nu^3}{\epsilon}) \tag{2.7}$$

This turbulent length scales will be later used to distinguish different combustion regimes and flame characteristics.

2.3 Liquid Sprays

2.3.1 Spray Equation

Diesel engine injectors today operate under considerably high injection pressures causing high speed liquid jets out of the injector orifice accelerating the droplets breakup. Small droplets will further travel inside the combustion chamber and due to drag forces and exposure to the hot surrounding gas will evaporate [37]. Schematic of number of processes happening while liquid fuel spray is illustrated in Fig. 2.1.

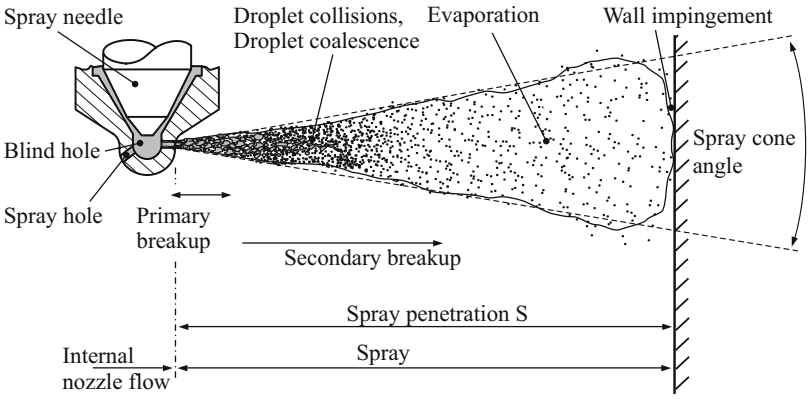

Figure 2.1: *Schematic illustration of processes while injecting a liquid fuel spray [37]*

Very close to the nozzle orifice an intact liquid core is present and then it rapidly disintegrates into ligaments (churning flow) and further down stream into droplets, where it still occupies a considerable fraction of the two-phase mixture. In immediate vicinity of the nozzle exit the spray is termed "thick" or dense, whereas further down stream of the injection axis, droplets become isolated and smaller in diameter. In this case, the spray is termed "thin" or dilute [38]. In a Diesel engine liquid fuel spray atomizes to couple of million droplets. Such a large number of droplets make it computationally impractical to resolve each single droplet in numerical simulations. Instead, statistical averaging technique becomes necessary with additional sub-models in order to describe the sub-scale processes. As formulated by Williams [39] the problem can be defined by

the so-called spray equation. Probable number of drops per unit volume at time *t*, that are located between location $\vec{x}$ and $\vec{x}$ + d$\vec{x}$ with corresponding velocities between $\vec{u}$ and $\vec{u}$ + d$\vec{u}$, a radius between rand *r* + d*r* and a temperature between T_{Liq} and T_{Liq} + dT_{Liq} is described with the probability density function *f*. Hence, probability of f can be written with its dependent parameters as below:

$$f = f(\vec{\mathbf{x}}, \vec{\mathbf{u}}, r, T_{Liq}, t)\, d\vec{\mathbf{u}}\, dr\, dT_{Liq} \tag{2.8}$$

Formulation above is based on the assumption that the droplets are ideally spherical and that their size or mass is thus explicitly defined by their radius *r*. However, in the vicinity of the injection orifice due to considerable relative velocity differences between liquid and gas phases (causing aerodynamic forces) droplet deviates from spherical shape. Two additional independent variables can be included as the distribution function: the droplet distortion parameter y and its temporal rate of change $\dot{y}$. Now f can be written again:

$$f = f(\vec{\mathbf{x}}, \vec{\mathbf{u}}, r, T_{Liq}, y, \dot{y}, t)\, d\vec{\mathbf{u}}\, dr\, dT_{Liq}\, dy\, d\dot{y} \tag{2.9}$$

The temporal and spatial evolution of the distribution function, spray equation [21], can be written as below:

$$\frac{\partial f}{\partial t} = -\frac{\partial}{\partial \vec{\mathbf{x}}}(f\vec{\mathbf{u}}) - \frac{\partial}{\partial \vec{\mathbf{u}}}(f\mathbf{F}) - \frac{\partial}{\partial r}(fR) - \frac{\partial}{\partial T_{Liq}}(f\dot{T}_{Liq}) - \frac{\partial}{\partial y}(f\dot{y}) - \frac{\partial}{\partial \dot{y}}(f\ddot{y}) + \dot{f}_{coll} + \dot{f}_{bu} \tag{2.10}$$

$\mathbf{F}$ denotes a force per unit mass, i.e. an acceleration. Thus the component $\mathbf{F}$ is the acceleration along the spatial coordinate $\vec{\mathbf{x}}$, ($\mathbf{F} = d\vec{\mathbf{u}}/dt$). R, $\dot{T}_{Liq}$ and $\ddot{y}$ are the time rates of change of droplet radius r, temperature T_{Liq} and oscillation velocity $\dot{y}$. The source terms f_{coll} and f_{bu} account for changes in the distribution function due to droplet collision and breakup, respectively. The solution of the spray equation gives the so-called source terms that describe the interactions between the liquid and gas phases. This will be later used while coupling Lagrangian Droplet and Eulerian Flow (LDEF) solutions.

2.3.2 Coupling of Lagrangian Droplet Eulerian Flow Solutions

Although there has been a number of studies to use Eulerian droplet and Eulerian flow [40, 41] approach, LDEF is considered to be the most applicable approach in terms of computational costs and numerical accuracy in simulation of IC engines [42–44]. This needs proper coupling between the flow and spray solutions. In order to assure conservation of mass, momentum and energy of the total (two-phase) system, these terms are appeared as source terms in as in Eulerian gas flow equations of 2.2, 2.4, and 2.5, respectively.

The source term accounting for mass evaporation of the liquid droplets in Eq.2.2 can be determined from Lagrangian Spray solutions as below [45]:

$$\dot{\rho}^{Spray} = -\int f \rho_{Liq} 4\pi r^2 R \, d\overrightarrow{\mathbf{u}} \, dr \, dT_{Liq} \, dy \, d\dot{y} \tag{2.11}$$

The rate of momentum gain due to droplet drag and body forces in 2.4 can be determined from Lagrangian Spray solutions as below:

$$\rho_{Gas}\mathbf{F}^{Spray} = -\int f \rho_{Liq} \left(\frac{4}{3}\pi r^3 \mathbf{F}' + 4\pi r^2 R \overrightarrow{\mathbf{u}} \right) d\overrightarrow{\mathbf{u}} \, dr \, dT_{Liq} \, dy \, d\dot{y} \tag{2.12}$$

Source term for energy conservation of the gas phase, Eq.2.5, which is the energy transfer between gas and liquid droplets due to heat transfer and evaporation can be formulated as:

$$\begin{aligned} \dot{Q}^{Spray} = \int f \rho_{Liq} \Bigg(& 4\pi r^2 R \left[i_{Liq} + \frac{1}{2}(\overrightarrow{\mathbf{u}_{Liq}} - \overrightarrow{\mathbf{u}_{Gas}})^2 \right] + \\ & \frac{4}{3}\pi r^3 \left[c_{p,Liq} \dot{T}_L iq + \mathbf{F}'(\overrightarrow{\mathbf{u}_{Liq}} - \overrightarrow{\mathbf{u}_{Gas}} - \overrightarrow{\mathbf{u}_{Gas}}') \right] \Bigg) d\overrightarrow{\mathbf{u}_{Liq}} \, dr \, dT_{Liq} \, dy \, d\dot{y} \end{aligned} \tag{2.13}$$

and the destruction of turbulent kinetic energy due to liquid droplet dispersion is obtained by:

$$\dot{W}^{Spray} = -\int f \rho_{Liq} \frac{4}{3}\pi r^3 \mathbf{F}' \cdot \overrightarrow{\mathbf{u}_{Gas}}' \, d\overrightarrow{\mathbf{u}_{Liq}} \, dr \, dT_{Liq} \, dy \, d\dot{y} \tag{2.14}$$

In Eqs. 2.14 $\mathbf{F}'$ is the difference between $\mathbf{F}$ and the gravitational acceleration g, $\overrightarrow{\mathbf{u}_{Liq}}$ - $\overrightarrow{\mathbf{u}_{Gas}}$ is the relative velocity between droplets and gas phase, and $\overrightarrow{\mathbf{u}_{Gas}}'$ is the turbulent fluctuation of the gas velocity. In Eq. 2.13, i_{Liq} denotes the specific internal

energy of the liquid droplet. More details of the applied sub-models for the liquid spray modeling will be presented in §4.2.2.

2.3.3 Multi-component Fuels and Mixture Formation

Practical and commercial IC engine fuels are not single component and they include many aliphatic, aromatic, saturated, and unsaturated fuel components [46–49]. Based on phase equilibrium relations at the liquid droplet surface and assuming ideal behavior for both the vapor and liquid phases, Raoult's law can be applied in order to specify the concentration of each fuel component in the vapor phase. However, in case of multi-component fuels more volatile fuel component may not necessarily evaporate earlier due to non-equilibrium effects (*fugacity effects*) under IC engines operating conditions [50,51]. As an assumption then, numerical studies both for spray simulation and combustion chemistry consider a surrogate fuel specie. For instance, n-heptane was extensively used for Diesel engine combustion simulations [52–55] and recently n-dodecane with closer physical and chemical properties to the commercial Diesel fuels is used for experimental and numerical studies [35, 56–59]. Mixture formation in numerical point of view is simulated in the Eulerian part of the CFD solution and hence grid alignment can play a significant role on proper air-fuel mixing and fuel vapor penetration length. This will be discussed in §4.2 with extensive numerical results for non-reacting conditions. Moreover, processes before evaporation such as spray breakup and evaporation can be affected by uncertainties from injector internal flow and probable cavitaion. Brief numerical representation of the cavitation effect will be represented in §4.3.1.

2.4 Chemical Kinetics

Insightful understanding of the underlying chemical processes is an essential requirement on the study of reactive fluid flows. In many combustion applications assumption of the infinitely fast chemistry is not applicable and *chemical reactions* control the rate of combustion as well as pollutant emission formation/destruction. Moreover, ignition, flame lift-off, and flame extinction are intimately related to chemical processes. The study of elementary reactions and their rates, *Chemical Kinetics*, is inseparable field in combustion studies. If one mole of Fuel reacts with a mole of Oxidizer and produces b mole of Product in the form of reaction 2.15 below:

$$F \ + \ aOx \ \rightarrow \ bPr \tag{2.15}$$

the rate at which the fuel is consumed from experimental measurements can be expressed as:

$$\frac{d[X_F]}{dt} = -k_G(T)[X_F]^n[X_{Ox}]^m \tag{2.16}$$

where $[X_i]$ is molar concentration of the *i*th species in the mixture. Equation 2.16 represents that the rate of disappearance of the fuel is proportional to each of reactants raised to a power. k_G is the global rate coefficient which is a strong function of temperature. Exponents *n* and *m* are reaction order. Although combustion closure is considered to be in global reaction format in some CFD codes and studies [60–62], expressing chemistry in this form makes it a "black box" approach in a specific problem. For instance, use of global rate coefficient might not necessarily provide reliable reaction rates for a range of operating conditions in a IC engine simulation or possibility to track concentration change of a particular intermediate species such as CH_2O or OH while ignition of a liquid spray. Most elementary reactions in combustion are bimolecular similar to reaction below:

$$A \ + \ B \ \rightarrow \ C \ + \ D \tag{2.17}$$

and dissociation rate of chemical specie *A* can be written as:

$$\frac{d[A]}{dt} = -k_{bimolecular}[A][B] \tag{2.18}$$

There are different method to determine the rate coefficients [63–66] and molecular collision theory is one of them. It is based on probabilities that collision can lead to reaction based on product of two factors:the energy factor, $\exp[-E_A/R_uT]$, which is fraction of collision occurs with an energy above the required energy for reaction, E_A, or *activation energy*; and geometrical or *steric factor* which takes into account geometry of collision between reactants *A* and *B* [63]. If the temperature range of interest is not too high, the bimolecular rate coefficients can be expressed by the empirical *Arrhenius form*:

$$k(T) = A \ exp(-E_A/R_uT) \tag{2.19}$$

and if the temperature rate is great in the form of:

$$k(T) = A\,T^{b}\,exp(-E_A/R_uT) \tag{2.20}$$

where *A* is pre-exponential factor and *b* is temperature power. It is then possible to represent oxidation/dissociation pathways of one/more main chemical specie (fuel in case of combustion) by series of bimolecular reactions called chemical kinetics mechanism. Mechanism may involve many elementary steps and many species and in the compact notation can be expresses as below:

$$\sum_{j=1}^{N} \nu^{'}{}_{ji} X_j \;\Leftrightarrow\; \sum_{j=1}^{N} \nu^{''}{}_{ji} X_j \qquad for\ i = 1, 2, ..., L \tag{2.21}$$

$\nu^{'}_{ji}$ and $\nu^{''}_{ji}$ are the stoichiometric coefficients on the reactants and products side, respectively for the *j*th species in the *i*th reaction. Then *j*th species *production rate*, $\dot{\omega}_j$, can be calculated using equations below:

$$\dot{\omega}_j \;=\; \sum_{i=1}^{L} \nu_{ji} q_i \qquad for\ j = 1, 2, ..., N \tag{2.22}$$

$$\nu_{ji} = (\nu^{''}_{ji} - \nu^{'}_{ji}) \tag{2.23}$$

$$q_i = k_{fi} \prod_{j=1}^{N} [X_j]^{\nu^{'}_{ji}} - k_{bi} \prod_{j=1}^{N} [X_j]^{\nu^{''}_{ji}} \tag{2.24}$$

where subscripts f and b are for forward and backward reactions. Using the above formulation there will be a system of *L* ordinary differential equations with *N* unknowns. Due to exponential formulation and highly non-linear behavior of these equations (stiff equations) specific mathematical solution algorithms [67–69] must be applied to determine the reaction rates and species concentrations.

2.5 Turbulent Combustion

Combustion is almost always *modeled* in CFD codes and its participation in the conservation equations of the reacting flows is appearance of an open term in conservation of the chemical species mass fraction (Eq.2.3) and energy (Eq.2.5). This is because combustion takes place by breaking/formation of chemical bonds in molecular level and trade of electron between fuel, oxidizer, and numerous intermediate species and

generally CFD is not developed for such scales. This is why combustion appears as an open term due to not solving the chemistry in molecular scales. *Combustion Closure* can be considered as the most important task of combustion models which directly affect temperature rise and emission formation/destruction processes. As discussed before, addition of turbulent flow effects will generate wide range of physical time and length scales and in case of reactive flow these should also be considered together with chemical time scales [70]. Chemical processes cover time scales from nanoseconds to seconds and care must be taken in mathematical modeling in terms of chemical time scale to resolve the chemistry of reacting flows with a reliable description of the entire process. This is because phenomena such as ignition, extinction, and pollutant formation (NO_x, soot, Unburned Hydro Carbons, UHC) are kinetically controlled and oversimplified chemical schemes are not able to capture these processes efficiently. It has been observed [71, 72] that some chemical reactions are very fast that some chemical species in the reaction system are in a quasi steady state. Comparing the time scales of the chemical reactions with the typical physical time scales (turbulent mixing, molecular transport, residence times) in Fig.2.2, it can be observed that the chemical time scales span typically a much larger range. As only the time scales of similar order couple, it is needed to decouple the fast chemical time scales by assuming them to be in steady state and the slow ones by assuming that they are frozen [70].

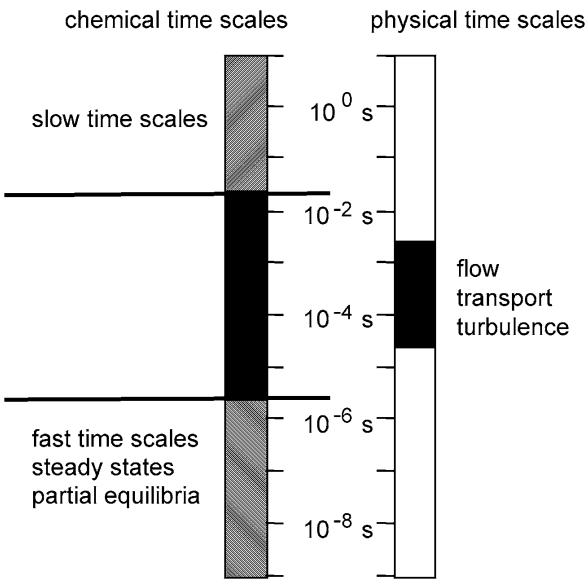

Figure 2.2: *Schematic representation of the time scales governing chemically reacting flows [70]*

2.6 Approaches to Turbulent Combustion Closure

Mixing of the fuel and oxidizer down to the molecular level is a perquisite of combustion. Here, turbulence can accelerate this mixing process and enhance the combustion and at the same time generated heat can strengthen flow instabilities and rapid development to the fully turbulent flow. Modeling of the turbulent combustion is mainly based on state of air-fuel mixing, turbulent length scales, and flame thickness which can result in different modes and regimes of turbulent combustion. Combustion closure is done by the main outcome of the combustion models, reaction rates, which will update the conservation equations. Now due to differences in the combustion modes and regimes, appropriate combustion closure must be applied for a typical reactive flow configuration to ensure reliable predictions. Based on state of air-fuel mixing, turbulent combustion can be classified into three main categories of: Premixed turbulent combustion, non-premixed turbulent combustion, and partially premixed turbulent combustion.

2.7 Premixed Turbulent Combustion

Flame is usually divided into a preheat zone, an inner layer, and an oxidation layer as shown in Fig.2.3 [25, 73]. Unburned gas is first preheated in the preheat zone where little heat is released. Inner layer contains the thickness in order of δ times thinner than the preheat zone where chemical reactions and fuel consumption mainly occurs in this layer. In case of turbulent conditions, turbulent eddies penetrate into the inner layer and mixing, heat conduction, and radical diffusion will be enhanced. Nevertheless, by further increasing the transport of heat and radicals above their production, flame can be extinguished.

An important length scale in laminar premixed flames is the characteristic flame thickness, l_F, defined by:

$$l_F = \frac{(\lambda/c_p)_o}{(\rho s_l^o)_u} \tag{2.25}$$

where λ is heat conductivity and c_p is the heat capacity at the inner layer temperature T^o, and ρ and s_l^o are the density and laminar burning velocity in the unburned gas.

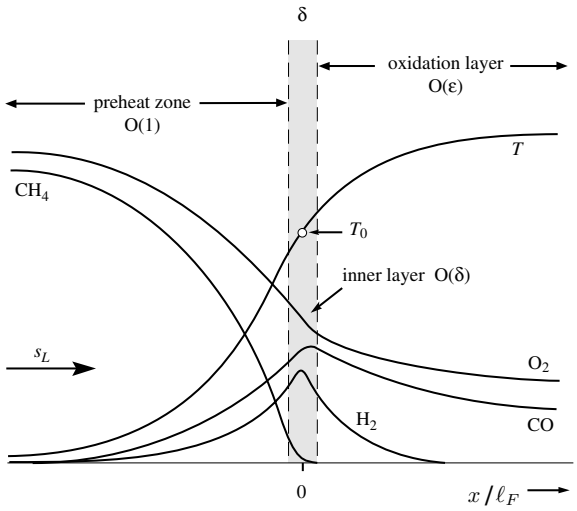

Figure 2.3: *Schematic illustration of the structure of a premixed methane-air flame [25]*

2.8 Regimes of Premixed Turbulent Combustion

By definition of number of non-dimensional numbers premixed turbulent combustion can be classified into four regimes [25]. Damköhler number, *Da*, is defined for the largest eddies and corresponds to the ratio of the integral time scale, τ_t, to the chemical time scales τ_c:

$$Da = \frac{\tau_t}{\tau_c} = \frac{l_t/u^{'}(l_t)}{\delta/s_l^o} \tag{2.26}$$

Karlovitz number, *Ka*, which measures the ratio of the flame thickness to the Kolmogorov scale:

$$Ka = \frac{l_F^2}{\eta^2} \tag{2.27}$$

and $Ka_\delta = \frac{l_\delta^2}{\eta^2}$ measures the ratio of the thickness of the inner layer to the Kolmogorov scale. Using these numbers premixed turbulent combustion regimes can be shown in the Fig.2.4 as proposed by Peters [25].

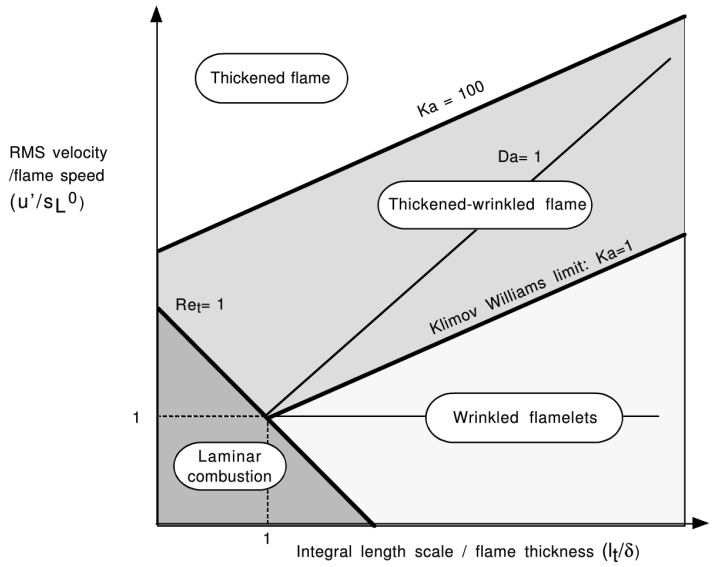

Figure 2.4: *Premixed turbulent combustion diagram proposed by Peters: combustion regimes are declared in terms of length* (l_t/δ) *and velocity* $(u^{'}/s_l^o)$ *ratios (log-log scale). [25]*

Identifying the regime(s) which the reacting flow is located is the basis of model development. Among combustion models of premixed turbulent combustion, G-Equation model [74–76] and flame surface density model [77–79] can be named. Combustion closure in premixed turbulent combustion utilizes laminar and turbulent flame speed as flame is propagating in premixed combustion mode. This is not discussed in the thesis as the focus is on non-premixed turbulent combustion of Diesel engines. Combustion models of Diesel engines will be represented in Chapter 3.

2.9 Non-premixed Turbulent Combustion

Due to safety issues and eliminating unwanted ignition and propagation speeds of premixed combustion, it is applicable to mix fuel and oxidizer while combustion. Non-premixed turbulent combustion is the main combustion mode which is applied in majority of industrial configurations such as furnaces, gas turbines, Diesel engines and etc. Non-premixed combustion is sometimes called diffusive combustion or combustion in diffusion flames since diffusion is the rate controlling process. The time needed for convection and diffusion, both being responsible for turbulent mixing, is typically much larger than the time needed for combustion reactions to occur. Comparing to the premixed combustion, modeling non-premixed turbulent combustion meets additional difficulties. Non-premixed flames do not propagate and located where the fuel

and oxidizer mixed properly and gas temperature is high enough to provide sustainable combustion. However, as there is no flame propagation, non-premixed turbulent flame is more sensitive to turbulence and is unable to impose its own dynamics to the flow field. Figure 2.5 below represents conceptual model for combustion of liquid spray at the sequence of fully established diffusive flame [80, 81].

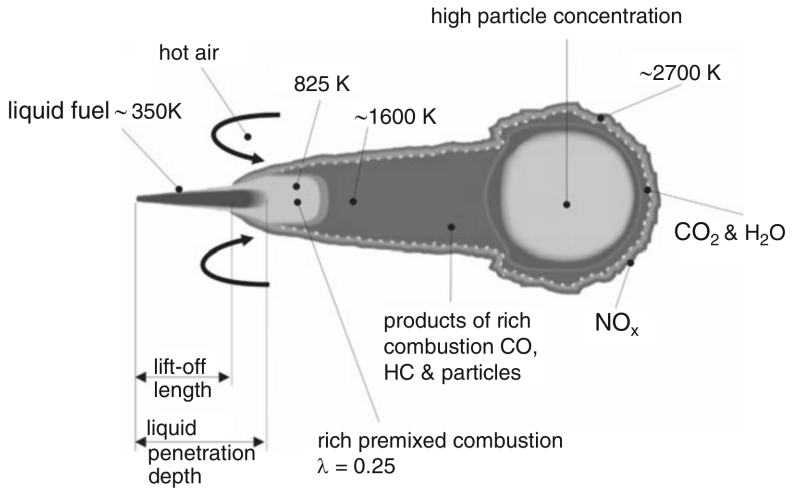

Figure 2.5: *Conceptual model for Diesel spray combustion under fully established diffusive flame phase. [25]*

2.10 Regimes of Non-premixed Turbulent Combustion

Compared to the premixed turbulent combustion, there is no intrinsic regime classification for non-premixed turbulent combustion. This is mainly due to the fact that there is no inherent length scales in non-premixed turbulent combustion and they strongly depend on flow conditions [14]. In non-premixed combustion, flame structure and the combustion regime depend on chemical characteristic time, τ_c. For fast chemistry (low τ_c values and large Damköhler numbers), the flame is very thin and can be considered to be a laminar flame element, *flamelet*. By further increasing chemical time, laminar assumption for the flame is no longer valid and unsteady effects are expected where for low Damköhler numbers, or large chemical times, extinction occurs. Simple representation of different regimes in non-premixed combustion can be considered by description based on two characteristic ratios:

- Damköhler number, $D_a = \tau_t/\tau_c$, as time ratio which corresponds to Damköhler number in premixed combustion.

- Length scale ratio l_t/l_d where l_t is integral length scale and l_d is diffusive thickness. As $l_d \approx \eta_k, l_t/l_d \approx Re_t^{3/4}$ where Re_t is turbulent Reynolds number.

Constant Damköhler number D_a^{fl} is for the line of slope 1/2 in log-log (D_a,Re_t) diagram. If the chemistry is fast, the flame is expected to be laminar flame (LF) and extinction occurs for large chemical times when $D_a^{fl} \leq D_a^{ext}$ as shown in figure below:

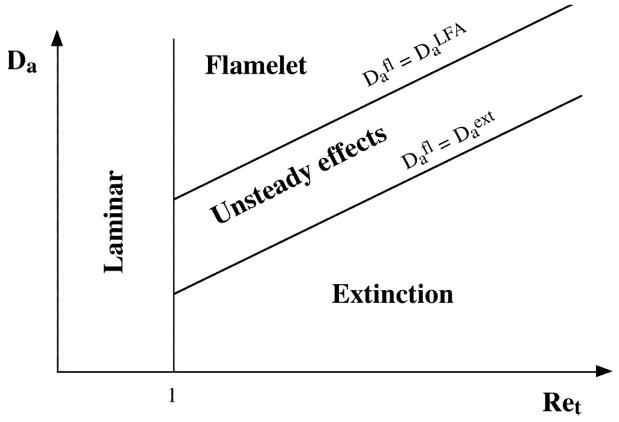

Figure 2.6: *Regimes of non-premixed turbulent combustion [25]*

In practical non-premixed combustion configurations, the time needed for convection and diffusion which are responsible for turbulent mixing, is typically much larger than the time needed for chemical reactions to occur. The assumption of infinitely fast chemistry or local chemical equilibrium therefore appears to be appropriate. It is an assumption that introduces an important simplification, since it eliminates all parameters associated with finite-rate chemical kinetics from the analysis. Nevertheless, unsteady flamelets and extinction can occur in specific conditions. Burke and Schumann [82] used the fast chemistry assumption to predict global properties such as the flame length of a jet diffusion flame. Essential feature for their formulation of diffusive combustion is the introduction of a chemistry-independent variable, *conserved scalar*, called the *Mixture Fraction*, *Z*. Derivation of mixture fraction is not repeated here and reader can refer to a review of the conserved scalar approach by Bilger [83]. All scalars such as temperature, chemical species concentrations, and density are then uniquely related to the mixture fraction by transformation of coordinates from physical space (**x**, t) to mixture fraction space (*Z*, y_2, y_3,t) as schematically illustrated in Fig.2.7.

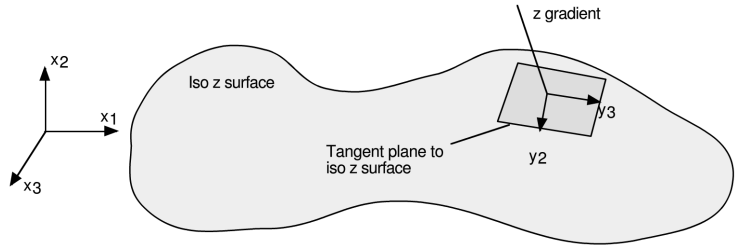

Figure 2.7: *Transformation of coordinates from physical space to mixture fraction space [25]*

where y_2 and y_3 are spatial variables in planes to iso-Z surfaces. These terms, gradients along the flame front, compared to the terms normal to the flame, gradients along Z [21, 25].

Figure below illustrates the diffusive flame structure for Burke and Schumann solution of irreversible infinitely fast chemistry for temperature, fuel, and oxidizer mass fractions.

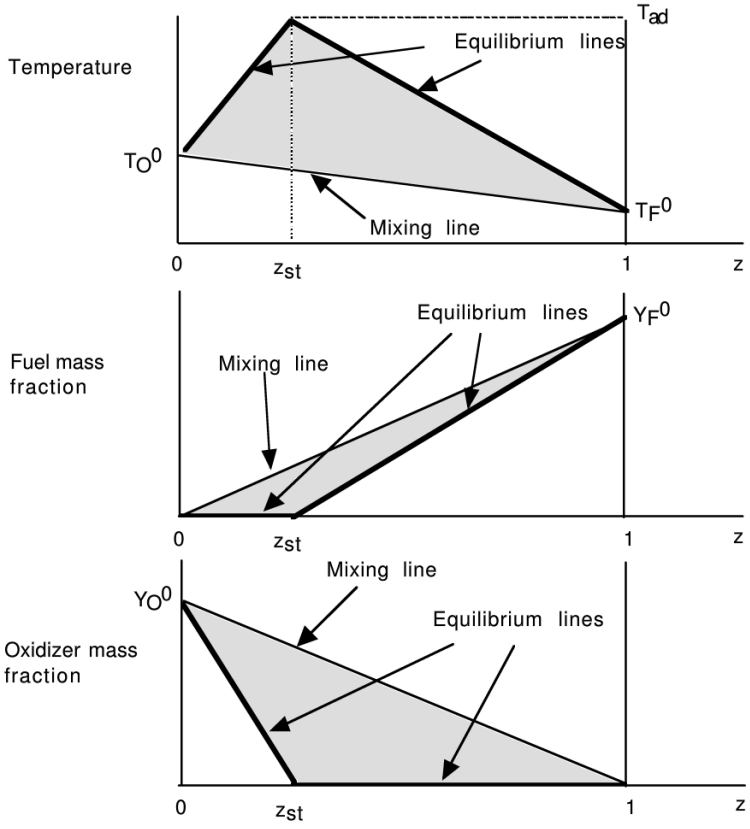

Figure 2.8: *Diffusive flame structure for Burke and Schumann solution of irreversible infinitely fast chemistry (equilibrium lines) in conjunction with pure mixing (mixing line) without chemical reactions [82] gray areas in the diagrams represent possible thermodynamic states [25].*

However, in turbulent flows it is possible that local diffusion time scales are not so large compared to the time scales of chemical reactions. The fast chemistry assumption is then not valid and non-equilibrium effects must be taken into account. Further reduction of diffusion time scales leads to lift-off and eventually blow-off of the entire turbulent flame. For finite rate chemistry, the chemical time, τ_c, is comparable to flow time scale, τ_f and D_a^{fl} takes finite values. Practically, chemistry effect are only important where reaction occurs and outside of this region combustion is zero and all the concepts developed for infinitely fast chemistry apply. Hence, Z diagrams of temperature, fuel and oxidizer mass fractions are only affected in the vicinity of the flame front which is mixture fraction values close to the stoichiometric mixture fraction, Z_{St}. Figure 2.8 can now be modified to consider finite rate chemistry effects:

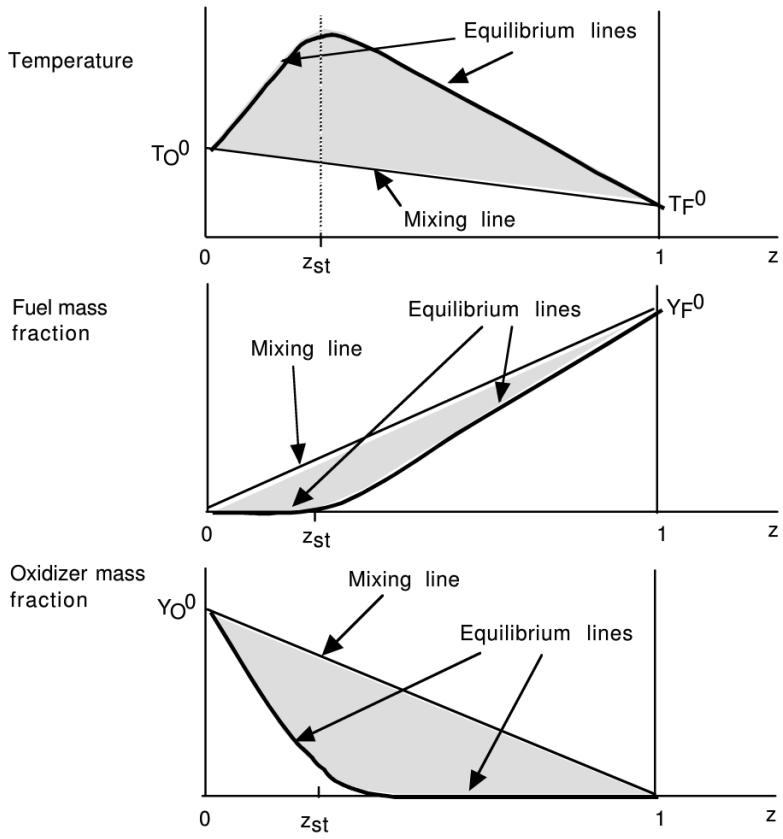

Figure 2.9: *Diffusive flame structure for finite rate chemistry for temperature and fuel and oxidizer mass fractions [25]*

Mathematical framework for application of these concepts in terms of combustion models for non-premixed and partially premixed turbulent combustion will be discussed in §3.2.2.

2.11 Partially Premixed Turbulent Combustion

As is has been discussed, state of air-fuel mixing can experience two extreme conditions of premixed and non-premixed mixtures. In practical configurations, however, this often lies somewhere between the extremes. If fuel and oxidizer enter separately, but partially mix by turbulence, combustion takes place in a stratified medium, once the mixture is ignited. Such a mode of combustion has traditionally been called partially premixed combustion which can be seen in gas turbines, Gasoline Direct Injection (GDI) engines, and Diesel engines. In CI Diesel engines, non-premixed turbulent combustion is affected and controlled by ignition sequence and then premixed combustion phase. During the ignition delay time, stratified charge of air-fuel mixture is formed and then burnout of the partially premixed part of the charge occurs essentially by flame propagation normal to the iso-mixture fraction surfaces. This will be discussed in the next section of combustion phasing in high pressure reacting sprays. More in Diesel spray combustion, flame lift-off and stabilization mimic characteristics of partially premixed turbulent combustion. Domingo and Vervisch [84] suggest that triple flame propagation through a stratified mixture is an important mechanism in the early phase of combustion in a Diesel engine. This phase is often referred to as the premixed combustion phase. Triple flames are a key element of partially premixed combustion. If a range of the mixture fractions $Z_{min} < Z < Z_{max}$ exists in a partially premixed field, and the stoichiometric mixture fraction lies between these limits, flame propagation generates a flame structure called a triple flame. Schematic of triple flame in partially premixed combustion is shown in Fig. 2.10 below:

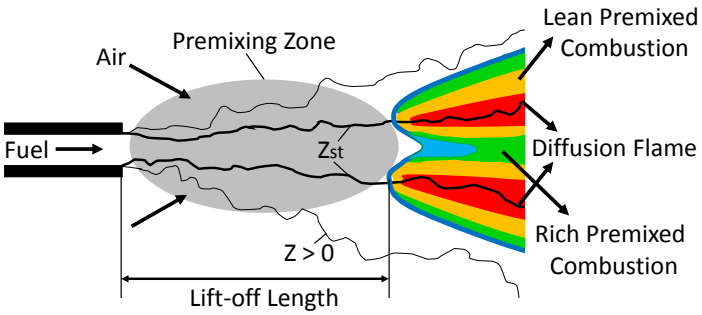

Figure 2.10: *Schematic representation of a lifted triple flame in partially premixed combustion*

Whether triple flames are effective in stabilization mechanisms of a non-premixed combustion is a controversial issue. Nevertheless, DNS simulations of Domingo and

Vervisch [84] show that triple flame like structures are found in the stabilization regions of turbulent lifted flames. In case of Diesel high pressure spray flames, stabilization maybe insured by the ignition process within the premixing zone in the Fig. 2.10. Extensive discussions on propagating characteristics of lean/rich premixed flames in partially premixed combustion can be found in [25].

2.12 Combustion Phasing in High Pressure Reacting Sprays

In case of reacting sprays such as Diesel engines, air-fuel mixing and combustion interactively govern the ignition and combustion. Presence of dense liquid prays in Diesel engines adds in number of physical processes: primary/secondary breakup, atomization, evaporation, and mixing before/while heat release history. Heat Release Rate (HRR) diagrams provide useful information for combustion phasing of reacting sprays. For instance, a typical HRR diagram for a Diesel engine is illustrated in Fig.2.11 versus engine Crank Angle Degree (CAD) and it can be considered to undergo three combustion phases after the ignition sequence. Ignition and combustion phases of high pressure reacting sprays will be discussed in the following sub-sections:

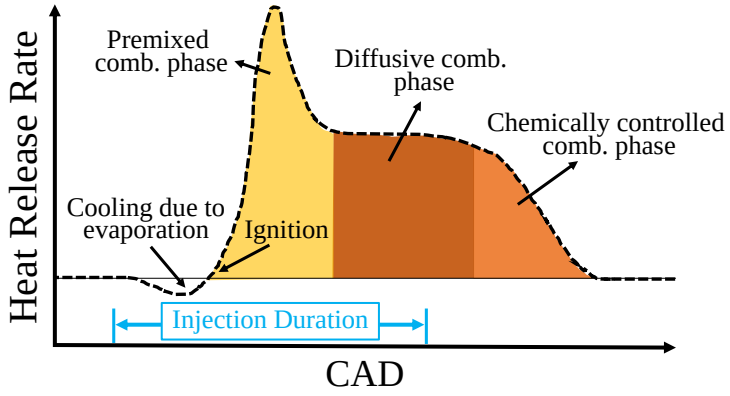

Figure 2.11: *Typical HRR diagram for Diesel engine combustion with ignition time and premixed combustion, diffusive combustion, and chemically controlled combustion phases.*

2.12.1 Ignition

After initiation of the injection process, liquid fuel droplets undergo a number of physical processes: breakup, atomization, vaporization, and mixing with oxidizer and create layers of mixture fraction with different magnitudes. It should be noted soon after initiation of the injection process, all mentioned processes take apart almost simultaneously together with ignition and combustion. Liquid fuel droplets have different momentum

where earlier injected droplets downstream of the injection axis possess small velocities and their motion can be affected by gas flow, whereas newly injected droplets contain higher velocities and their motion is almost unaffected by turbulent gas flow. This behavior can be characterized by Stokes Number [85]:

$$St = t_v/t_l \tag{2.28}$$

where t_v is droplet vaporization time scale and t_l is integral time scale in mixing layer of large turbulent vortices $t_l = l/\mathbf{u}$. As depicted in Fig. 2.12, droplet motion with a high Stokes number is not affected by turbulent vortexes and in near unity Stokes number droplet motion is getting to be under control of turbulent vortexes and in a low Stokes number droplet motion is governed by turbulent vortexes.

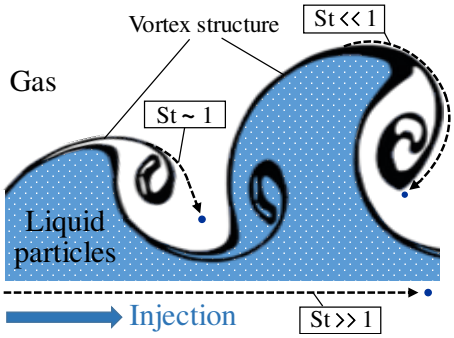

Figure 2.12: *Schematic motion of liquid droplets (dashed curves) based on their Stokes number in turbulent gas flow.*

For ignition of a liquid droplet based on its Stokes number three different outcomes are possible. For $St \gg 1$, the droplets on the spray side of the mixing layer are insensitive to the velocity perturbations induced by the large vortical motion and therefore continue in straight trajectories. In this condition, the droplets remain surrounded by the cold gas, thereby hindering droplet vaporization, Fig.2.13 (b). An increasing interaction of the droplets with the turbulent eddies occurs as the Stokes number decreases, with droplet dispersion becoming optimal for $St \approx 1$ the droplets are ejected from the spray side through the high strain regions, resulting in non-uniform droplet distributions (Fig.2.13(c)) [85]. This droplets cross the mixing layer and vaporize on the other side surrounded by hot air and form reactive pockets.

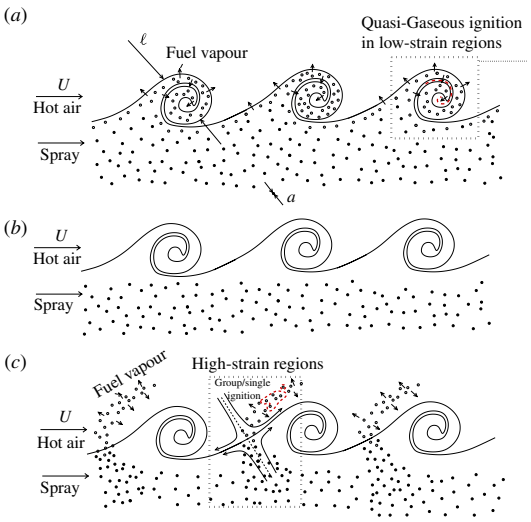

Figure 2.13: *Schematic of mixing layers in reactive liquid sprays based on small (a), large (b) and near unity (c) Stokes numbers taken from [85]*

For $St<1$, the droplets behave as flow tracers and become entrained in the large scale turbulent eddies, where they come into contact with the hot gas, thereby promoting vaporization and ignition of the fuel spray in the resulting mixing layers (Fig.2.13(a)). Ignition then occurs in regions with low scalar dissipation rate with *Most Reactive Mixture Fraction* which will be defined later. As injection goes on, premixed or partially premixed air-fuel mixtures are exposed to the hot combustion chamber gas and condition for ignition or sometimes called auto-ignition will be provided. Ignition and extinction are important limit phenomena in combustion theory and their states were conventionally defined as the turning points on the *S-curve* diagram as shown in Fig. 2.14.

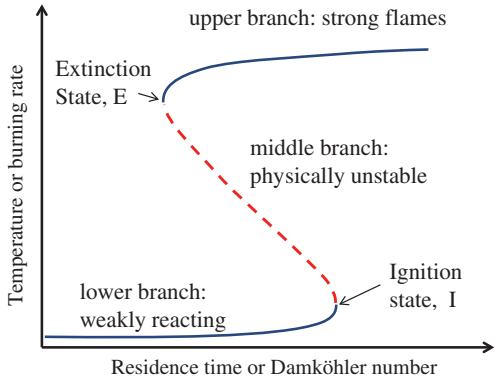

Figure 2.14: *Folded S-curve diagram for ignition and extinction states [86].*

The upper and the lower branches of this diagram are known to be stable where the upper branch indicates strongly burning flames and the lower branch indicates weak reactions, and the middle branch is known to be unstable states which experimentally cannot be obtained. The upper turning point is considered as the extinction state of strong flames as a strong flame cannot be sustained with further reduced Damköhler number or residence time. Similarly, the lower turning point is known as the ignition state since the steady state solution will jump to the upper branch with further increased Damköhler number or residence time. Shan and Lu [86] showed that for hydrocarbons with two stage ignition this curve is in the shape of two attached *S* curves with additional ignition and extinction states as shown in Fig.2.15.

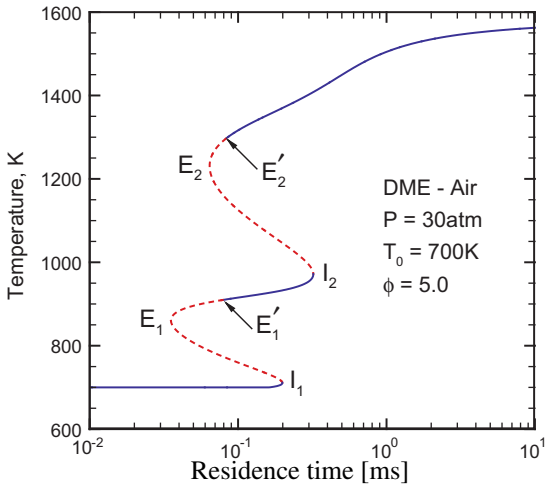

Figure 2.15: *Temperature as a function of residence time (ms) for perfectly stirred reactor simulations of dimethyl ether-air mixture at pressure of 30atm, initial temperature of 700K [86].*

Compared to available literature on occurrence of ignition in gaseous fuel problems, there is virtually no information on this topic available for sprays. In a turbulent spray, the fuel evaporation introduces an additional timescale to the problem and the droplet size and spacing introduce additional length scales [87]. Mastorakos et al. [88] show that ignition for non-premixed combustion (mixing layer configuration) is initiated from a mixture fraction called: *Most Reactive Mixture Fraction*, Z_{MR}, which is different from stoichiometric mixture fraction. They also concluded that ignition occurs in Z_{MR} and where the conditional scalar dissipation rate (will be discussed in §3.2.2) $\chi|_{Z_{MR}}$ is low. In reacting sprays close to the injector orifice, regions with high

χ, large heat losses occur and ignition for Z_{MR} cannot take place, while further regions with low χ will have low heat losses during the ignition delay times. It should be noted that in the literature different definitions of ignition sequence and the criteria to its representation are used [87]. Maximum pressure rise, temperature rise or noticeable production/consumption of specific chemical species or reaching to a percentage of accumulated heat release are some of criteria to define ignition time. In case of mixture fraction versus temperature (Z-T) diagram, Mastorakos [87] stated that for hydrogen non-premixed combustion, increased temperature above the mixing line in conjunction with noticeable production of HO_2 can show the time of ignition (Fig.2.16). However, still threshold for ignition remained a vague point and no quantification for either temporal temperature above the initial temperature value or mass fraction of HO_2 above the certain value is considered in their study. In prior two dimensional DNS study of Mastorakos et al. [88] on non-premixed combustion of methane with one-step chemistry, Fig. 2.17, it is represented that ignition starts at low scalar dissipation rates from most reactive mixture fraction, $Z_{MR} \approx 0.13$, and later shifts towards the stoichiometric mixture fraction, Z_{St}=0.055, during the diffusive combustion. It is also concluded that for laminar igniting mixing layers, most reactive mixture fraction, Z_{MR}, only depends on: the *initial fuel and oxidant temperatures* and the *activation energy*.

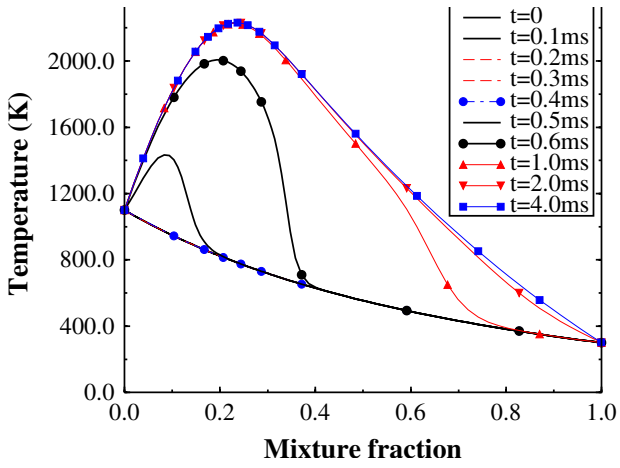

Figure 2.16: *Mixture fraction versus temperature diagram of hydrogen-air constant-strain mixing layer with χ =20 1/s in time (ms), Z_{St}=0.127 [87]. Time of t=0.1ms was considered as the time of ignition.*

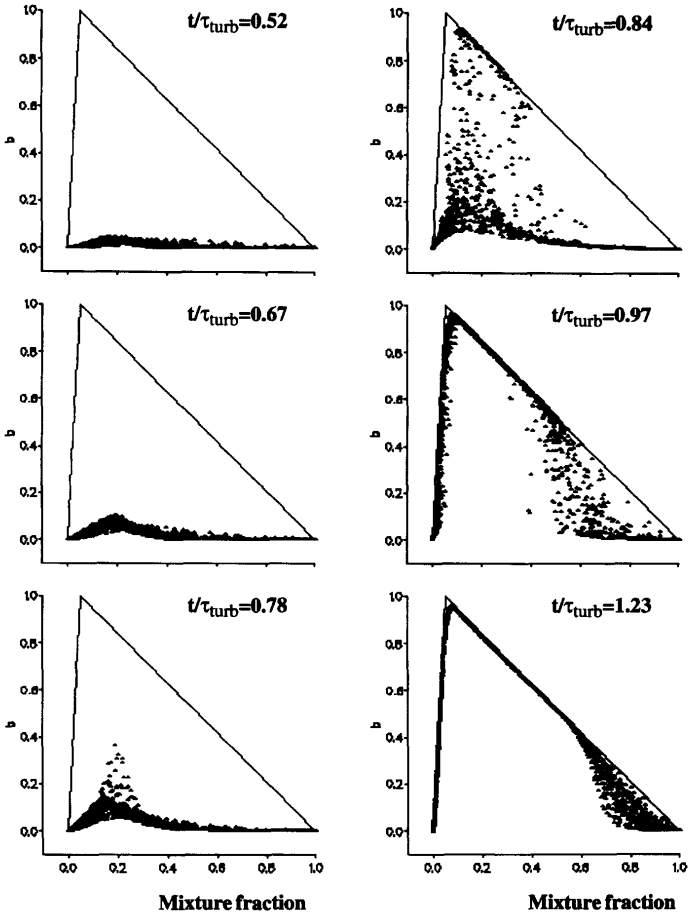

Figure 2.17: *Normalized temperature, b, above the initial inert value versus mixture fraction from two dimensional DNS simulation of methane non-premixed combustion with one-step chemistry for various times. The turbulence timescale, τ_{turb}, in the original reference is such that ignition occurs at about t/τ_{turb} = 0.78 [88].*

Based on this finding, ignition occurs at mixture fractions close to Z_{MR} and then reaction zone propagates in two directions of lean and rich mixtures fractions. Diffusive flame will form when the reaction zone ignites the stoichiometric mixture fraction. Two rich and lean premixed flames at sides of diffusive flame burn with lower reactivity and as they depart from diffusive flame get weaker and may extinct due to high scalar dissipation rates and heat rejection or reaching to flammability limits [25].

In order to quantify the value of Z_{MR}, three methods can be applied [87]. First, homogeneous reactor calculations can be conducted, with initial conditions of species and temperature corresponding to frozen mixing between the cold fuel and the hot air. Based on a criteria for the definition of the ignition, a curve for ignition time versus

applied mixture fractions results in a minimum value. Mixture fraction for the minimum ignition time is Z_{MR}. Second, asymptotic analysis results from Ref. [89] can be used for constant-strain problems. Lastly, conducting laminar mixing layer simulations and examine the location where the reaction rate peaks or ignition occurs. This can provide useful insights later for initiation of the premixed combustion phase which will be triggered by ignition.

2.12.2 Premixed Combustion Phase

Premixed combustion phase follows immediately after ignition as shown in Fig.2.11. Injected fuel during the ignition delay time mixes with air in the combustion chamber and forms a nearly homogeneous and reactive mixture. After ignition, prepared air-fuel mixture burns very quickly. Since areas with premixed combustion arise in the main combustion phase as well, this phase is called premixed combustion [90]. The rate of heat release in this combustion phase is determined by the speed of the chemical reactions and by the amount of air-fuel mixture formed during the ignition delay. Advancing injection timing will provide larger amount of air-fuel mixture and once it is ignited, premixed phase will result in a higher heat release rate. Engine boost pressure and temperature have direct effect on strength of heat release rate in this phase.

When the Z_{MR} is ignited, reaction zone spreads in the stratified premixed mixture (richer at the core) and as discussed in §2.12.1 reactions proceed both in lean and rich mixture fractions till all premixed mixture is burned or reaction zone reaches locally high scalar dissipation rates and possible flame extinction occurs. Hence, generally premixed combustion phase of turbulent reacting sprays is the time taking for the reaction zone after igniting in Z_{MR} and burning premixed flammable mixture fractions (including stoichiometric mixture fraction) and then locate again on the stoichiometric mixture fraction. This is also believed that this phase has a noticeable effect on diffusive flame stabilization later on diffusive combustion phase [90].

2.12.3 Diffusive Combustion Phase

In this phase, heat release rate is nearly constant (as represented in Fig.2.11) and controlled by the turbulent mixing processes between the fuel and air and therefore also is called mixing-controlled combustion [90]. In this phase, injection, spray breakup, evaporation, mixing with oxidizer, combustion, and pollutant formation all take place

simultaneously. A diffusive flame is formed around the spray on an iso-surface with a stoichiometric mixture fraction. Partially oxidized products of the rich premixed combustion such as CO and the particles move further downstream and are transported into the diffusive flame, where they are completely oxidized into CO_2 and H_2O. Reaction zone burns with adiabatic flame temperature at the range up to 2700K for commonly used hydrocarbon fuels. Due to the high temperatures, NO_x is formed on the lean side of the diffusive flame. Near the injector nozzle due to high velocities, insufficient mixing, and high scalar dissipation rates, flame cannot be formed but further downstream these effects are mitigated and self sustaining reactions can take place and diffusive flame establishes itself. The axial distance between the nozzle orifice and the diffusion flame is called the lift-off length and is an important property of a Diesel flame with regard to soot formation [91]. This phase continues a little bit more than end of injection (see Fig.2.11) as last liquid fuel droplets undergo the breakup and vaporization processes.

2.12.4 Chemically Controlled Combustion Phase

A little time after end of injection no additional momentum is added to the spray by the injection. In this phase, flame structure evolves into a pocket of rich premixed products surrounded by a diffusion flame. The exact properties of this zone depend on the injection system. If the nozzle needle closes very quickly, then the last fuel parcels still have high speed, so that they follow very similar combustion sequence as in diffusive combustion phase. On the other hand, a slow closure of the needle leads to low speeds of the last fuel particles with low mixing with oxidizer and consequently increased formation of soot emission. As this phase mainly occurrs while the engine is in the expansion stroke, combustion chamber temperature is lowered and the reaction rates go down with longer chemical time scales so that combustion is chemically controlled again. This phase is of extreme importance for final emission levels such as the oxidation of the previously formed CO and soot, of which over 90% is decomposed again [91].

CHAPTER 3

Turbulent Non-premixed and Partially Premixed Combustion Modeling: Theory and Formulation

In this chapter modeling approaches and their formulation for combustion closure of turbulent non-premixed and partially premixed combustion will be discussed. Detailed understanding of the assumptions, capabilities, and limitations of the applied models is necessary to obtain reliable and valid results from reacting spray simulations. It should be noted that focus has been given to combustion within CI Diesel, HCCI, and PPCI engines and not to propagating flames as of SI engines. State of the art on modeling reacting sprays and combustion configurations under non-premixed and partially premixed combustion regimes will be discussed next. Moreover, extensive explanations of the applied combustion models for the results section of the thesis (Chapter 5, 6, and 7) will be provided.

3.1 State of the Art on Simulation of Reacting Sprays

The way to tackle the problem of non/partially premixed turbulent combustion of reacting sprays can be categorized in a number of perspectives as they include wide range of time and length scales. It has been discussed before that applying spray of heavy hydrocarbons under reacting conditions will introduce wide range of chemical (due to large number of chain branching reactions and elementary chemical species) and turbulent (due to high momentum of spray and its interactions with fluid flow) and additionally liquid droplet evaporation time and length scales.

Turbulence-Chemistry Interactions (TCI) is an important concept in combustion modeling of a reactive spray and can divide combustion models which include TCI and the ones they do not. For instance, there is no TCI considerations in Well-Mixed (WM) combustion models and in these models it is assumed that fuel, oxidizer, and possibly products are fully homogeneous in each CFD cell. Although each CFD cell can exchange momentum, chemical species, and heat with the neighbor cells, calculation of the combustion source terms (based on global reactions or chemical kinetics) for the update of the conservation equations is performed for the full homogeneous composition of a typical cell. Despite the fact that models without considering TCI, possess less physics for turbulent mixing, they have extensively used in Diesel combustion simulations [35, 92–97]. On the other hand, a number of models developed with considering TCI effects. Transported Probability Density Functions (TPDF) [98–103] and Representative Interactive Flamelet (RIF) [35, 104–107] models were formulated to include TCI effects. Both methods were applied in simulations of reactive sprays and enhanced numerical results for Ignition Delay (ID) and Length of flame Lift-off (LOL) were reported comparing to the models without TCI.

Other classification of the combustion models can be based on how the chemistry is treated while solving for CFD. So-called *on-the-fly chemistry* models, are the models which combustion source terms (either with TCI or without TCI considerations) are calculated (by solving system of stiff ordinary differential equations) in a typical CFD time-step and update the conservation equations at the end of time-step. Tabulated chemistry is an alternative way to include chemical kinetics mechanism with noticeably lower computational costs. The main difference here is that combustion source terms in the conservation equations were not calculated while solving for CFD and instead, state of thermodynamics of the reacting mixture in a time-step is read and updated from

previously generated tables by definition of a transported parameter so-called *progress variable* [108–114]. In this context, progress variable is the link between fluid flow calculation and tabulated chemistry (flamelet look-up tables) and needs comprehensive definition, transport, retrieval, and utilization. Failure in all mentioned concepts of progress variable, will result in wrong determination of thermodynamic state of reactive fluid flow and results with unphysical meanings. There is a need to store needed data of chemistry in the flamelet tables which will be later read by CFD solver to update the thermodynamic state by the link of progress variable [115]. Definition and utilization of the progress variable is not unique and straightforward, however, as Ihme et al. [116] stated, the choice of a suitable progress variable should be guided by the following principles: *a)* Being able to be transported within the CFD domain. *b)* The reactive scalars used for its definition, should all evolve on comparable time scales. *c)* Generation of flamelet tables should be based on independent parameters. and *d)* Mentioned independent parameters should uniquely characterize one point in the thermo-chemical state-space. There have been different methodologies on generation of flamelet tables such as: Flamelet Prolongation of ILDM (FPI) [117], Flamelet generated Manifold (FGM) [112], and Perfectly Stirred Reactor (PSR) [118] and the aim of all these methods is to determine source of progress variable which will be later used to update its transport equation. There has been also a number of different methods for progress variable definition which can be enthalpy or chemical specie based.

Models for combustion of a typical reactive flow configuration can be selected and used based on their applicability, reliability, and range of accuracy. Models such as TPDF although provide more accurate results due to detailed considerations of the physical phenomena, are tangibly more time-consuming and demand high computational times. On the other hand, detailed observation of transient phenomena such as ignition, re-ignition and quenching require comprehensive models and detailed insights cannot be achieved by simplified models.

3.2 Applied Non-premixed and Partially Premixed Turbulent Combustion Models

In this section extensive explanations of the applied combustion models will be discussed. Results of these models will be presented for the combustion of reactive sprays, Diesel, HCCI, and PPCI engines in Chapters 5, 6, and 7.

3.2.1 Multi-Zone Well-Mixed Chemistry Model

MZWM model is based on Well-Mixed combustion model which treats each CFD cell as a closed homogeneous reactor and computes the chemical species reaction rates accordingly. Temperature, pressure and the chemical composition of the each cell are passed to a stiff ODE solver to integrate and calculate $\dot{\omega}_j$ (Eq. 2.21) during the given time-step to update combustion source terms in species mass and energy conservation equations. Although TCI is not considered in the MZWM model, when applied to Diesel combustion it provides a reasonable estimation of ignition time and burning rate during the premixed combustion phase, as shown in [119–121]. This model is flexible with respect to the applied combustion mode but the main drawback of the WM model is represented by the need to employ an operator splitting technique for the computation of the chemical reaction rates. It requires integrating the species equations using a stiff ODE solver. This aspect represents a large computational overhead and makes this model unsuitable for multi-cycle engine calculations. Different solutions proposed over the years to reduce the computational time including on-the-fly tabulation and mechanism reduction techniques such as *in-situ adaptive tabulation*, *dynamic adaptive chemistry* and *multi-zone chemistry* [122–125]. Multi-Zoning approach will be discussed next.

Zoning Strategy

Computational efficiency is achieved by utilizing the multi-zone chemistry approach originally presented in [126]. According to user-specified tolerances, zones are created by clustering CFD cells with similar temperature and progress equivalence ratio. The number of zones dynamically varies during the simulation, to properly account for temperature and mixture distribution inside the combustion chamber. Chemistry is then integrated only once per zone and reaction rates are mapped back to the CFD domain by employing a technique which preserves local cell composition and chemical elements. Zones are divided based on temperature and the progress equivalence ratio of the cells. The progress equivalence ratio ϕ_p is chosen to account for both composition and combustion progress effects. ϕ_p is defined as:

$$\phi_p = \frac{2C^{\#}_{-CO_2} + \frac{H^{\#}_{-H_2O}}{2}}{O^{\#}_{-CO_2-H_2O}} \tag{3.1}$$

where first term in the numerator is the number of carbon atoms without CO_2, sec-

ond term is number of hydrogen atoms without H_2O and denominator is number of oxygen atoms without CO_2 and H_2O. Resolutions of 5K and 0.05 are considered to divide zones and cluster the CFD grids for temperature and ϕ_p, respectively.

Mapping Strategy

Chemistry is solved in each zone and, accordingly, reaction rates are computed for each one of them. Mapping back reaction rates to any computational cell is not straightforward and must be conservative with respect to the chemical elements. The mapping strategy proposed by Babajimopoulos [127] was used. It is based on the *"ch"* value of the individual cells in the zone which is defined as:

$$ch_{cell} = 2C^{\#}_{-CO_2} + \frac{H^{\#}_{-H_2O}}{2} \tag{3.2}$$

The *"ch"* value is calculated for all of the individual cells and the zones before the start of chemistry calculations on the zones. The sum of all the *"ch"* values of the individual cells (*"*ch_{cell}*"*) in a particular zone will be equal to the *"ch"* value of the zone (*"*ch_{zone}*"*):

$$\dot{\omega}_{j,cell} = \frac{ch_{cell}}{ch_{zone}} \dot{\omega}_{j,zone} \tag{3.3}$$

Operation of the multi-zone chemistry is summarized in Fig. 3.1

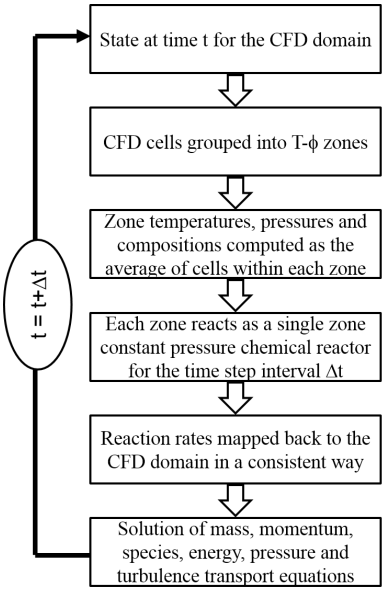

Figure 3.1: *Flowchart of the MZWM model [126].*

3.2.2 Multiple Representative Interactive Flamelet Model

Laminar Flamelet Approach

The *flamelet* approach is based on two principles. One is the use of the conserved scalar, mixture fraction *Z*, and the other is the transform of coordinates from *physical space* and consider the turbulent combustion characteristics in *reaction space*. In the flow field, conserved scalar, *Z*, is used to account for the turbulent mixing between the vaporized fuel and the oxidizer streams. Meanwhile, reaction, diffusion, and mass fraction change of chemical species are determined in the reaction space for different values of *Z*. This was also discussed in §2.10. Derivation of the governing equations in the physical space and the reaction space will be discussed following the approach of Peters [25].

Physical Space: Conserved Scalar Variable

In non-premixed turbulent combustion system, the fuel and the oxidizer are separately introduced into the combustion chamber where they are mixed. The level of mixing between the fuel and the oxidizer can be described by introducing a conserved scalar variable as discussed in Chapter 2. The conserved scalar variable (for instance mixture fraction in this thesis), as its name implies, does not vary due to chemical reaction. This characteristic enables to use a conserved scalar to track mixing between fuel and oxidizer regardless of reaction. Hence, local chemical composition can be estimated from the Z field in the physical space, assuming that its sub-grid distribution can be represented by a β-PDF. To this end, transport equations for both Z and its variance need to be solved, accounting for spray evaporation effects [128]. In this work, the approach proposed by Hasse was followed [129]:

$$\frac{D\left(\rho\tilde{Z}\right)}{Dt} = \nabla\cdot\left(\frac{\mu_t}{Sc_{\tilde{Z}}}\nabla\tilde{Z}\right) + \dot{S} \tag{3.4}$$

$$\frac{D\left(\rho\widetilde{Z''^2}\right)}{Dt} = \nabla\cdot\left(\frac{\mu_t}{Sc_{\widetilde{Z''^2}}}\nabla\widetilde{Z''^2}\right) + 2\frac{\mu_t}{Sc_{\widetilde{Z''^2}}}\left|\nabla Z\right|^2 - \rho\chi \tag{3.5}$$

where $Sc_{\tilde{Z}}$ and $Sc_{\widetilde{Z''^2}}$ are constants and set to 0.9 as suggested in [130]. $\dot{S}$ is the liquid mass evaporation rate per unit volume. Generation of mixture fraction variance is due to strain rate while the sink term appearing in Eq. 3.5 is the average scalar dissipation

rate, which is function of the turbulent time scale and mixture fraction variance:

$$\chi = C_\chi \frac{\varepsilon}{k} \widetilde{Z''^2} \tag{3.6}$$

where the constant C_χ was set to 2 in the thesis. Scalar dissipation rate is a key element in non-premixed turbulent combustion and has the significance of an effective diffusion in the mixture fraction space and is responsible for so-called flame stretching effects, i.e. laminar flow equilibrium between diffusion and reaction. It has the dimension of an inverse time and therefore represents the inverse of a diffusion time scale. In principle, both the mixture fraction, Z, and the scalar dissipation rate, χ, are fluctuating quantities and their statistical distribution needs to be considered, if one wants to calculate statistical moments of the reactive scalars [25].

Reaction Space: Flamelet Equations

Reaction space in MRIF model is based on the laminar flamelet concept, assuming that the smallest turbulent time and length scales are much larger than the chemical ones and there exists a locally undisturbed sheet where reactions occur [131]. This sheet can be treated as an ensemble of stretched counter-flow diffusion flames, called *flamelets*. The advantage of such treatment is that all reacting scalars only depend on the mixture fraction variable, Z, which is related to the local fuel-to-air ratio for non-premixed combustion. In order to properly account for local flow and turbulence effects on the flame structure and predict flame stabilization, a multiple number of flamelets can be used. Each one is representative of a certain portion of the injected fuel mass, and chemical composition in each cell is computed from mixture fraction and flamelet marker distribution as follows:

$$Y_i\left(\vec{x}\right) = \sum_{j=1}^{N_f} M_j \int_0^1 Y_{j,i}\left(Z\right) P\left(Z, \widetilde{Z''^2}\right) dZ \tag{3.7}$$

For each flamelet marker, M_j, the following transport equation is solved:

$$\frac{D\left(\rho \tilde{M}_j\right)}{Dt} + \nabla \cdot \left(\frac{\mu_t}{\tilde{Sc}_Z} \nabla \tilde{M}_j\right) = \dot{S}_{M_j} \tag{3.8}$$

where the source term $\dot{S}_{M_j}$ corresponds to $\dot{S}$ only for a specified interval of the injection duration, while it is zero elsewhere. Flamelet markers must also satisfy the following relation:

$$Z = \sum_{j=1}^{N_f} M_j \tag{3.9}$$

Where N_f is the number of considered flamelets. The local flame structure is defined by the flamelet equations that are solved assuming unity Lewis number [132] in the reaction space:

$$\rho\frac{\partial Y_i}{\partial t} = \rho\frac{\chi_z}{2}\frac{\partial^2 Y_i}{\partial Z^2} + \dot{\omega}_i \tag{3.10}$$

$$\rho\frac{\partial h_s}{\partial t} = \rho\frac{\chi_z}{2}\frac{\partial^2 h_s}{\partial Z^2} + \dot{q}_s \tag{3.11}$$

where Y_i is the mass fraction of the species i, ρ is the density, Z the mixture fraction, $\dot{\omega}_i$ is the chemical source term of species i, h_s the sensible enthalpy and $\dot{q}_s$ the heat released by the chemical reactions. Eqns. 3.10 - 3.11 are solved in the flamelet space with a 1-D mesh with the finite volume method, by employing a stiff ODE solver to properly compute $\dot{\omega}_i$. Effects of mixing related to turbulence and flow-field are grouped into the scalar dissipation rate term χ_z expressed as:

$$\chi_z = \widehat{\chi_{st,j}}\frac{f\left(Z\right)}{f\left(Z_{st}\right)} \tag{3.12}$$

$f\left(Z\right)$ has an *erfc*-profile [133], while scalar dissipation rate at stoichiometric mixture fraction conditions $\widehat{\chi_{st,i}}$ for each flamelet is computed as an average of the local values in each CFD computational cell:

$$\widehat{\chi_{st,j}} = \frac{\int_V M_j \chi_{st,l}^{3/2}\rho\tilde{P}\left(Z_{st}\right)dV'}{\int_V M_j \chi_{st,l}^{1/2}\rho\tilde{P}\left(Z_{st}\right)dV'} \tag{3.13}$$

where P is a β-function, whose parameters depend on mixture fraction and its variance. In each cell $\chi_{st,l}$ is computed following the Hellstrom formulation [134]:

$$\chi_{st,l} = \frac{\chi}{\int_0^1 \frac{f(Z)}{f(Z_{st})}\tilde{P}\left(Z\right)dZ} \tag{3.14}$$

In such a formulation, TCI is embedded in sub-grid scale mixing and reaction of the fuel and oxidizer which is not considered in the MZWM model in §3.2.1. Fig. 3.2 summarizes the operation of the MRIF combustion model, illustrating the mutual interactions between the physical space and the reaction space. At each time-step, average stoichiometric scalar dissipation rate values are passed to each flamelet, that solves Eqn. 3.10-3.11 accordingly. The chemical composition in the physical space is computed from the mixture fraction, its variance and the flamelet marker distribution. Temperature is updated from new chemical composition and total enthalpy, whose variation

is only due to flow and spray evaporation. For further information, the reader is referred to [135].

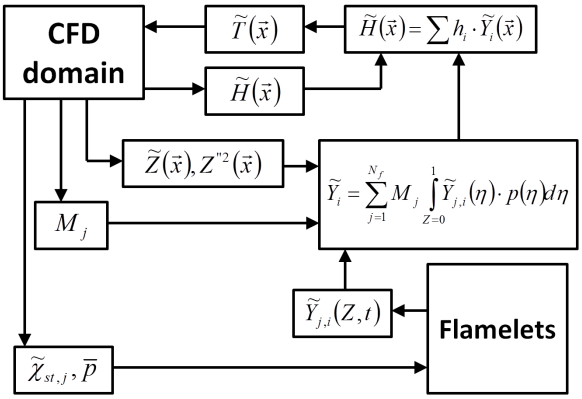

Figure 3.2: *Flowchart of MRIF model: interaction between flamelets and CFD domain.*

Discussed MZWM and MRIF models were applied as combustion models for reactive spray configurations of Chapters 5 and 6 and LTC modeling in Chapter 7.

CHAPTER 4

Non-Reacting Simulations and Air-Fuel Mixing

Accurate non-reacting liquid spray modeling is a demanding requirement of reactive simulations in constant volume vessels and CI Diesel engines configurations. Hence, non-reacting characteristics of liquid and vaporizing sprays should be closely evaluated with available experimental data. This is because reacting and combustion characteristics such as ignition and flame lift-off are directly affected by state of liquid fuel spray, breakup, atomization, vaporization and air-fuel mixing. Initiation of these processes is mainly due to high drag forces on liquid phase of the spray with high momentum. Aerodynamic forces result in growing of waves on the gas/liquid interface or of the whole droplet itself, which finally lead to disintegration and formation of smaller droplets. These droplets are again subject to further aerodynamically induced breakup [136]. Surface tension force on the other hand, tries to keep the droplet spherical and counteracts the deformation force. It depends on the curvature of the surface: smaller the droplet, bigger the surface tension force which leads to an unstable droplet deformation and to disintegration. This behaviour is expressed by *Weber* number which is the ratio of aerodynamic and surface tension forces:

$$We_g = (\rho_g \,.\, \mathbf{u}_{rel}^2 \,.\, d)/\sigma \tag{4.1}$$

where d is the droplet diameter before breakup, σ is the surface tension between liquid and gas, u_{rel} is the relative velocity between droplet and gas, and ρ_g is the gas density. For the discussion on the mathematical formulation of the governing sub-models see [38, 136].

4.1 Liquid and Vapor Penetration Length

Liquid and vapor penetration length are key parameters to ensure that LDEF simulations provide expected results for liquid spray and evaporated spray penetrations. In this thesis numerical thresholds for these parameters are considered as below:

- **Liquid Penetration Length:** Maximum distance of a Lagrangian parcel which has 95% mass of total liquid mass in a particular time-step.
- **Vapor Penetration Length:** If in a CFD cell, mixture fraction, *Z*, is larger than 0.001, maximum distance from the injector nozzle to the cell center fulfilling this threshold is considered as vapor penetration length.

4.2 Effects of Grid Alignment

Flame structure and pollutant formation in conventional and advanced combustion modes in Diesel engines are mainly determined by the characteristics of spray evolution and air-fuel mixing processes. Many efforts were carried out in order to improve available turbulence and spray models in CFD codes. However, enhancements in physical modeling can be drastically affected by how the CFD grid was structured. Grid quality can negatively influence the prediction of the organized charge motion structures, turbulence generation and interaction between in-cylinder flows and injected sprays. This was even more relevant for applied modern strategies in DI engines, where multiple injections and control of charge motions were employed. The first requirement for accurate DI engine simulations is the capacity to well describe fuel spray processes. As it was discussed before, liquid fuel sprays have been widely simulated by the use of LDEF with proper coupling of these two approaches. In Eulerian-Flow field point of view, further refinements in the size of a computational grid is desirable due to more accurate calculations of discretized differential equations and better resolved spatial

gradients of the flow quantities. However, here accurate spray simulations would not necessarily be resulted by applying finer grids due to inadequate space resolution of the velocity, temperature and vapor concentration of the fluid flow in the Eulerian phase. This hinders accurate Eulerian flow calculations in the vicinity of the injector nozzle where very high velocity and density gradients were presented. Introduced numerical diffusion by applying coarse and misaligned grids would be the main reason on inaccurate liquid and vapor penetrations and poor modeling of air-fuel mixing, no matter how accurate turbulence and spray sub-models were considered. By the experiments it has been known that high pressure Diesel spray has a conical morphology during its evolution, although it can be partially or fully deviated by engine swirl and counter squish flows of the piston bowl [137, 138]. Alignment of the computational mesh on the spray pattern can then ensure realistic spray mixing and morphology. Jing et al. [139] investigated the effect of three different combustion chamber geometries on combustion and emission characteristics of a DI Diesel engine. Spray oriented computational grid were generated to gain better accuracy of spray and combustion simulations. Similar studies using spray oriented grids were reported in several researches [140–143]. Imamori et al. [144] compared effect of polar and non-polar sector meshes on combustion characteristics of a Sandia optically accessible Diesel engine. Polar mesh and non-polar meshes were refined and higher mesh resolutions showed better agreement in terms of combustion and emission characteristics with the experimental data. Adaptive Mesh Refinement (AMR) scheme was used by a number of researchers [42, 145–147] with the objective to reduce the numerical diffusivity. Lippert et al. [148] performed a comprehensive study on momentum coupling of liquid and gas phases enabling accurate spray liquid penetrations for coarse meshes. They used adaptive mesh refinement on spray tip penetration simulations but no data was provided for air-fuel mixing and final evaporated spray structure by application of AMR. Most of the mentioned studies were closely examined spray sub-models, phase coupling and effect of mesh refinement on the spray and combustion predictions. However, less attention was given to the level of accuracy on the moment of final delivery of Lagrangian phase to the Eulerian phase in case of evaporated spray structure and air-fuel mixing. This could be a critical issue while modeling early injection engine operating modes such as partially premixed combustion. In such modes by applying coarse cells on axial direction and non-spray oriented grid alignment, inferior and highly reticulated predictions of the va-

porized spray structure and very poor modeling of the air-fuel mixing process would be resulted. This was noticeably far from actual evaporated spray morphology and can highly affect modeling accuracy of mixing and subsequent combustion and emission formation simulations. Multi-dimensional engine modeling of partially premixed combustion mode was investigated by a number of studies [149–153]; however, despite applying very early injections such as -90 CAD ATDC, no attention was given to the grid alignment and its essential effect on air-fuel mixing.

Aim of the this section of the thesis is to introduce a novel approach base on applying a conical mesh structure in order to get reliable predictions on air-fuel mixing, equivalence ratio, and scalar dissipation rate distributions within the combustion chamber of DI Diesel engines.

4.2.1 Numerical Simulation

Multi-dimensional CFD simulations were conducted and LDEF was used in the spray simulations with proper 'gas-to-liquid' and 'liquid-to-gas' coupling sequences. Interpolation process at the parcel locations where the gas quantities were estimated was taken into account in the former sequence. The latter sequence refers to the summation of the particle source terms in the Eulerian conservation laws. For the detailed descriptions of Eulerian and Lagrangian governing equations, their coupling, discretizations, and solution approaches the reader was referred to [42, 154]. Although reacting flow and combustion modeling was not considered in this study, solution of transport equations for Z as mixture fraction (Eq.3.4) and Z'' as its variance (Eq.3.5) was also performed along with mass, momentum and energy conservation equations together with turbulence (RANS) to evaluate how grid structure might affect the mixing process.

4.2.2 Simulation Case Properties and Mesh Types

In order to show maximum level of agreement between numerical non-reacting simulations with available experimental data, published experiments of Singh et al. [43] were used. Four stroke Cummins DI Diesel engine was used where the optical access to the combustion chamber was provided by an extended piston and flat piston-crown window and imaging access was provided through one of two exhaust valves in the cylinder head. Type 2 Diesel fuel has been used in the experiments whose properties were provided in Table 4.1. Different modes of combustion were investigated by mak-

ing changes in the extent of dilution and the relative difference between duration of injection and ignition delay [43, 155]. Two laser beams overlapped and directed in a form of less than 1mm thick laser sheet into the combustion chamber in a way to capture images from the chamber at a slope of 14° from the fire deck. This angle was the spray injection angle with respect to the fire deck, so the attempt was to capture the laser sheet images on the axis of the spray [156].

Table 4.1: *Properties of ultra-low sulfur 2007 emissions certification type 2 Diesel fuel [43].*

Total aromatics by volume	27%
Olefins	0.5%
Saturates	72.5%
Sulfur (by weight)	9.1 ppm
Distillation temperatures	
Initial boiling point	190°C
10% Distillation temperature	212°C
50% Distillation temperature	254°C
90% Distillation temperature	315°C
End point	350°C
Cetane number	46
Specific gravity @ 20°C	0.8426
C/H by weight	6.5
Net heat of combustion	43MJ/kg
Viscosity @ 40°C	2.35cS

In the present study, mesh generation and multi-dimensional simulations were performed on the engine specifications and experimental case properties listed in Table 4.2 and Table 4.3, respectively. Summary of applied sub-models for the non-reacting simulations is provided in Table 4.4.

Specifications of four types of computational grids were presented in Table 4.5. After grid generation, all meshes were checked on a closed cycle simulations, from IVC to EVO, to have a same compression ratio as of the Sandia optical engine. Assuming symmetrical combustion chamber geometry, polar Cartesian 45° sector Coarse Mesh was generated and periodic boundary conditions were assumed on side faces. Fine Mesh was simply generated by refining the Coarse Mesh in radial, azimuthal, and axial directions. These grids were shown in Fig.4.1.a. It was discussed that spray morphology can be enhanced by aligning the grids on the spray axis. This approach was used to

Table 4.2: *Sandia optical engine specifications taken from [43].*

Engine base type	Cummins N-14 DI Diesel
Number of cylinders	1
Combustion chamber	Quiescent, DI
Swirl ratio	0.5
Bore × Stroke	13.97 × 15.24cm
Bowl width × depth	9.78 × 1.55cm
Displacement	2.34l
Connecting rod length	30.48cm
Geometric compression ratio	11.2:1
Fuel injector, no. of holes	Common-rail, 8
Spray pattern included angle	152°
Injection pressure	1200/1600bar
Nozzle orifice diameter	0.196mm
Nozzle orifice, L/D	5

Table 4.3: *Properties of the experimental cases for non-reacting simulations taken from Ref. [43].*

	Low-Temp. Late Inj.	High-Temp. Long Ign. Del.	Low-Temp. Early Inj.
Engine speed [rpm]	1200	1200	1200
IMEP [bar]	4.1	4.5	3.9
Injection pressure [bar]	1600	1200	1600
Intake temperature [K]	343	320	363
BDC temperature [K]	351	335	365
Intake pressure [bar]	2.02	1.92	2.14
TDC motored temperature [K]	840	800	870
TDC motored density [kg/m^3]	22.5	22.3	22.9
SOI [CAD ATDC]	0	-5	-22
DOI [CAD]	7	10	7
Injection quantity [mg/cycle]	56	61	56
O_2 concentration [vol.%]	12.7	21	12.7

generate a polar Spray Oriented Mesh whose total cell count was less than Fine Mesh. Spray Oriented Mesh was represented in Fig.4.1.a. In order to get much closer to the conical spray structure, the Conical Mesh shown in Fig.4.1.a was generated. Presence and geometry of injector in the combustion chamber was also taken into account (red circle in Fig.4.1.a). A closer view of mesh alignment near the nozzle orifice area was provided in Fig.4.1.b for the Conical Mesh. In Fig.4.1.a cyan colored parts were the

Table 4.4: *Summary of applied sub-models/calculation schemes and their properties on multi-dimensional non-reacting Diesel engine simulations*

Modeling/calculation of	Applied sub-model/scheme	Sub-model/scheme properties
Turbulence	Standard k-ϵ model	Coefficients: C_μ=0.09, C_1=1.44, C_2=1.92, C_3=-0.33
Injection	Huh-injector model [157]	Initial droplet diameter = nominal orifice diameter, C_d=0.8
Spray atomization	Huh-Gosman model [157]	Coefficients: C_1=2.0, C_2=0.5, C_3=1.0, C_4=3.0, C_5=0.6, Weber limit = 40
Spray breakup	Kelvin-Helmholtz model [158]	B_0=0.61, B_1=10, Weber limit = 6
Spray evaporation	Spalding [42]	D^2-law with relaxation times calculated under standard and boiling conditions
Heat-transfer	Ranz-Marshall [42]	Semi-implicit method for solving droplet energy equation

result of splitting the grids on injection axis to show a normal view of the mesh alignments in introduced meshes types. It should be noted that during compression and expansion processes, cells were removed and added in both Coarse and Fine Mesh on a flat plate over the bowl, whereas in Spray Oriented and Conical Meshes, cell layers were removed and added on a V shaped surface. Cell add/removal layer was shown with a yellow line in Fig.4.1.a which for Spray Oriented and Conical Meshes allows keeping the cells fixed at TDC and compress/expand the cells below them. This is a noticeable advantage while simulating engine cases with an early injection such as partially premixed combustion modes or multiple injections.

Table 4.5: *Specifications of the applied computational grid in the non-reacting spray simulations.*

Mesh type	Coarse Mesh	Fine Mesh	Spray Oriented Mesh	Conical Msesh
Number of cells on azimuthal, radial, and axial directions at TDC	21×67×11	31×77×23	21×77×27	17×variable×variable
Total number of cells at TDC	15,477	54,901	43,659	78,482
Minimum cell volume at TDC [mm^3]	0.0206	0.00494	0.00287	0.00011
Maximum cell volume at TDC [mm^3]	6.12	3.67	5.89	6.95

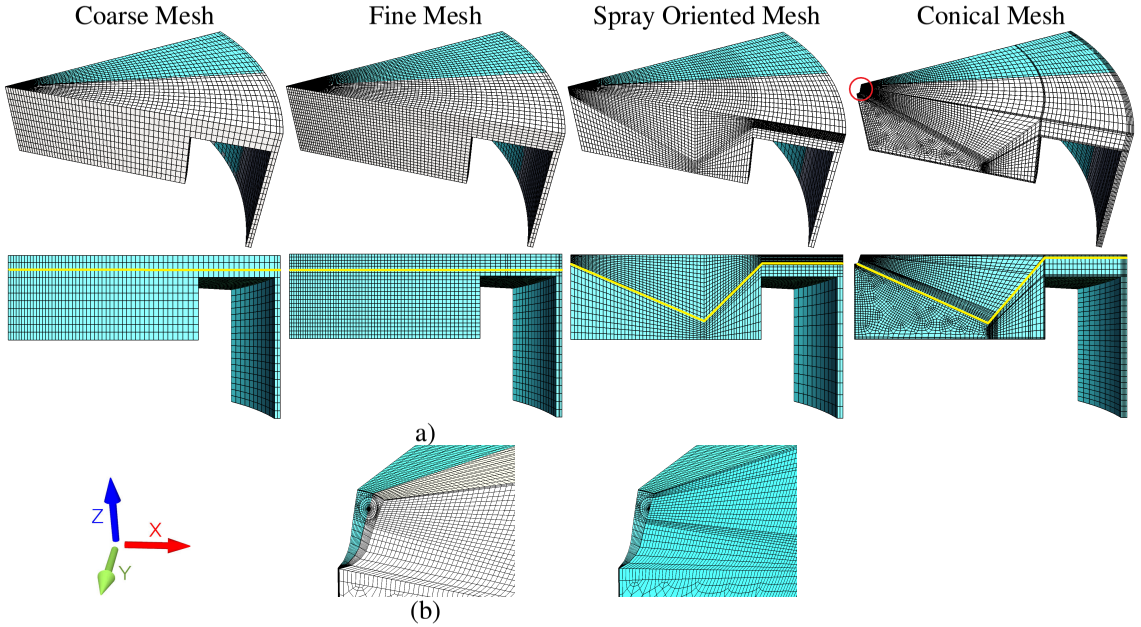

Figure 4.1: *a) Coarse Mesh, Fine Mesh, Spray Oriented Mesh, and Conical Mesh generated for Sandia optical engine geometry. b) Closer view to the cell alignment of Conical Mesh near the nozzle orifice location, cyan color shows radial alignment of cells on the spray axis (14° below the fire deck).*

4.2.3 Spray Behavior Near the Injector Nozzle

It has been discussed that LDEF approach cannot accurately predict momentum exchange between Lagrangian droplets and Eulerian Flow in vicinity of the injector nozzle when the Discrete Droplet Method (DDM) was applied. Instead, atomization submodels were needed to capture the churning flow very close to the nozzle orifice if dense spray near to the nozzle was not modeled by means of Continuous Droplet Method [159]. Huh-Gosman injector and atomization models were applied taking into account effects of churning flow close to the injector nozzle. Depicting the results, three critical planes of spray injection were shown in Fig.4.2 as Plane I, II and III. These planes will be used to further discuss the results on different aspects. Normal vector of the Plane III is parallel to injection direction vector and in this sub-section assumed to be located in a distance of 4mm from the nozzle orifice. Faeth [159] by experimental observations has shown that liquid core of the spray, L_{fc}, can be estimated by Eq.4.2.

$$L_{fc}/d \;=\; C_c(\rho_f \;/\; \rho_\infty)^{1/2} \tag{4.2}$$

Where d is injector diameter, C_c is a constant and ρ_f and ρ_∞ are fuel and ambient air densities, respectively. For the applied fuel in this study Eq.4.2 yields in liquid core length of 8.2 mm. Hence distance of 4mm from the nozzle orifice was considered to locate the Plane III within the region where the churning flow is dominant. Figure 4.3 shows the grid density function (cell vertices) of Eulerian phase velocities in x, y, and z directions with respect to distance from the cross point of injection axis with the Plane III as independent variable for the applied grids. Results of grid types were also compared with Abani's Gas-Jet model [160] as reference. This zero dimensional model evaluates spray-tip penetration for transient injection velocity profiles based on gas-jet theory that is consistent with Helmholtz's vortex-model. Number of cell vertices for the Conical, Spray Oriented, Fine and Coarse Mesh types on the Plane III with the distance of 4 mm from the nozzle orifice were: 1521, 724, 1022, and 448, respectively. Velocities were shown for 3 CAD ATDC as the mid of injection duration where the highest liquid fuel mass flow rate takes place. Highest velocities were reported for Ux comparing to velocities in y and z coordinates as the injection axis was just 14° below the fire deck and makes a low angle with the x coordinate. In view of magnitudes of Ux, the Conical Mesh predicts the most similar velocity distributions with Gas-Jet theory

comparing to other grid types showing lower numerical diffusion. Moreover, it can be seen that there were more distributions for higher *Ux* velocities for Conical Mesh than other grid types which can suitably take the effect of churning flow into account without directly modeling it through DDM. It is interesting to notice that although grid density on Plane III for Spray Oriented Mesh was almost 30% less than Fine Mesh, the former mesh type managed to better capture both higher *Ux* peak and distribution near the cross point with injection axis. The highest momentum diffusion was reported for the Coarse Mesh where for the distances more than 1 mm it had more density for higher *Ux* velocity. On the *y* coordinate, symmetrical distributions of *Uy* velocities were resulted for all grid types, whereas in *z* coordinates similar behavior discussed for *x* coordinates were resulted and Conical and Spray Oriented Mesh types represent lower numerical diffusion in vicinity of injector nozzle. In addition, more densities of higher velocities were resulted for Conical Mesh due to effective radial grid distribution showing the best agreement with the results of Gas-Jet theory.

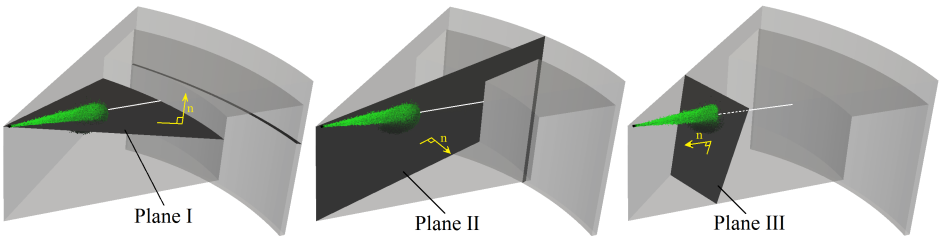

Figure 4.2: *Geometrical surfaces to extract numerical data. White line: Spray injection direction.*

4.2.4 Liquid and Vapor Penetration Length and Distribution

Singh et al. conducted spray liquid and vapor penetration length measurements on Sandia optical engine [43] for different modes of combustion and have taken ten sample for penetration distances in each engine crank angle. A comparison of their experiments on the Low-Temperature Late-Injection case with the numerical predictions of four mesh types was shown in Fig.4.4. Paying attention to the experimental results, it can be seen that there was a high level of cycle-to-cycle variations in the penetration length distances of ten samples in a particular crank angle. This was more pronounced for liquid penetration length at 5 CAD ATDC where the penetration length of maximum sample distance was almost twice of minimum sample. The reason for this behavior

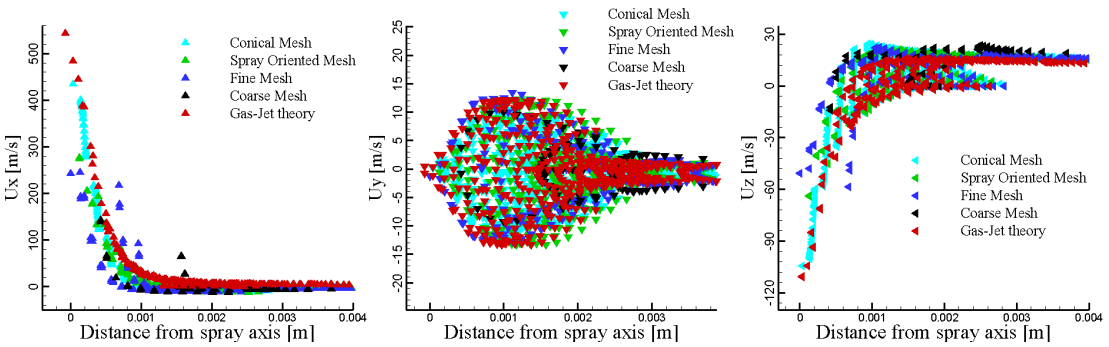

Figure 4.3: *Grid density function of Eulerian phase velocities of Ux, Uy, and Uz on plane III (located at 4mm distance from the nozzle orifice) with respect to distance from the cross point of injection axis and Plane III compared to the results of Gas-Jet theory.*

can be due to high and variable level of turbulence within the combustion chamber in different cycles. Numerical simulations show acceptable trend in prediction of both liquid and vapor penetration lengths where the best agreement with the experiments for the applied DOI was achieved by the Conical Mesh. Figure 4.4 also depicts noticeable difference on prediction of liquid and vapor penetrations between Coarse and Fine Meshes, whereas the results for Spray Oriented and Conical Meshes were very close to each other. This can be discussed in a way that spray momentum was highly diffused to the vertices of the Coarse Mesh resulting in the minimum penetration predictions. By refining the grid for the Fine Mesh, better results were obtained due to closer vertices to the Lagrangian parcels and lower spray momentum loss. Further enhancement of predictions in Spray Oriented and Conical Meshes, however, was not based on possessing higher cell count but on their alignment. As it was mentioned in §4.2.2, Spray Oriented Mesh has lower cell count compared to the Fine mesh but its predictions show higher accuracy than the latter mesh type. This was mainly because Lagrangian parcels were spread in a higher number of cells in Fine Mesh causing higher momentum diffusion to the low momentum Eulerian cells during the Lagrangian-Eulerian coupling and finally reduction in the liquid and vapor penetration lengths. This would also affect the final delivered amount of evaporated fuel to an Eulerian cell, air-fuel mixing, and equivalence ratio distributions within the combustion chamber.

Simulations are conducted for two more engine operating conditions of High Temperature Long Ignition Delay and Low-Temperature Early-Injection. Properties of

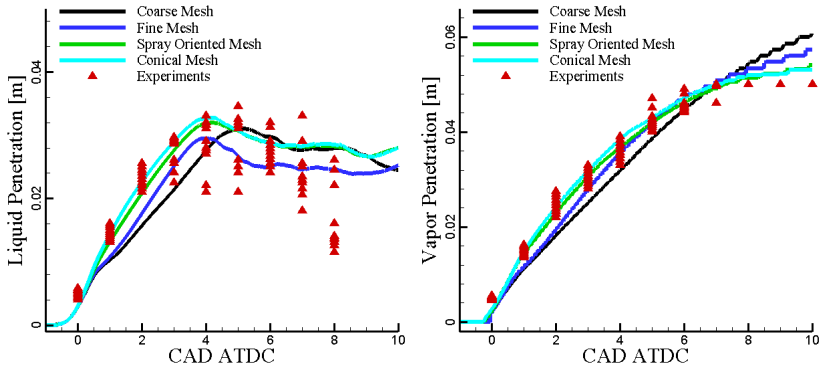

Figure 4.4: *Liquid and vapor penetration length comparisons between experiments of Singh et al. [43] and numerical simulations of Low-Temperature Late-Injection case using four mesh types.*

these two cases were represented in Table 4.3. Non-reacting simulation results of liquid and vapor penetrations were shown in Fig.4.5. It should be noted that experimental results were extracted under reacting conditions where heat release due to combustion was started at 1 and -17 CAD ATDC in High-Temperature Long Ignition Delay and Low-Temperature Early-Injection cases, respectively. Simulation results for liquid and vapor penetration lengths, however, were compared from start of injection up to these engine crank angles. Acceptable agreements in both cases were resulted by using the Conical Mesh.

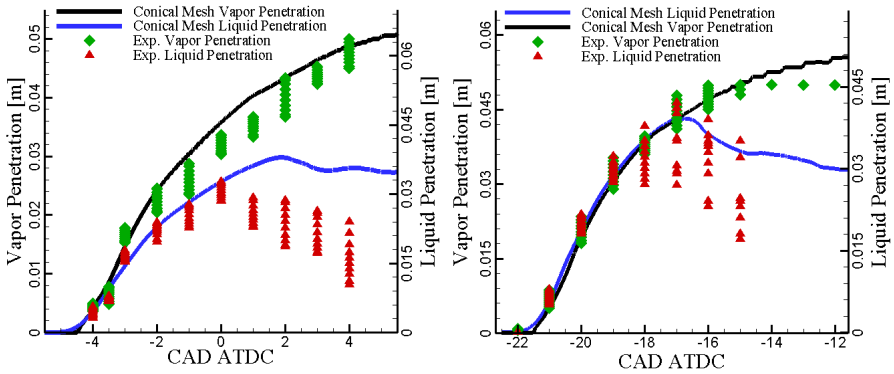

Figure 4.5: *Liquid and vapor penetration length comparisons between experiments of Singh et al. [43] and numerical simulations of High-Temperature Long Ignition Delay (left) and Low-Temperature Early-Injection (right) cases using the Conical Mesh.*

Figure 4.6 compares the simulation results of liquid droplets (blue) and gaseous fuel (green) distributions of Low-Temperature Late-Injection case using the four analyzed mesh types at 0, 2, 4, and 6 CAD ATDC with the experimental images. It should be noted that to capture experimental images, the laser sheet was directed with the slope of 14° from the fire deck (injection angle) and later normal views of this plane were used to represent them. Similarly, normal views were selected to compare simulation results with the experiments of Singh et al. [43] for the Low-Temperature Late-Injection case in Fig.4.6. As it can be seen, evolution of spray in the assigned DOI was well captured by both Spray Oriented and Conical Meshes where the latter mesh type shows the best agreement with the experiments. Results of liquid and gaseous fuel penetrations in Fig.4.4 were shown tangible reduction when Coarse and Fine Meshes were applied. This coincides with the images of Fig.4.6 where comparing to Conical and Spray Oriented Meshes, noticeably lower penetration lengths were resulted in Coarse and Fine Meshes. This behavior is because of higher drag forces on Lagrangian droplets as they face coarse Eulerian cells that were not oriented on the injection axis. Moving from the Coarse Mesh to the Conical Mesh in all the crank angles in Fig.4.6, denser liquid core predictions were resulted. In Lagrangian droplet point of view, higher velocity loss was occurred in a fuel droplet in the Coarse Mesh resulted in accelerated evaporation and diameter reduction due to its lengthy disposal to the hot Eulerian gas flow. In Eulerian gas point of view, only cells near to the nozzle orifice gain high momentum in the Coarse Mesh. This is due to coarser cell dimensions and they were subjected to a large number of Lagrangian droplets. Accumulation of these two effects has resulted both in having sparser liquid core and shorter liquid and gaseous fuel penetrations in coarse and non-spray oriented grids.

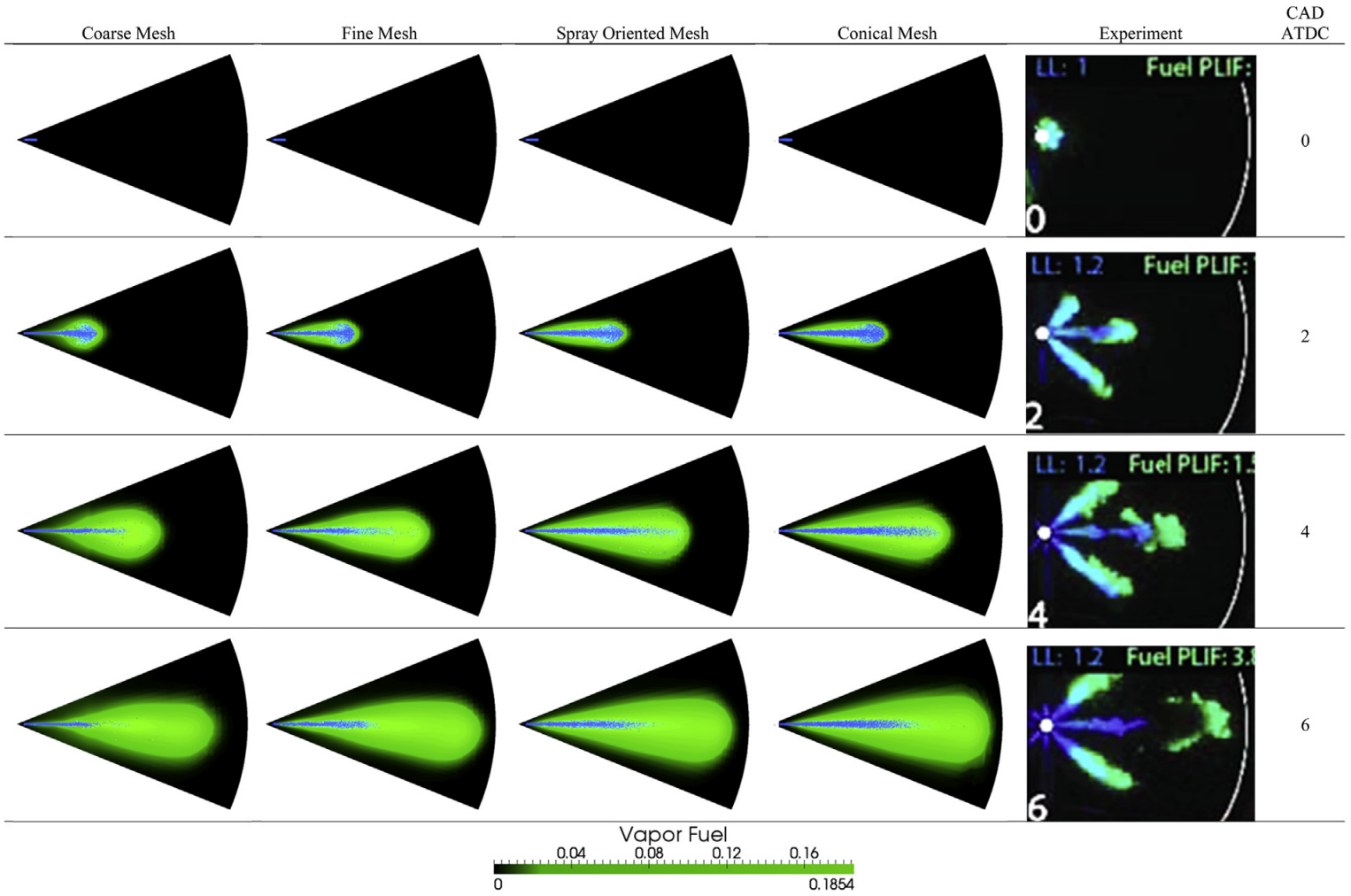

Figure 4.6: *Simulation results of liquid fuel particles (blue) and vaporized fuel mass fraction (green) distributions for Low-Temperature Late-Injection case on the plane of spray injection axis for four mesh types at 0, 2, 4, and 6 CAD ATDC compared to the experiments of Singh et al. [43]*

4.2.5 Equivalence Ratio Distribution

Plane I

Figure 4.7 shows equivalence ratio distributions on Plane I for the applied mesh structures at 3 CAD ATDC as the mid of DOI. It can be seen that equivalence ratio distribution was highly affected by mesh types. Moving on the injection axis from the Coarse Mesh to the Conical Mesh, less equivalence ratio was resulted in the spray tip. For Plane I this behavior can be discussed together with the results of liquid and vapor fuel distributions in Fig.4.6. Higher penetrations and lower spray momentum losses were resulted due to the enhanced mesh alignment and finer mesh structure in the Spray Oriented and Conical Meshes where such a trend was not reported in Coarse and Fine Meshes. At 3 CAD ATDC (mid of DOI) predicted particle velocities out of the injector orifice were the highest due to the injection profile [43]. These high momentum particles which newly introduced to the spray tail have less participation in mixing process as they need time to undergo the breakup, diameter reduction and evaporation processes. Taking high momentum particles in the spray tail and low momentum particles in the spray tip into consideration, it was expected equivalence ratio to increase from tail to tip. This trend was pronounced in Coarse and Fine Meshes due to higher momentum reduction in the spray tip and higher gradients of equivalence ratio were resulted comparing to Spray Oriented and Conical Meshes. Advantage of Spray Oriented and Conical Meshes was represented in Fig.4.7 for 3 CAD ATDC as mid time of injection duration. Results show that cross section on three dimensional equivalence ratio distributions using the Plane I was much closer to the actual conical spray structure comparing to the Coarse and Fine Meshes. It should be noted that mesh alignments in Coarse and Fine Meshes introduces poor and reticulated evaporated spray structure which is also shown in Fig.4.7 by representing the computational cells making up equivalence ratio cross section on Plane I. This is a critical stage if later combustion simulations of the reacting flow would be conducted.

Plane II

Equivalence ratio distributions of four mesh types were shown in Fig.4.8 on the cross section of Plane II. Poor evaporated spray structure was resulted in Coarse and Fine Meshes, whereas proper mesh alignment in Spray Oriented and Conical Meshes was led to much lower departure from conical structure. Computational cells which occupy

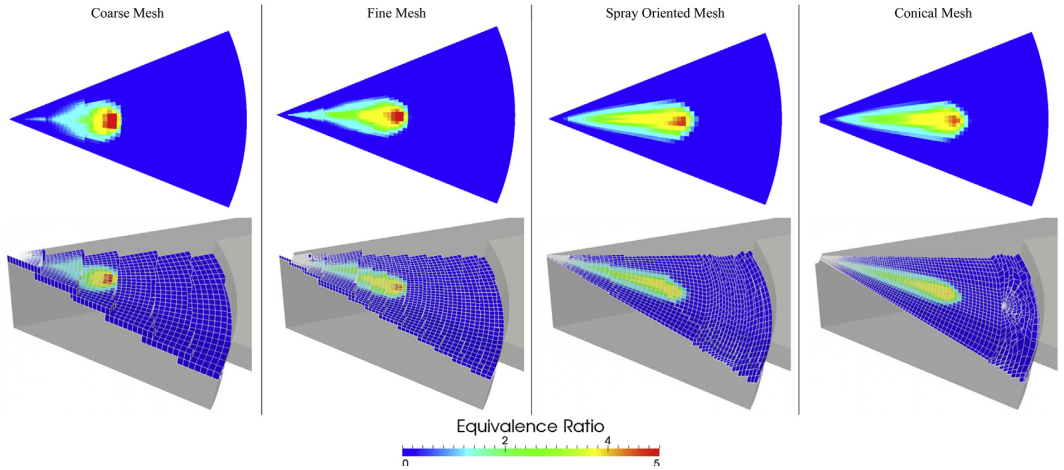

Figure 4.7: *Equivalence ratio distributions of four mesh types on a normal view of Plane I at 3 CAD ATDC. Bottom: Computational cell alignments within the combustion chamber on the Plane I to capture equivalence ratio distributions in the top row*

the volumes on Plane II cross section also show that applying Cartesian type of mesh alignment in Coarse and Fine Meshes would be resulted in more reticulated equivalence ratio distributions. It should be noted that by further refining the Fine Mesh, it is possible to get closer to the conical structure but Spray Oriented Mesh was already fulfilled this with lower number of cells comparing to the Fine Mesh.

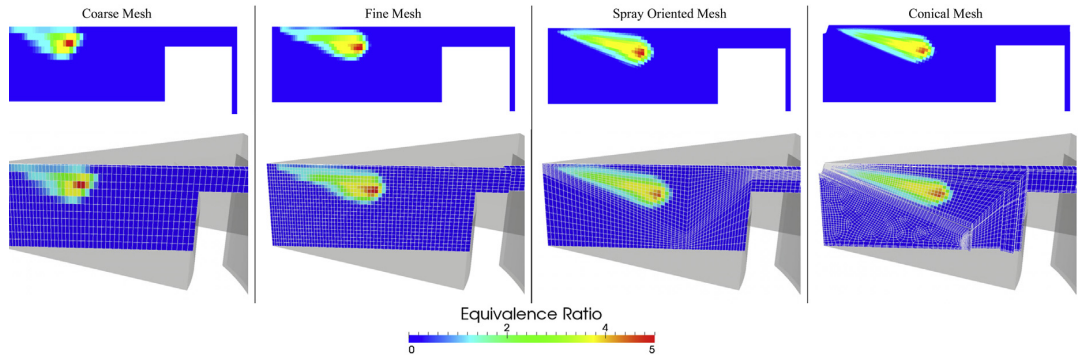

Figure 4.8: *Top: Equivalence ratio distributions of four mesh types on a normal view of Plane II at 3 CAD ATDC. Bottom: Computational cell alignments within the combustion chamber on the Plane II to capture equivalence ratio distributions in the top row.*

Plane III

Geometrical orientation of the Plane III was shown in Fig.4.2. Keeping the normal vector of the Plane III constant, Fig.4.9 (left) shows planes A, B, and C which were made by distances of 1, 1.5, and 2.5cm from the nozzle orifice on the injection axis, respectively. Results of equivalence ratio distributions for these planes using four mesh types were depicted in Fig.4.10 at 3 CAD ATDC. Results show that only Conical Mesh alignment is capable of predicting accurate radial equivalence ratio distributions on the planes A, B, and C forming concentric circles around the injection axis. For instance, in all planes of the Coarse Mesh very poor distributions of equivalence ratio were resulted. Fine and Spray Oriented Meshes had better results comparing to the Coarse Mesh; however, equivalence ratio distribution was highly reticulated. This behavior was resulted from the mesh alignment which was also shown by the cells occupying the cross sections of the Plane C.

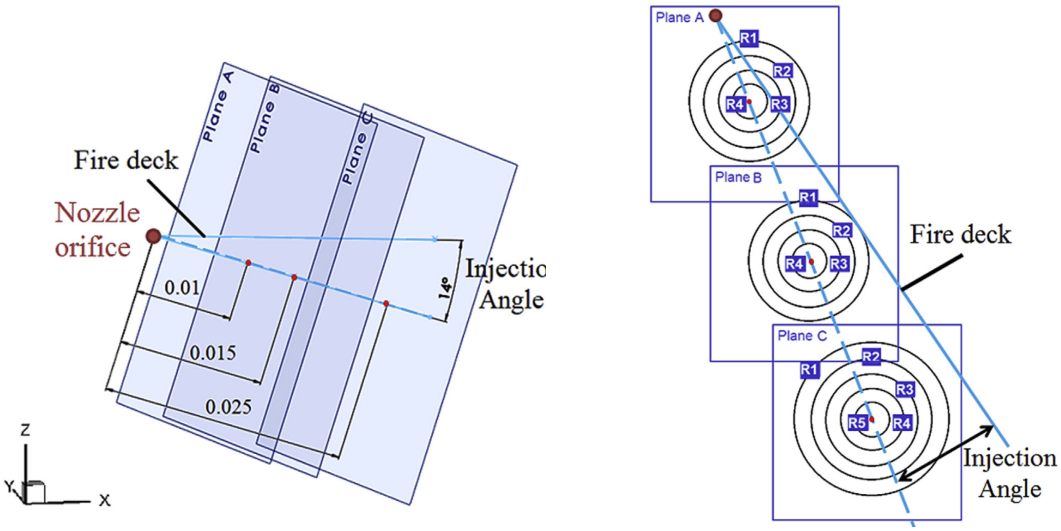

Figure 4.9: *Left: Planes A, B, and C parallel to the Plane III (Fig.4.2) with the distances of 10, 15, and 25mm from the nozzle orifice, respectively. Right: Positions of R1-R4 in Planes A and B and R1-R5 in Plane C. Plane A: R1=2mm, R2=1.5mm, R3=1mm, and R4=0.5mm. Plane B: R1=3mm, R2=2mm, R3=1mm, and R4=0.5mm. Plane C: R1=5mm, R2=4mm, R3=3mm, R4=2mm, and R5=1mm.*

In order to discuss the magnitude of equivalence ratio distribution on Plane A, B, and C, four circles, R1-R4, were considered on Plane A, and B and five circles, R1-R5, on Plane C as shown in Fig.4.9 (right). Simulated equivalence ratio data were sampled

on twelve equally distanced points on the circles on the Planes A, B, and C and were shown in Fig. 4.11 for four mesh types at 3 CAD ATDC. Sampled data for these points was colored by magnitude of equivalence ratio and was shown using spheres at the points on the circles R1-R4 in Planes A, and B, and R1-R5 in Plane C. Using new $x' - y'$ coordinate systems diagrams in Fig.4.11 show tangible fluctuations of equivalence ratio magnitude in Coarse and Fine Meshes when compared to their corresponding circles in the Spray Oriented and Conical Meshes. It should be noted that relations between points on circles were not linear this is why dashed lines were used to link the spheres together. Figure 4.11 also shows that larger the momentum decay, higher the magnitude of equivalence ratio which coincides with the discussions on the previous sections.

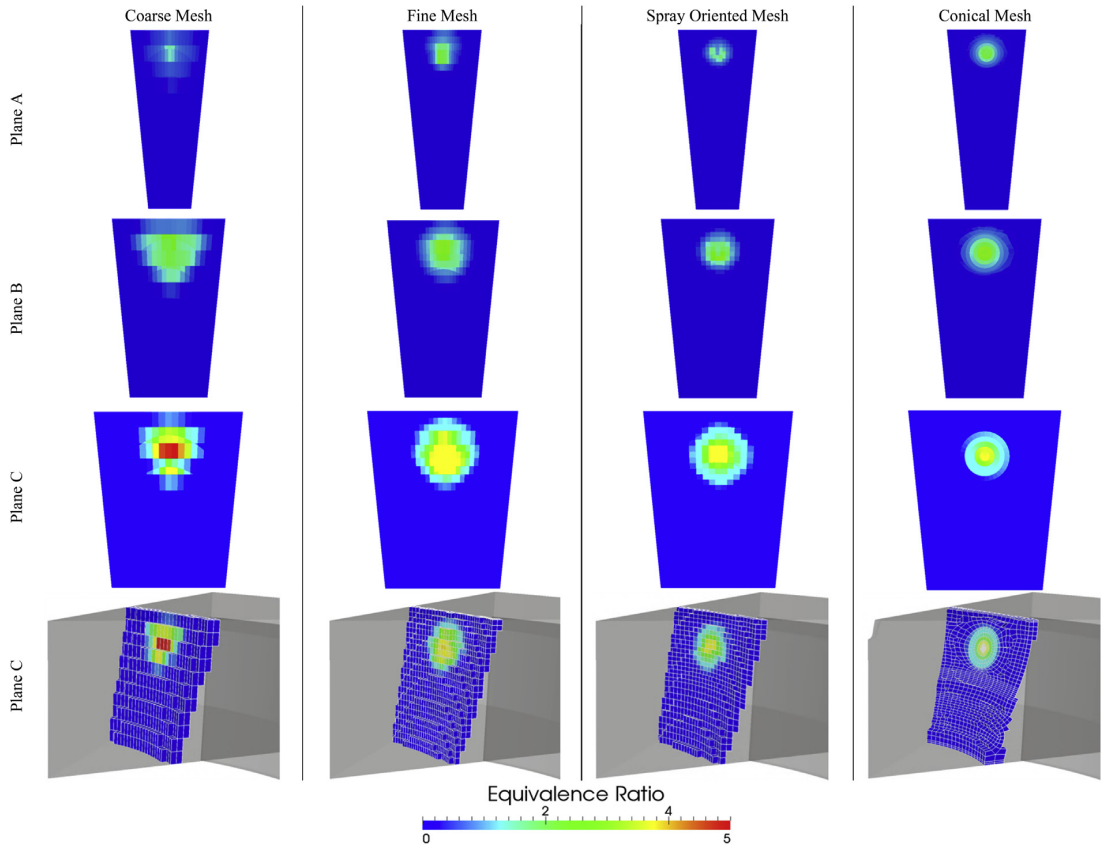

Figure 4.10: *Three top rows: Equivalence ratio distributions of four mesh types on a normal view of Planes A, B, and C at 3 CAD ATDC. Bottom: Computational cell alignments within the combustion chamber on the Plane C.*

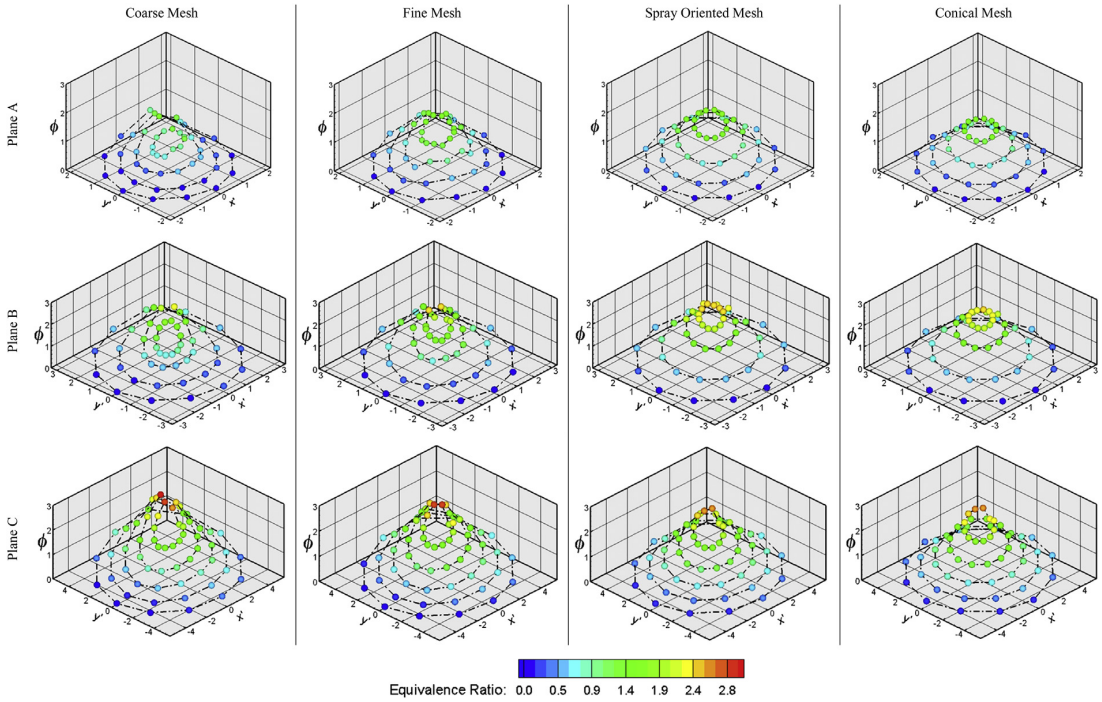

Figure 4.11: *Equivalence ratio magnitudes of R1-R4 on Planes A and B, and R1-R5 on Plane C at 3 CAD ATDC for four mesh types*

4.2.6 Scalar Dissipation Rate Distributions

Flame structure can be altered due to change in the values of scalar dissipation rate, $\hat{\chi}$, as it is directly related to the preparation of combustible mixtures and chemistry-turbulence interactions. Figure 4.12 represents magnitudes of scalar dissipation rate for the considered circles on Plane A, B, and C at 7 CAD ATDC (end of DOI). As this engine crank was the end of injection process, magnitudes of scalar dissipation rate would play a key role on heat release rate and emission formation if the reacting flow simulations would be conducted. It can be seen that lower values for $\hat{\chi}$ were resulted at the end of injection for the Coarse Mesh, whereas a similar trend was not observed for three other mesh types. On the other hand, both 3D and 2D diagrams show less variation of scalar dissipation rate magnitudes by moving from the Coarse Mesh to the Conical Mesh. This would be resulted in more uniform flame structure in Conical Mesh and it is acceptable due to low swirl combustion chamber of Sandia optical engine. It can be concluded that by applying conical grid alignment lower numerical diffusion

was resulted in vicinity of the injector nozzle where the churning flow takes place and spray morphology was enhanced downstream in evaporated spray region which showed less departure from the actual conical structure in the experiments. Higher magnitudes of equivalence ratio were resulted in early crank angles after initiation of injection process in Coarse and Fine Meshes. This was mainly due to high momentum diffusion and spread of Lagrangian particles to the large number of computational cells in Coarse and Fine Meshes, respectively. Similar trend was not observed for Spray Oriented Mesh with lower cell count comparing to the Fine Mesh. Application of coarser and non-spray oriented grid alignments was resulted on both reticulated evaporated spray simulations and unacceptable early evaporation due to over estimations on momentum diffusion and lowered Lagrangian particle velocity and higher liquid fuel diameter reduction. Both Spray Oriented and Conical Meshes showed acceptable results for liquid and gaseous fuel penetration lengths. However, predictions for spray morphology on radial distances from the injection axis showed acceptable trend only for Conical Mesh alignment of the grids.

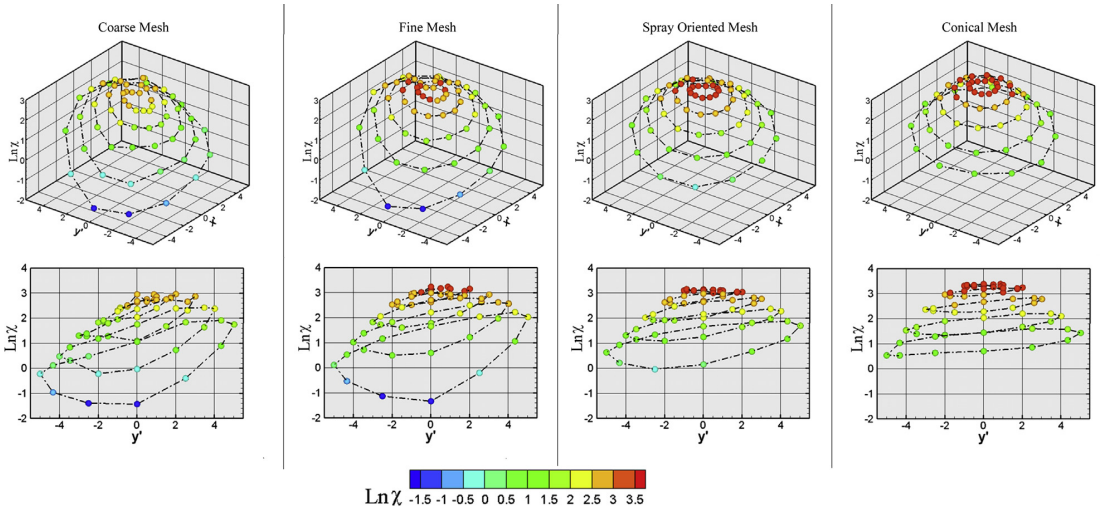

Figure 4.12: *3D and 2D diagrams for scalar dissipation rate magnitudes of R1eR4 on Planes A and B, and R1-R5 on Plane C for four mesh types at 7 CAD ATDC.*

4.3 Uncertainties

Non-reacting spray simulation results can be subjected to uncertainties just before the start of injection. Generally, liquid spray simulations within a high pressure chamber or IC engines is decoupled with injector nozzle internal flow as they differ in time and length scales. Injected amount of mass and injection profile (mass based or velocity based) are provided for CFD solvers and this way injector nozzle internal flow is not taken into account. This can be source of uncertainties and care must be taken. Next section will discuss the effect of cavitation on spray breakup and air-fuel mixing.

4.3.1 Effects of Cavitation

Late injection combustion, as an alternative combustion mode, was favorable where combustion was more closely coupled to the injection event offering more direct control over combustion phasing. Nonetheless, if injected fuel in the late injection combustion mode was not mix rapidly, fuel rich regions would be created leading to higher levels of soot emission. Genzale et al. [161] investigated the impact of spray targeting on the mixture evolution and combustion of a late-injection heavy-duty Diesel engine under low temperature combustion operating conditions. Laser sheets were used to illuminate thin layers in the combustion chamber and optical access was provided to a Sandia Diesel engine. Unique jet-wall and jet-jet interactions were resulted by applying three different injector nozzles angles. They concluded that weaker jet-wall and jet-jet interactions were achieved with a wide injection angle which may cause bulk flows to stagnate and hinder late-cycle mixing processes. By contrast, in narrow-angle injection the jet momentum was redirected up along the bowl-wall suppressing the formation of rich regions due to jet-jet interaction. This reduced soot formation and enhanced bulk-flow mixing late in the combustion cycle. Diesel engine multi-dimensional simulations of low temperature late injection combustion was conducted also by Genzale et al. [162] on the same configuration. Numerical results show that spray-targeting strategy can significantly alter the jet interactions with the jet-bowl and with neighboring jets, influencing the entire combustion. In this part of the thesis, extensive numerical simulations were conducted based on experiments of Genzale et al. [140].

4.3.2 Experimental Setup, Combustion Chamber Grids and Non-reacting Simulations

A single-cylinder optically-accessible heavy-duty DI engine was used to perform the experiments by Genzale et al. [140, 161]. Specifications of the Sandia engine were summarized in Table 4.6.

Table 4.6: *Sandia optical engine specifications taken from [161].*

Engine base type	Cummins N-14 DI Diesel
Number of cylinders	1
Combustion chamber	Quiescent, DI
Swirl ratio	0.5
Bore $\times$ Stroke	13.97 $\times$ 15.24cm
Bowl width $\times$ depth	9.78 $\times$ 1.55cm
Displacement	2.34l
Connecting rod length	30.48cm
Geometric compression ratio	11.2:1
Fuel injector, no. of holes	Common-rail, 8
Spray pattern included angle	152°
Injection pressure	1200/1600bar
Nozzle orifice diameter	0.196mm
Nozzle orifice, L/D	5

Three piston designs were considered in the experiments with piston bowl diameters of 60%, 70% and 80% of the cylinder bore where for each bowl design, injector spray angle was selected so that the nominal spray axis intersected the vertical midpoint of the bowl wall while piston is at TDC. For the 60%, 70%, and 80% piston bowls, the spray included angles were 140°, 152°, and 160°, respectively. Experiments were conducted for reacting and non-reacting conditions where non-reacting conditions were achieved by using pure N_2 in the intake charge. *PRF29* was used in the experiments and addition of 1% of toluene by volume provided a tracer for measuring fuel concentration. Laser sheets were used to capture images of the tracer enabling equivalence ratio measurements during the non-reacting experiments. Three different horizontal laser sheets were considered as it is depicted in Fig. 4.13 and experiments of different bowl geometries were performed for the initial conditions of Table 4.7. Computational mesh generation was carried out for three bowl geometries in this study. Spray oriented meshes were

generated, Fig. 4.13, and used in the spray simulations of this study.

Table 4.7: *Low temperature late injection case specifications [161].*

Engine speed [rpm]	1200
Indicated mean effective pressure [bar]	4.1
Injection pressure [bar]	1600
Intake temperature [K]	343
BDC temperature [K]	351
Intake pressure [bar]	2.02
TDC motored temperature [K]	840
TDC motored density [kg/m^3]	22.5
SOI [CAD ATDC]	0
DOI [CAD]	7
Injection quantity [mg/cycle]	56
Injector nozzle	Sharp edge, not rounded

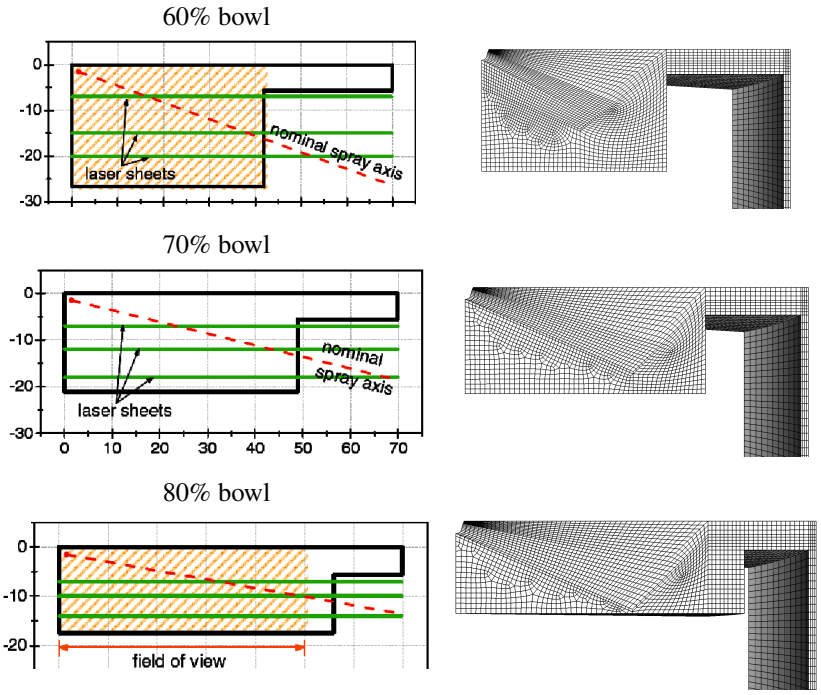

Figure 4.13: *Left: Laser sheet locations in three piston bowl geometries and injection angles in experiments of Genzale et al. [161]. Right: Spray oriented meshes generated for three bowl geometries*

Simulation for non-reacting conditions was first conducted for the engine base bowl geometry [140] of 70% and compared with experimental results in Fig. 4.14 for three laser sheets, 7mm, 12mm, and 18mm at 7CAD ATDC. However, it can be seen that simulation results in case of location of the rich equivalence ratio regions and magnitude have considerable discrepancy with the experiments. As PRF29 is used in the experiments and injector had sharped edge configuration, it was probable that cavitation occurred during the injection process. Number of researches has shown that cavitation can deviate spray shape and highly affect its breakup length and mixing with air [163, 164]. It has been also emphasized that occurrence of cavitation is highly depended on fuel local vapor pressure [165]. Figure 4.15 is a comparison of vapor pressure of components of PRF29 and heavier Diesel fuels. It can be seen that under engine temperature operating conditions of the injector, there is a high possibility for cavitation in toluene, *n*-heptane, and iso-octane fuels to take place. Taking into account the cavitation phenomenon simulations were again conducted on 70% piston bowl geometry together with 60% and 80% bowls. It should be noted that injector nozzle internal flow simulations were not carried out and in order to represent cavitation phenomenon, experiments of Gannipa et al. and Jia et al. [166, 167] were used to correct breakup length constant and injection axis direction.

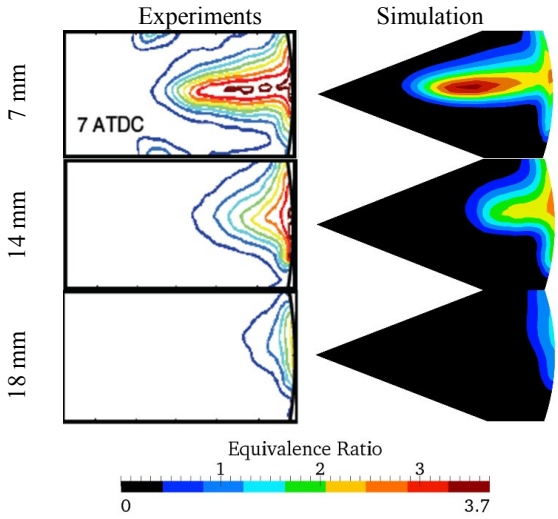

Figure 4.14: *Comparison of equivalence ratio simulation results with experiments of 70% piston bowl geometry.*

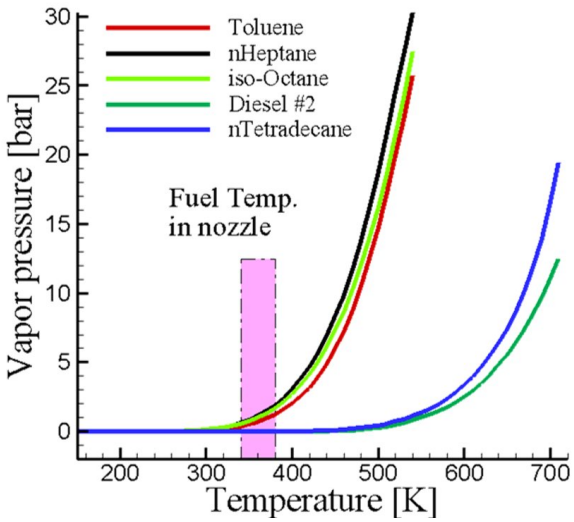

Figure 4.15: *Vapor pressure of selected fuels under injector operating temperatures.*

Breakup length coefficient and spray axis directions of three piston bowl geometries were amended by evaluating the *Reynolds* number based on injection pressure, injector nozzle dimensions, velocity profile and fuel density at the nozzle exit. Results with corrected breakup length coefficient and injection axis directions were represented and validated by the experiments as below. Figure 4.16 shows the comparison between simulation results of equivalence ratio with the experiments of 70% piston bowl geometry for 7, 8, and 12 CAD ATDC. It can be seen that equivalence ratio distributions had a noticeable enhancement by taking the effects of cavitation into account. Comparing to Fig. 4.14, more accurate magnitudes and distributions of equivalence ratio were predicted after including the effects of cavitation.

In order to further validate the new spray simulation setup with included cavitation effect, numerical calculations were conducted on 60% and 80% bowl geometries. Figures 4.17 and 4.18 show that simulations were able to capture acceptable equivalence ratio distributions within the combustion chamber for 60% and 80% piston bowls at three different crank angles. Results show that magnitude of equivalence ratio was noticeably reduced after 2 CAD for the cases which made higher angle with laser sheet planes. For instance, in 60% piston bowl geometry the rich region with equivalence ratio magnitude of 3.7 in middle of sector mesh was reduced to 1.3 during 2

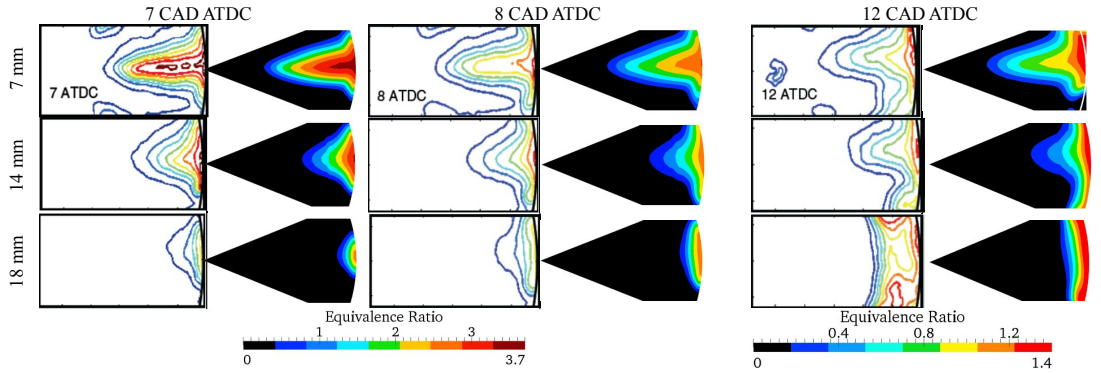

Figure 4.16: *Comparisons of equivalence ratio distribution of three laser sheets of 70% piston bowl geometry at 7, 8, and 12 CAD ATDC by including cavitation effects.*

CAD, whereas the same trend was not observed for 70% bowl case. Moreover, simulations were also captured experimental jet-jet interactions due to applying periodic faces where in 15mm and 20mm laser sheets of 60% piston bowl, it is well predicted by the calculations. Simulation results show that spray targeting and bowl geometry can lead to very different results in case of spray evolution, air-fuel mixing, equivalence ratio distributions and subsequent combustion if the reacting flow experimentation and simulation were conducted.

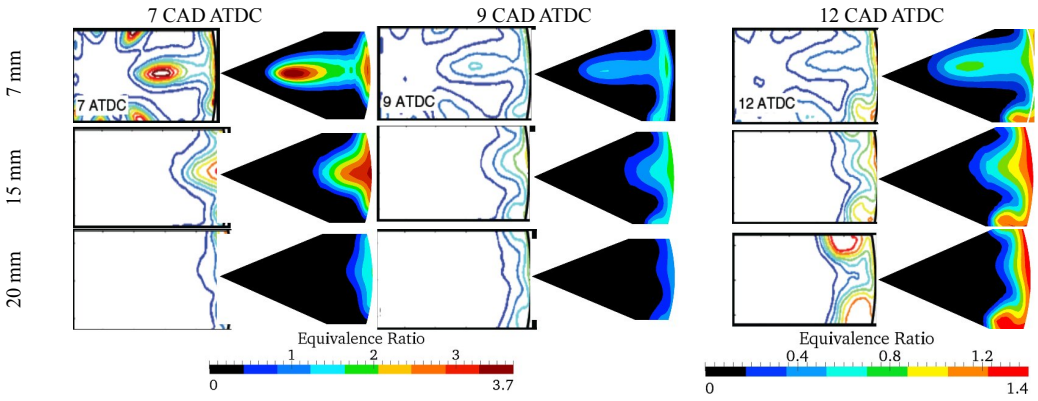

Figure 4.17: *Comparisons of equivalence ratio distribution of three laser sheets of 60% piston bowl geometry at 7, 8, and 12 CAD ATDC by including cavitation effects.*

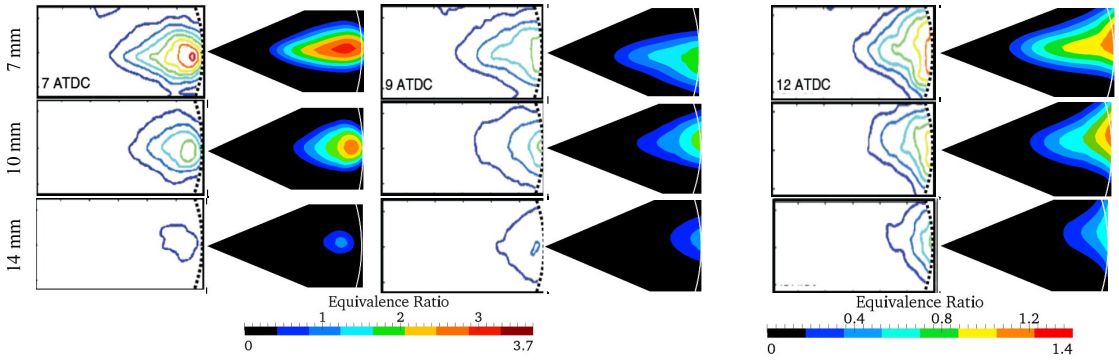

Figure 4.18: *Comparisons of equivalence ratio distribution of three laser sheets of 80% piston bowl geometry at 7, 8, and 12 CAD ATDC by including cavitation effects.*

4.4 Conclusions

In this chapter attention was given to the effects of grid alignments on non-reacting spray simulations and uncertainties caused by cavitation. Some of the main conclusions were made as below:

- By applying conical grid alignment lower numerical diffusion was resulted in vicinity of the injector nozzle where the churning flow takes place and spray morphology was enhanced downstream in evaporated spray region which showed less departure from the actual conical structure in the experiments.
- Higher magnitudes of equivalence ratio were resulted in early crank angles after initiation of injection process in Coarse and Fine Meshes. This was mainly due to high momentum diffusion and spread of Lagrangian particles to the large number of computational cells in Coarse and Fine Meshes, respectively. Similar trend was not observed for Spray Oriented Mesh with lower cell count comparing to the Fine Mesh.
- Application of coarser and non-spray oriented grid alignments resulted on both reticulated evaporated spray simulations and unacceptable early evaporation due to over estimations on momentum diffusion and lowered Lagrangian particle velocities.
- Both Spray Oriented and Conical Meshes showed acceptable results for liquid and

gaseous fuel penetration lengths. However, predictions for spray morphology on radial distances from the injection axis showed acceptable trend only for Conical Mesh alignment of the grids.

- In a study for the effects of cavitation on a non-reacting spray, multi-dimensional simulations were conducted on a low temperature late injection operating condition for an optically accessible DI diesel engine. Three different piston bowl geometries with specific spray targeting were considered. Initial simulation results showed noticeable disagreement with local rich equivalence ratio regions. By determining the Reynolds number at the exit of the nozzle orifice simulations were then conducted by including the cavitation effect by increasing break-up length and shifting the spray axis direction towards cylinder fire deck. Numerical simulations by applying cavitation effects had more accuracy in the magnitudes and distributions of the local equivalence ratio within the combustion chamber. Results show that occurrence of cavitation can tangibly differ air-fuel mixing and equivalence ratio distributions.

CHAPTER 5

Spray A: Study of Reacting Diesel Sprays in Constant Volume Vessel

A fundamental research on reacting Diesel sprays has been extensively conducted for a section of Engine Combustion Network (ECN) named *Spray A* [168]. Non-reacting and reacting conditions were studied by setting up a well-controlled experiments and well-defined boundary conditions to further reduce dependency of the results from facility to facility in the experiments and application of different numerical frameworks and methodologies in simulations. Comparative experimental and numerical studies can be suitable source to discuss the ignition and combustion of the non-premixed Diesel spray combustion under IC engine operating conditions. This can provide useful insights on combustion mechanism and phasing in CI engines and results can further be used for optimization purposes.

5.1 Experimental Apparatus and Configuration

Experimental studies on Spray A configuration were interactively conducted and still continuing mainly in Sandia National Laboratories, Eindhoven University of Technology, IFPEN, and CMT-Motores. Sandia's experimental apparatus briefly discussed here and more information also is available in ECN pages [168].

Spray A is an optically accessible, constant-volume, cubic combustion vessel. Its total volume is $1147 cm^3$. Injector is a very close representative of those used in common-rail, direct-injection Diesel engines and is located at the center of one face of the chamber. Two spark plugs and a mixing fan are mounted for ignition (providing high ambient temperature) and homogenizing the mixture before the spray, respectively. Wide range of ambient conditions for temperature, density, oxidizer ratio, and injection pressure similar to conditions before the injection in CI engines were provided. For sufficiently long injection duration, an established lifted turbulent spray flame is formed. Combustion characteristics of low/high ambient temperatures, pressures, and densities correspond to early/late injection strategies in an engine, respectively, and different levels of EGR are tested using different ambient oxygen concentrations. Measurements are available for several single and multi-component fuels, including both hydrocarbons and oxygenated fuels. Injector is a single-orifice, axial injector nozzle with mini-sac type tip with a top-hat injection profile. Table 5.1 summarizes specifications of the Spray A experimental setup.

5.2 Numerical Simulation

5.2.1 Grid Generation

Taking advantage of symmetry for Sandia's constant volume vessel of Spray A experiments, a 2-dimensional wedge grid is generated. Grid is finer on the injection axis and coarser on the parts of the domain which is not affected by spray varying from the minimum of 0.1mm to the maximum of 1mm. Grid dependancy and applied sub-model for liquid n-dodecane spray can be found in [107].

5.2.2 Initial and Boundary Conditions

Numerical experiment was conducted for the Spray A base-line case as represented in the Table 5.1. Extensive numerical efforts on different operating conditions for ambient

Table 5.1: *Specifications for Spray A base-line operating condition of the ECN [168].*

Ambient gas temperature	900K
Ambient gas pressure	$\approx$ 6.0MPa
Ambient gas density	22.8 kg/m^3
Ambient gas oxygen (Vol)	15% O_2 (reacting); 0% O_2 (non-reacting)
Ambient gas velocity	Near-quiescent, < 1m/s
Fuel injector	Bosch solenoid-activated
Injector nominal nozzle outlet diameter	0.090mm
Nozzle K factor	1.5
Discharge coefficient	C_d = 0.86
Number of holes	1 (single hole)
Orifice orientation	Axial (0° full included angle)
Fuel injection pressure	150MPa (1500 bar)
Fuel	n-dodecane
Fuel temperature at nozzle	363K
Injection duration	1.5ms
Injection mass	3.5 - 3.7mg

temperature, density, oxidizer percentage, and injection pressure can be found in the literature [27, 93, 101, 107, 121, 169–173]. In this chapter, however, numerical results were represented and extensively discussed for only the base-line operating condition to make the connection to the *Spray B* simulations of the Chapter 6.

5.2.3 Non-Reactive Spray Results

For the non-reactive simulation setup, internal field for temperature was set to 900K and pressure to 59.4bar and mass fractions of the initial species as: Y_{O_2}=0, Y_{N_2}=0.884, Y_{H_2O}=0.022, and Y_{CO_2}=0.094. Total injected mass = 3.5mg and injection profile was taken from experimental database of Spray A in ECN web page [168]. Applied sub-models for the spray were similar to Table 4.4 with the modified B_1=24 for Spray A operating condition. Based on ECN recommendations for modeling turbulence in reacting sprays, C_1 constant of $k-\epsilon$ model was set to 1.54. This value was found to better represent effects of turbulent flow on transport of mixture fraction and its variance [168]. Liquid and vapor penetration lengths were extracted from numerical simulations based on the thresholds defined in §4.1 and were compared to ECN Spray A experimental data in Fig.5.1. Moreover, mixture fraction distribution contour for the steady state spray at 0.75ms was compared to the experimental data in Fig.5.2. Non-reacting simulations in terms of liquid and vapor penetration lengths and mixture fraction distribution

were in acceptable agreement with experiments and further reacting simulations can be conducted.

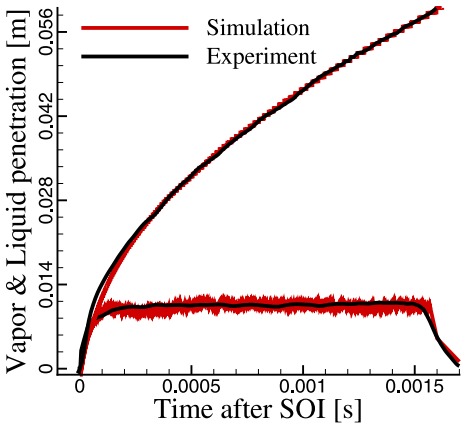

Figure 5.1: *Non-reacting liquid and vapor prnetration length comparison of the spray A baseline case: 0% O_2, 1500bar injection pressure, 900K ambient temperature, and 1.5ms of injection duration.*

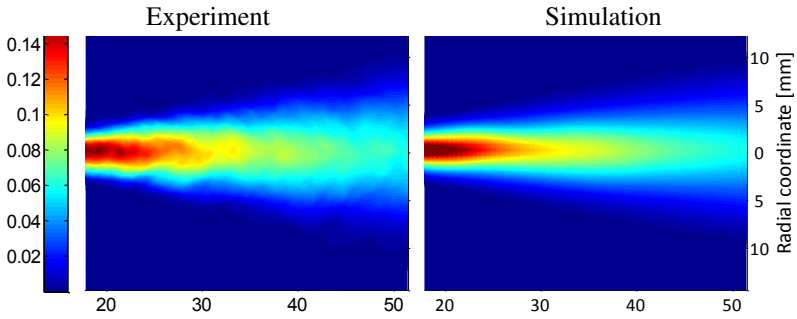

Figure 5.2: *Mixture fraction comparison of the non-reacting spray A baseline case: 0% O_2, 1500bar injection pressure, 900K ambient temperature, and 1.5ms of injection duration experiment with simulation at 0.75ms.*

5.2.4 Reactive Spray Results

Reactive simulation of the spray A experiment was conducted using both MZWM (§3.2.1) and MRIF (§3.2.2) combustion models for the baseline case: 900K ambient temperature, 15%O_2, 22.8Kg/m^3 ambient density, and 1500bar injection pressure. n-dodecane oxidation for both applied combustion models is predicted by using an skeletal chemical mechanism proposed by Lou et al. [173] with 105 chemical species and

420 reactions. In §5.2.6 effects of selection and dependency on chemical kinetics reaction mechanism will be represented.

Literature study on the choice of parameter selection as for identification of the ignition delay and flame lift-off dipickted that researchers have been choosen different parameters and therosholds [93, 101, 107, 121, 169, 170, 172, 173]. Unfortunately, this can be resulted in high level of uncertainity and makes the comparison of the model-to-experiment and model-to-model results of different institutes almost impossible. Refering to the source of ECN Spray A experimental data [168], ignition delay experimentally is determined by two different methods:

1) Pressure Rise based: Ignition delay is the time difference from SOI until high-temperature (rather than first-stage) ignition and combustion (the premixed burn). Pressure threshold must be selected for each condition to ensure that the pressure rise corresponds to the start of high-temperature combustion [174].

2) High-Temperature Chemiluminescence based: Ignition delay is the time difference from SOI until high-temperature (rather than first-stage) ignition and combustion (the premixed burn). Defined as the time when luminosity reaches 50% of steady high-temperature chemiluminescence (not soot luminosity) [175].

Both methods were discussed in detail in [174] and [175] from experimental point of view. It is stated before in §2.12.2 that premixed phase of Diesel spray combustion due to prepared partially homogeneous air-fuel mixture during the ignition delay time, mimics the behavior of rapid heat and pressure rise. It is discussed in [174] that: " The intense pressure rise of the premixed burn creates pressure waves that propagate throughout the combustion vessel. The pressure waves are characterized by large oscillations in measured pressure after the time of the premixed burn. These oscillations are not experimental noise as the noise level of the pressure measurement prior to ignition is much smaller than the oscillation level. The frequency of these oscillations matches the resonant frequency of the combustion vessel. Typically, these pressure oscillations are smoothed in engine experiments by filtering of the signal in post-processing." On the other hand, for the second approach of quantification for ignition delay time, as discussed in detail in [175] the onset of high-temperature heat release in the spray can be characterized by high-speed chemiluminescence imaging to directly measure the location and timing of ignition where care must be taken to avoid the soot luminosity region downstream of the spray.

In numerical modeling and for ignition time quantification, this is author's view that for the sake of consistency and generating comparable results, a global parameter such as pressure rise (or apparent heat release rate in IC engine case) is better to be used. Numerically, OH^* chemistry pathways and its transport in CFD domain can be considered to make comparisons with experimental data, however, using pressure rise which is related to both chemical and physical aspects of reactive fluid flow seems to be a better choice for ignition quantification than chemical specie based thresholds.

Flame lift-off as discussed in [176] was experimentally measured as the distance from injector orifice up to the first axial locations above and below the spray centerline with an intensity greater than approximately 50% of the leveling-off value for OH or OH^* chemiluminescence [168]. Numerically, it is suggested to consider flame lift-off as the first axial location of Favre-average OH mass fraction reaching 5% of its maximum in the domain [168].

Simulation results for ignition delay (as suggested by [168] for pressure rise of high temperature combustion), flame lift-off (based on 5% of maximum OH in the CFD domain) were extracted from the simulation and compared with the experiment data in Table 5.2. Ignition delay is slightly over-predicted in both MZWM and MRIF models. Flame lift-off length is well predicted by MRIF model, whereas for MZWM model it is noticeably over-predicted. This can be due to embeded TCI in the MRIF model and accounting for sub-grid scale turbulent mixing.

Table 5.2: *Spray A baseline case comparison of ignition delay and flame lift-off results of Lou mechanism [173] with ECN experiment [168].*

	Simulation MZWM	Simulation MRIF	Experiment
Ignition delay [ms]	0.46	0.49	0.43
Flame lift-off [mm]	26.2	17.1	16.7

It should also be considered that ignition delay and flame lift-off are the parametrization of two different phases of non-premixed spray flame combustion. This was also discussed in §2.12. Ignition delay is the time delay between start of liquid fuel injection and start of self-sustaining and exothermic chemical reactions (which occur in premixed phase of Diesel spray combustion), whereas flame lift-off happens for fully established diffusive flame during injection of the liquid fuel or little time after end of injection. Nevertheless, to the author's knowledge, definition of the ignition se-

quence and premixed combustion phase was not well-introduced and applied in ECN guidelines. Combustion phasing which is theoretically represented in §2.12, will be discussed next by numerical simulation results.

5.2.5 Combustion Phasing and Flame Structure Analysis

Combustion phasing as discussed in initial Chapters is inseparable part of spray flames and its comprehensive understanding is inevitable for IC engine optimization perspectives. In this section combustion phasing and flame structure for the applied MZWM and MRIF combustion models will be presented. Eliminating dependency of the reactive spray results on chemical kinetics mechanism, only Lou's n-dodecane mechanism [173] was used in this section and effects of chemical mechanism will be discussed in the next section.

Combustion Phasing

The effort now is on linking the conceptual representation of combustion phases of the reacting sprays, Fig.2.11 to the numerical results of the Spray A configuration. PRR result of MZWM model is depicted in Fig.5.3 together with temperature contours in Fig.5.4 to show reaction zone (temperatures higher than 900K of ambient temperature and scaled to the maximum value in each time-step).

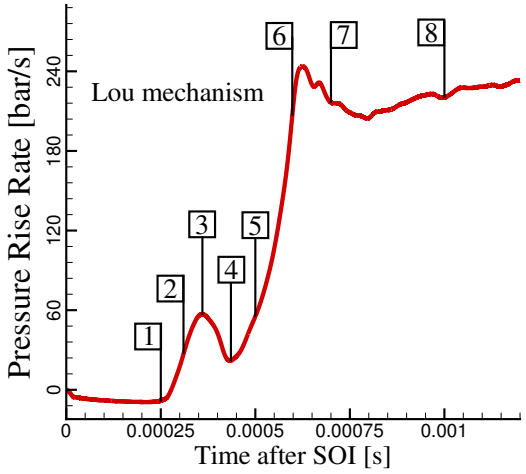

Figure 5.3: *Pressure rise rate of baseline Spray A case for MZWM combustion model using Lou n-dodecane chemical mechanism [173] with marked time-steps.*

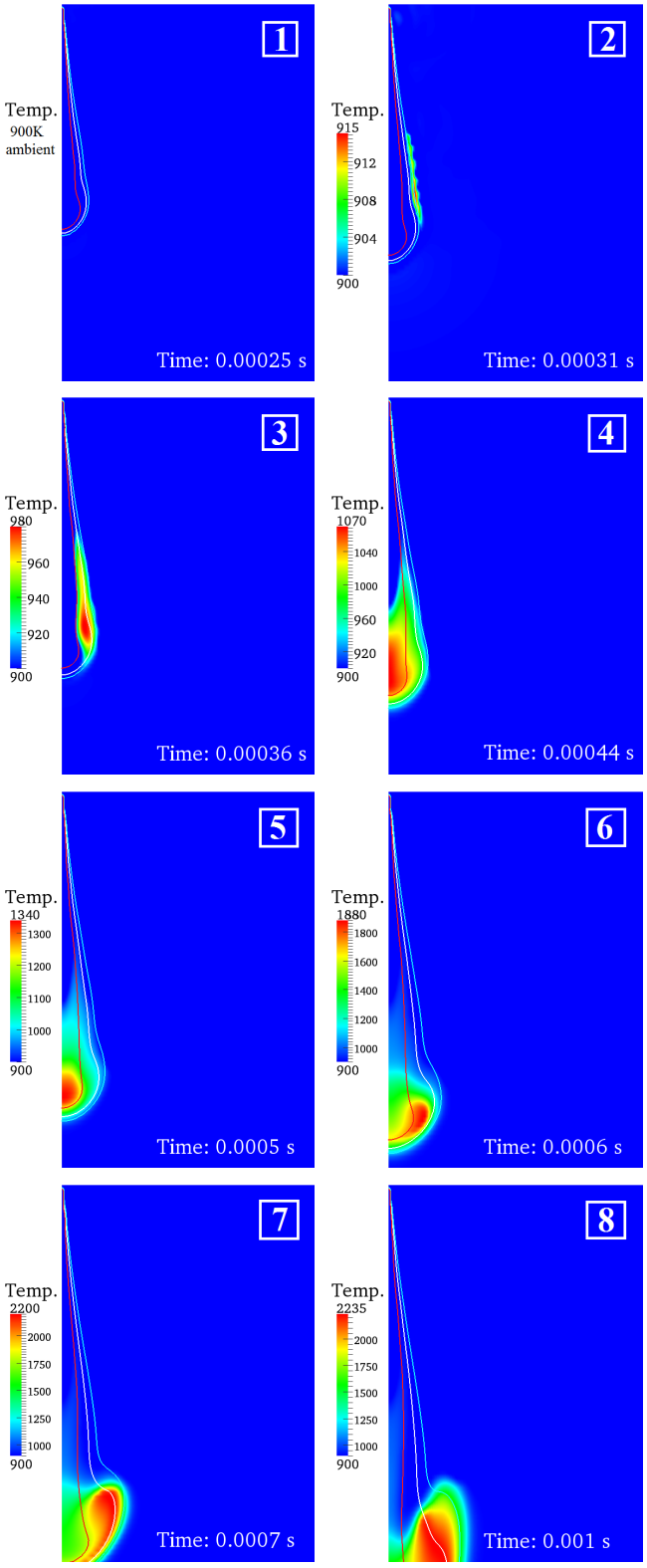

Figure 5.4: *Temperature contours for the marked time-steps in the Fig.5.3 (MZWM model) scaled to minimum of 900K (baseline Spray A ambient temperature) and to the maximum value within each time-steps. White curve:* $Z_{St} = 0.045$*, red curve:* $Z = 2 \times Z_{St}$*, cyan curve:* $Z = 0.5 \times Z_{St}$

All times in both Fig.5.3 and Fig.5.4 are after SOI. Analysis below is based on results of both figures. Marked time steps can be considered to represent: 1: no reactions occur, 2 3, and 4: premixed combustion phase which also coincides with cool flame region of n-dodecane ignition, 5 and 6: transition to diffusive combustion, 7 and 8: diffusive combustion phase (established high temperature diffusive flame). In Fig.5.4 white curve is stoichiometric mixture faction, $Z_{St} = 0.045$, red curve is two times richer than Z_{St} and cyan curve is two times leaner than Z_{St}.

It can be seen that self-sustaining reactions occur in 2 and reaction zone is formed with temperature of 915K in leaner mixture fractions than Z_{St}. This time (0.31ms after SOI) is the first rise of the PRR curve in Fig.5.3. Reaction zone then moves from lean mixtures to stoichiometric and rich mixture fractions in 3 and 4, respectively. Shifting of reaction zone from ignited lean to the rich mixture fractions can also be considered as cool flame region of n-dodecane ignition. However, this is happening for baseline Spray A condition as its ambient temperature is in cool flame region of ignition delay times [173]. After burning the rich mixture fractions (located in spray center line), reaction zone in a transient process moves back from rich mixture fractions to the Z_{St} in times 5 and 6 by significant increase in the temperature. This temperature rise (1340K to 1880K) coincides with noticeable second rise of PRR in Fig.5.3. In times 7 and 8 flame is in almost established diffusive flame conditions as reaction zone with near adiabatic flame temperature is located on Z_{St}. It can be noted that temperature rise from 7 to 8 is not significant. This numerical results agree with conceptual definition of combustion in non/partially premixed conditions by Peters [25].

Comparison of the results for PRR of the applied combustion models, MZWM and MRIF, is shown in Fig.5.5. It can be observed that MRIF model (with TCI) was igniting faster and premixed phase was started earlier than MZWM model. It should be noted that this observation may contradict with already presented results of ignition delay in Table 5.2 where it is represented that MZWM model ignites faster. As discussed before, to be consistent with the definition of ignition delay in ECN guidelines, results of the Table 5.2 for ignition delay is extracted based on second rise (start of high temperature diffusive flame) of PRR in Fig.5.5. This happens earlier in MZWM model.

The reason why in Fig.5.5 MRIF model ignites earlier than NZWM model can be ascribed to the TCI. This is true that TCI through effects of scalar dissipation rate has important role on diffusive phase of non/partially premixed combustion, but at the same

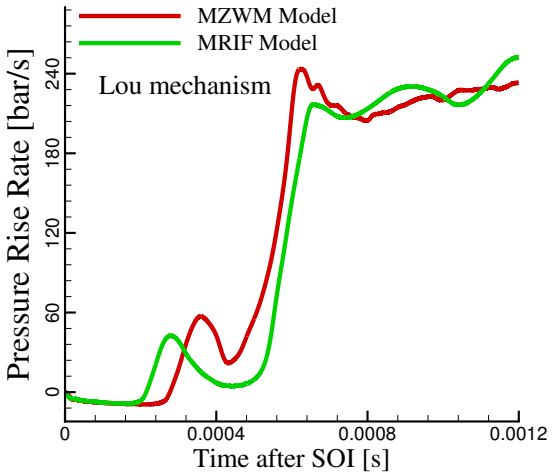

Figure 5.5: *Pressure rise rate of MZWM and MRIF combustion models for the spray A baseline case: 15% O_2, 1500bar injection pressure, 900K ambient temperature, and 1.5ms of injection duration using Lou chemical mechanism [173].*

time sub-grid scale mixing of MRIF model accelerates smoothing of mixture fraction field even before ignition. This can be seen in Fig.5.6 which is the diagram for mixture fraction distribution of the models versus distance from the injector orifice.

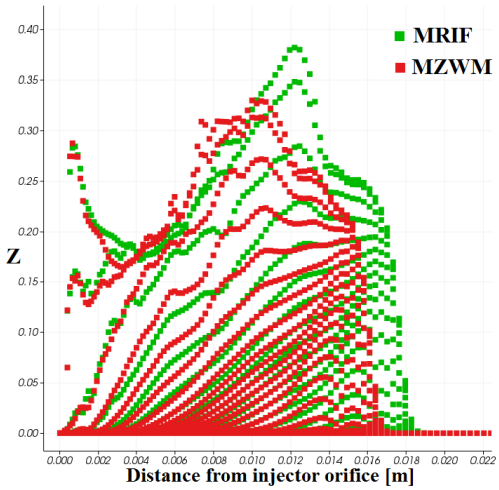

Figure 5.6: *Mixture fraction distribution versus distance from the injecroe orifice for MRIF and MZWM models at time 0.18ms after SOI*

Fig.5.6 represents values of mixture fraction for MZWM model (red squares) and MRIF model (green squares) for the time of 0.18ms which due to PRR diagram of Fig.5.5 for this time there is no pressure rise in both models. It is interesting to note

that, by keeping totally identical injection and spray modeling properties between applied models, mixture fraction spans larger distances for MRIF model than MZWM. Although mixture fraction is a conserved scalar and independent of combustion, its transport can be altered by heat release. This is because heat release causes flow dilatation to occur within the thin mixing layers between fuel and oxidizer [108, 115]. Embedded TCI then causes in lower gradients of mixture fraction in the jet periphery and enhances mixing. Now if any ignitable mixture fraction magnitude is exposed to high temperature ambient gas, local ignition can take place and mixture fraction transport will be altered. This can be correlated to the earlier ignition of MRIF model comparing to MZWM model. More mathematical reasoning of this discussion can be found in in §6.2.4. Such behavior of earlier ignition for the combustion models with TCI comparing to well-mixed models was also observed by other researchers [101, 171].

It can also be seen from the Fig.5.5 that after burning the premixed phase of the combustion, shifting from premixed to the diffusive flame (semi plateau levels of PRR, approximately after 0.64ms) takes longer times for MRIF model. This can be attributed to the nature of well-mixed model as due to the assumption of fully mixed reactants, applied chemical kinetics mechanism rates provide equilibrium thermodynamic state resulting in high reactivity of the ignited mixture fractions. In other words, TCI decelerates return of the reaction zone from rich mixture fractions (latest times in premixed combustion phase, time $\boxed{7}$ in Fig.5.4) to the Z_{St} due to embedded sub-grid scale mixing effects. Model-to-model comparisons and reasoning will be more discussed in detail for larger number of operating conditions for *Spray B* configuration in §6.2.4.

Transient Flame Structure

Flame structure analysis by using graphs of temperature versus mixture fraction, can provide useful sort of information for the different times (starting from $\boxed{2}$) of transient flame evolution and model-to-model comparisons. Fig. 5.7 shows both flame structure and OH contours of the applied combustion models in the corresponding time. For the times of $\boxed{7}$ and $\boxed{8}$ (established diffusive flame discussed in the Fig.5.5) cyan curves are also shown for the 5% of maximum OH as diffusive flame indicator on the white curves of Z_{St}.

It can be seen that for $\boxed{2}$, MRIF model has already started the premixed phase combustion and higher temperatures (reaction zone) is shifting toward richer mixture

fractions reaching to 50K higher than ambient temperature, whereas premixed phase of MZWM model is just started from leaner mixture fractions. Alongside these observations, OH contours show the correlated behavior. At time $\boxed{2}$ there is a high amount of OH mass fractions in the fuel rich tip of the spray for the MRIF model, however, higher magnitudes of OH are started to appear from leaner mixture fractions (not from Z_{St}). After this time MZWM model has noticeably higher shifting speed to the diffusive combustion phase where at times $\boxed{7}$ and $\boxed{8}$ fully established diffusive flame is formed. This can be related to the assumption of this model which ignited mixture fractions which experience local thermodynamic equilibrium. For all the flame structure diagrams in the Fig. 5.7, MRIF model resulted in more scattered *Z-Temperature* distributions between mixing line and thermodynamic equilibrium lines. This is due to embedded mixing effect of this model which predicts intermediate thermodynamic conditions rather than equilibrium. Reaction zone in both models moves to richer mixture fractions (approximately *Z*=0.175) and returns to Z_{St} on times $\boxed{7}$ and $\boxed{8}$. It also burns with higher rates (generating higher peak temperatures) for MZWM than MRIF model. For model-to-model comparison, attention is given to the times $\boxed{7}$ and $\boxed{8}$ in case of OH contours and limits of the diffusive flame. It can be seen that magnitudes of the OH mass fractions are higher for MZWM model in all represented times. This again can be attributed to the well-mixed model assumption and included mixing effects in MRIF model. On the other hand, MRIF model shows more reactive flame brush which can be seen in the times $\boxed{7}$ and $\boxed{8}$ for the cyan curves for the flame lift-off threshold. This is because mixing-effects through scalar dissipation rate generate smaller gradients of mixture fraction variance and smooth down the mixture fraction field more than MZWM model. Fig.5.8 shows OH mass fraction versus scalar dissipation rate below the flame extinction scalar dissipation rates for MZWM and MRIF models at 1ms after SOI. It can be noted that larger number of scalar dissipation rates have OH mass fractions more than zero (χ<30 as ignited mixture fractions) for the MRIF model, whereas MZWM model spans narrower ignited scalar dissipation rates (χ<5) but with higher magnitudes of OH mass fractions. This is why lift-off length is shorter in MRIF model for the represented results in the Fig.5.7.

Time: 2 0.31ms after SOI

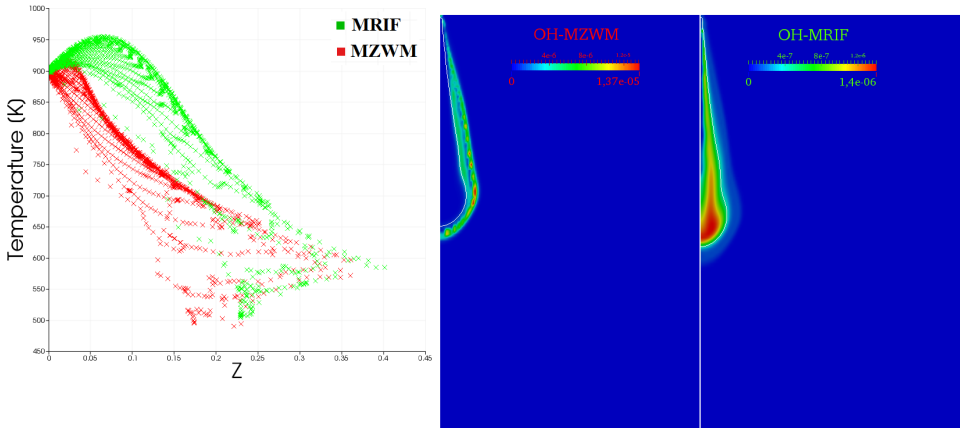

Time: 3 0.36ms after SOI

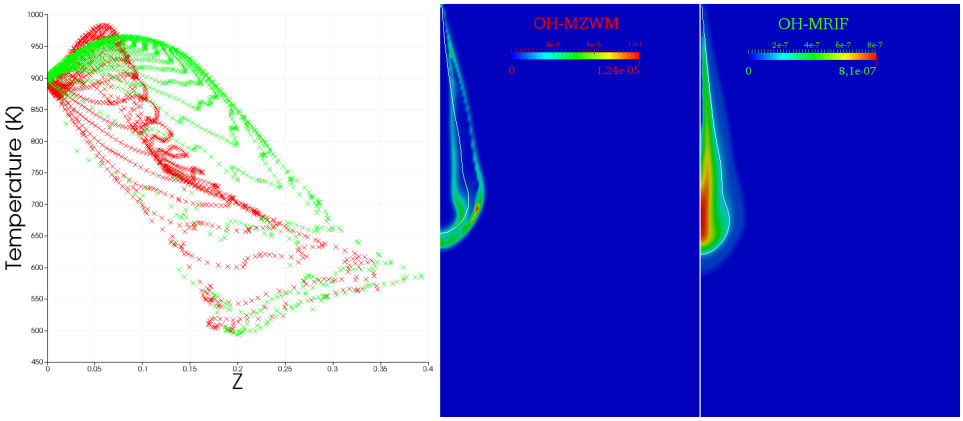

Time: 4 0.44ms after SOI

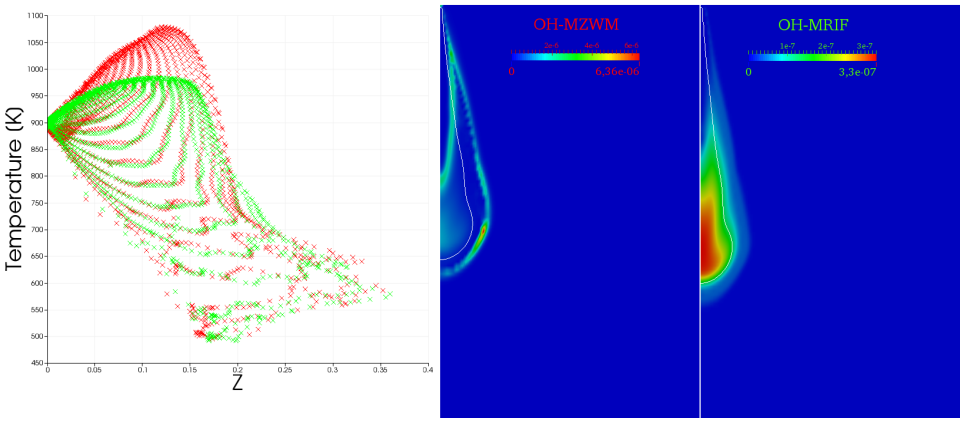

Time: 5 0.50ms after SOI

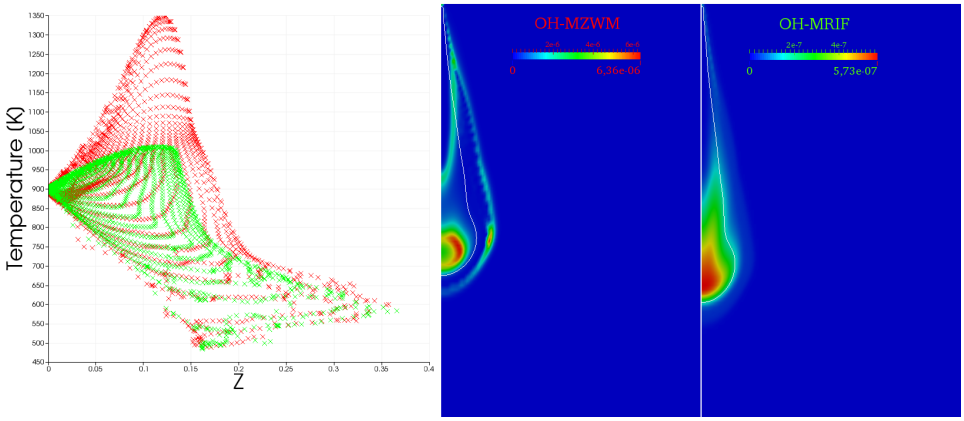

Time: 6 0.60ms after SOI

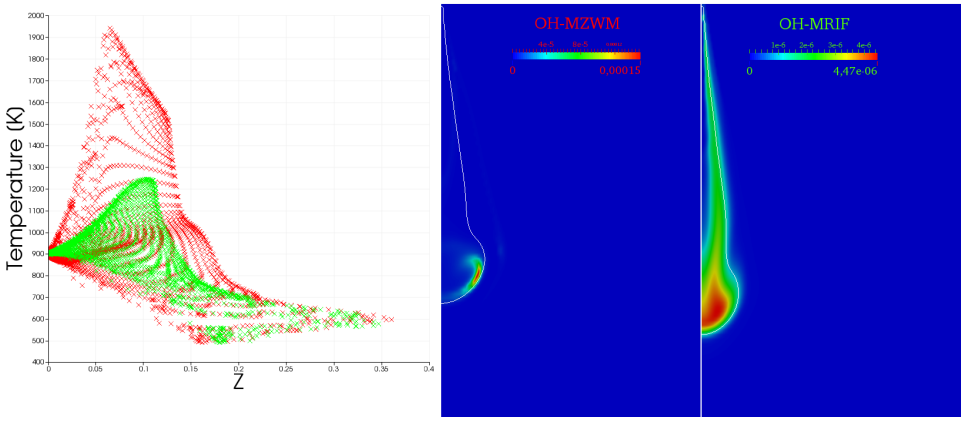

Time: 7 0.70ms after SOI

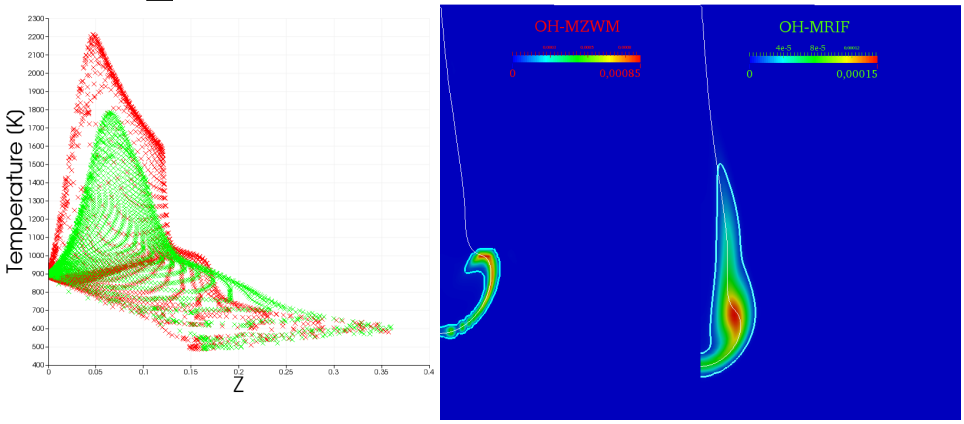

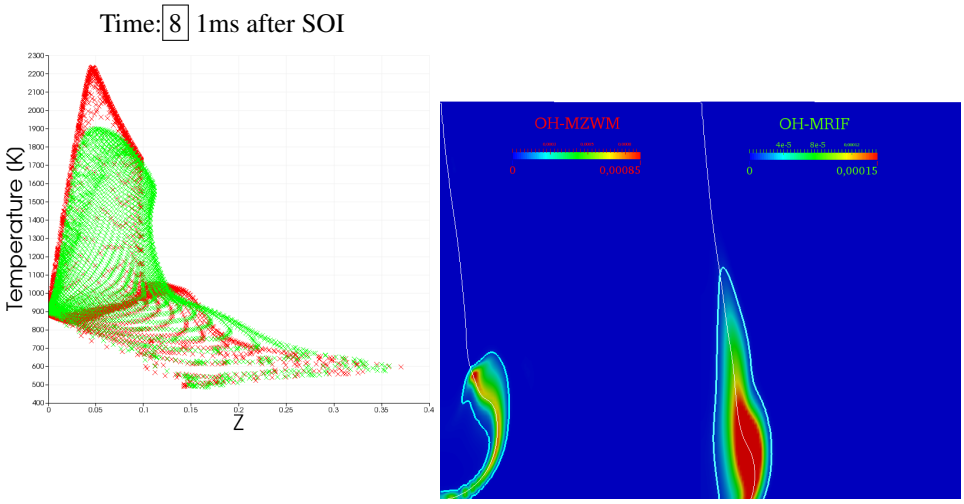

Figure 5.7: *Flame structure, Z-Temperature diagrams, based on times in Fig.5.3 for the applied combustion models. White curve: $Z_{St} = 0.045$, cyan curve: 5% of maximum OH as diffusive flame indicator.*

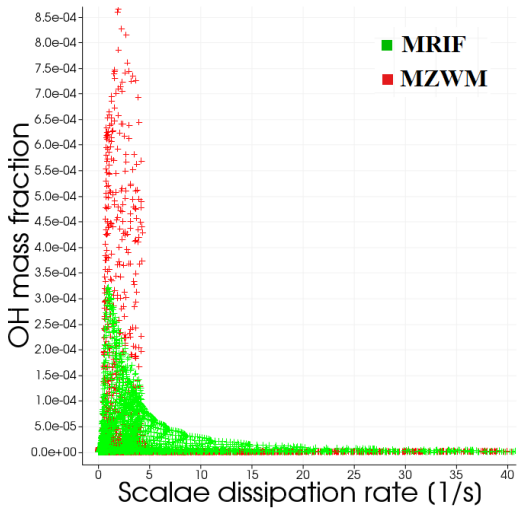

Figure 5.8: *OH mass fraction versus scalar dissipation rate for MZWM and MRIF model at the time of fully established diffusive flame (1ms after SOI).*

5.2.6 Effect of Chemical Kinetics Mechanism

Attention is then given to the effect of choice of n-dodecane chemical kinetics mechanism only using the MRIF combustion model. Lou's mechanism [173] result for PRR is compared to Yao [177] and PoliMi [178] mechanisms. It can be seen that Yao and

PoliMi mechanisms ignite earlier than Lou mechanism, however, magnitudes of PRR for the premixed combustion phase is different for all mechanisms. Shifting to diffusive combustion phase (second rise of PRR diagram) is happening earlier for Yao mechanism and then for PoliMi and Lou mechanisms, respectively.

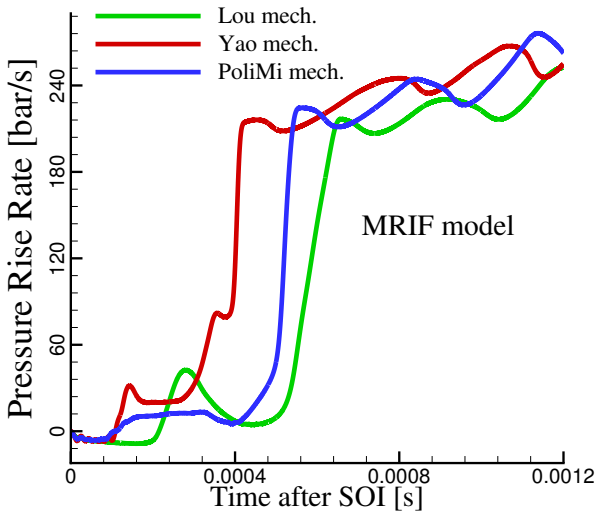

Figure 5.9: *PRR results of MRIF model for Lou [173], Yao [177], and PoliMi [178] mechanisms.*

For the flame structure, differences between mechanisms can be found in the Z-temperature diagrams of Fig.5.10 and spatial representation of diffusive flame limits in the Fig.5.11. It can be seen that for the time of 1ms after SOI (already established diffusive flame), Lou and PoliMi mechanisms predict pretty similar flame structure. Yao mechanism is more reactive in richer mixture fractions (Z>0.1). Another observation is that maximum temperature for Lou mechanism, 1900K, is lower than peak temperature of 2100K for the both Yao and PoliMi mechanisms. Effects of these observations can be seen in the Fig.5.11. Flame brush of the Yao mechanism (red curve) is noticeably wider than Lou (green curve) and PoliMi (blue curve) mechanisms. As explained this behavior is because of higher reactivity of this mechanism. It can be also seen that Yao and PoliMi mechanisms predict very similar flame lift-off length. This can be ascribed to Z-temperature diagrams of these mechanisms and having very similar peak temperature in vicinity of Z_{St}.

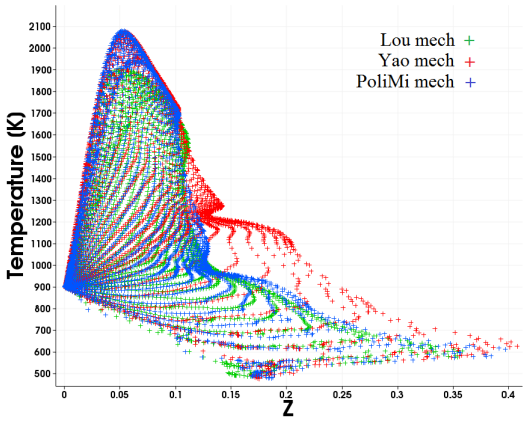

Figure 5.10: *Flame structure results of MRIF model for Lou [173], Yao [177], and PoliMi [178] n-dodecane mechanisms at time 1ms after SOI.*

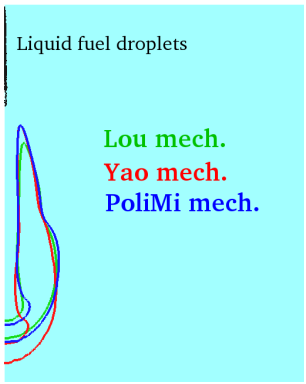

Figure 5.11: *Diffusive flame limit for the applied chemistry mechanisms marked by 5% of maximum OH for the established diffusive flame at 1ms after SOI.*

5.3 Conclusions

Non-reacting and reacting baseline n-dodecane experiment of ECN, so-called *Spray A*, was numerically investigated in this chapter. It was discussed that Spray A configuration can provide useful insights on combustion characteristics of CI Diesel engines. The most important advantage of ECN Spray A experiments is in their quality of data and careful control on boundary conditions. The latter advantage highly enhances numerical model selection and accuracy of the simulation results. Initially, non-reacting simulation was performed to ensure reliable predictions on liquid and vapor penetration lengths.

After achieving to reliable non-reacting results, reacting simulations were performed using well-mixed chemistry and flamelet based combustion models. Main attention in

this chapter was given to the combustion phasing analysis of the liquid spray flames and mechanism of diffusive flame establishment. It was tried to make clear connection between conceptual representation of Diesel engine combustion phases with numerical results. It is concluded a global parameter such as apparent heat release rate or pressure rise rate can better depict Diesel combustion phases and combustion characteristics such as ignition sequence. Pressure rise rate results were used to identify ignition time and comparisons were made between models with and without embedded TCI. It has been found that including TCI will alter the transport of mixture fraction although it is a conserved scalar. This occurs due to enhanced turbulent mixing through applying TCI and later flow dilatation and was resulted in earlier ignition of the flamelet combustion model.

In case of combustion phasing and moving of the reaction zone within mixture fraction space, it has been shown that in both models reaction zone starts from lean mixtures (for spray A baseline condition) and moves to richer mixture fractions and later stabilizes on stoichiometric mixture fraction. However, this movement was seen to be faster for well-mixed model. It also concluded that although TCI will promote the local condition to trigger the main ignition, it will limit the reaction rate in the transition of the main ignition to the diffusive combustion phase. It is also found that combustion phasing is highly depended on the applied chemical kinetics mechanism. By eliminating the dependency on the combustion model, it was illustrated that the results of the different chemical kinetics mechanisms can be noticeably different for predictions of ignition, combustion phasing, and flame lift-off length.

In case of flame structure, tangible differences was depicted for the applied combustion models. It was shown that TCI reduces the maximum temperature of the ignited mixture fractions while well-mixed model assumes majority of the ignited mixture fractions in thermodynamic equilibrium. Flame structure was also affected by the choice of chemical kinetics mechanism selection where reaction zone and diffusive flame brush can be altered by applying different mechanisms.

CHAPTER 6

Spray B in Engines: Study of Reactive Diesel Sprays within Real Engine Operating Conditions

Driven by the need to reduce pollutant emissions (NO_x and soot) while simultaneously maintaining high efficiencies, detailed experimental results and accurate numerical methods are of great importance for the development of the next generation of Diesel engines. In particular, the combustion process is influenced by the complex interplay of spray evolution, in-cylinder flow, turbulence and chemical kinetics. Reproducible test results are required to compare different techniques enable a better understanding of the involved interacting physical phenomena. Within this context, attention has mainly focused on the so-called *Spray A* configuration of ECN, where n-dodecane fuel is delivered by an axial, single hole nozzle in a constant volume chamber at ambient conditions (reacting and non-reacting) similar to those encountered in Diesel engines at start of injection [171, 173, 179, 180]. The experimental database includes conditions at variable ambient temperature (450-1300K), density (7-30kg/m^3), injection pressure (50-150 MPa) and Oxygen concentration (0-21%) [181, 182].

Comparison to experiments typically includes global fuel-air mixing and combustion indicators (penetration, ignition delay time, flame lift-off length), but also correlating computed distributions of chemical species (formaldehyde, OH, soot, PAH) with the ones measured with detailed optical techniques. The availability of detailed experimental data and the possibility to compare simulation results achieved with different numerical approaches, make it possible to identify which are the most suitable. However, both fuel-air mixing and combustion processes are affected by in-cylinder flow (swirl, squish and jet-wall interaction) and heat transfer. For this reason, the quality of the CFD simulation results needs to be evaluated to experiments in engines. This Chapter extends prior art in the ECN by comparing experiments and simulations in not just engine-relevant conditions in a constant volume vessel, but actually in engines. With a proper choice of intake temperature and pressure, it is possible to achieve thermodynamic conditions at start of injections (SOI) similar to those encountered in the constant-volume vessel. To date, numerous simulations of the *Spray A* experiment have been carried out to evaluate different approaches to model combustion, fuel-air mixing, and mesh management. This includes the comparisons of fixed grids with adaptive local mesh refinement [172, 183], accounting for turbulence-chemistry interaction versus assuming every cell to be a homogeneous reactor [107, 171, 173]. Among these, the spray is generally modeled with the Lagrangian approach, none-the-less the capabilities of Eulerian-Eulerian appears to be very promising [184] when applied at simulation of non-reacting conditions. Similar to Chapter 5, MZWM and MRIF combustion models are considered. Using the same engine studied in this Chapter, Singh et al. [155] applied well-mixed and their flamelet based combustion model for *Diesel Type 2* fuel with different injector and injection amount under variety of engine operating modes. However, no comparisons were made with experiments on liquid and vapor penetrations and no quantitative numerical ignition delay and flame lift-off studies were carried out. Although Singh et al. [155] considered five different combustion modes (differences were considered based on high/low temperature, long/short ignition delay, and early/late injection criteria), the initial and boundary conditions of these modes were not consistent and no comparative studies can be made.

6.0.1 Specific Aims

Aim here is to assess two combustion methodologies and identify the most suitable approach over a wide operating map in the real engine operating conditions. Parametric variation and comparison to the experiment is carried out at different operating conditions including variation of ambient temperature of 800, 900 and 1000K, ambient density of 15.2 and 22.8 kg/m^3, oxygen concentrations of 13, 15 and 21%, and injection pressure of 500, 1000 and 1500 bar. Initial and boundary conditions of these operating points are well controlled, enabling comparative study between them on non-reacting and reacting characteristics of Diesel engine spray and combustion.

6.1 Experimental Apparatus and Configuration

6.1.1 Optical Engine and Diagnostic Setup

The engine used for the experiments is a Sandia single cylinder 2.34L optical heavy-duty Diesel, based on the Cummins N-series production line. The optical engine is designed so that the upper cylinder liner separates and drops down from the head without engine dis-assembly, for cleaning of in-cylinder optical surfaces[1]. Selected details of the geometry for the engine appears in Table 6.1. The injector of interest is the ECN Spray B #211199, a three hole injector. Details of the injector appear in Table 6.2. In Fig 6.1, a schematic of the extended piston showing the optical path for the blue LED illumination[2] and a monochrome Phantom v7.1 in a schlieren configuration for the detection of vapor penetration. Two other optical setups, not shown in Fig 6.1, are also used. The second included a Phantom v611 high-speed color camera for liquid length computed from images of Mie-scattering of liquid under non-reacting (7.5%O_2 by volume) conditions. The third optical setup includes a beam splitter (R310 diachroic @45^o) and a second intensified monochrome Phantom 7.1 fitted with a bandpass filter of width 10nm centered at 310nm for simultaneous intensified OH^* chemiluminescence and broadband luminosity ignition detection. These images are used to determine ignition delay and lift-off length. Operating conditions and their parametric variations are detailed next. Additional details of the operating conditions, boundary condition monitoring, and imaging diagnostic setups for ignition delay, vapor penetration, liquid

[1] Experiments were conducted in Sandia National Labs. For more information regarding the experiments refer to [185]

[2] 1.5mm^2 Cree XPE LED in a custom assembly built at Sandia National Labs.

and lift-off length are discussed in [185] and so are only briefly described below.

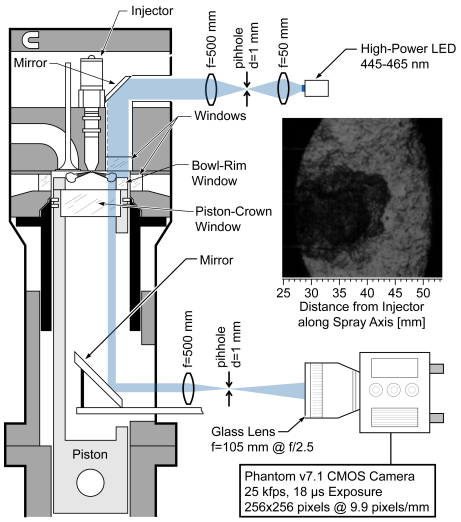

Figure 6.1: *Extended-piston optical imaging schematic with the schlieren setup. Inset: Example instantaneous schlieren image at 364 CAD at ambient-gas conditions of 900K, 15.2kg/m^3 and 7.5%O_2, with 1500 bar rail pressure.*

Table 6.1: *Sandia optical engine specifications [186]*

Intake valves	2
Exhaust valves	1
Swirl ratio	0.5
Bore × Stroke	13.97 × 15.24 [cm]
Bowl width × depth	9.78 × 1.55 [cm]
Displacement	2.34 [L]
Compression ratio	11.22:1
Connecting rod length	30.48 [cm]

6.1.2 Operating Conditions

A number of parametric variations are performed with Spray B in the optical engine. Injection configurations such as timing, duration and profile were kept identical, but injector rail pressure and ambient gas properties are changed. At each condition, a minimum of 30 but up to 90 injections are performed and the resulting parameters computed represent ensemble averages. Details of the experimental cases are listed in Table 6.3. *Cases* are named based on the targeted TDC condition. A numeric case ID is

Table 6.2: *Sandia Spray B injector specifications. Orifice #3 was the orifice of interest in Spray B experiments. Bottom: Schematic orientation of the orifices for Spray B [15]*

Inj. type	#211199 Bosch Spray B
Hole sizes, #1, 2, 3	90.9μm, 91.7μm, 90.9μm
Nominal included angle	145^o
Nozzle shaping	Smoothed
Discharge coefficient	C_d= 0.86
Hole angular position	#1 36.4°, #2 -62.3°, #3 180°

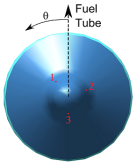

also included and used for reference in the result section of this chapter. *SprayB* is the baseline case; 900K, 15%O_2, 22.8kg/m^3 in-cylinder conditions, with an injection at 1500bar rail pressure. *800K* and *1000K* are the targeted 800K and 1000K temperatures at TDC, and can be achieved by variable intake charge heating. The *15.2* lower density case is experimentally achieved by reducing the intake plenum mass-flow (and hence pressure). *13%* and *21%* are the variations on oxygen percentage by volume in the cylinder air composition produced by variable dilution of the intake charge with Nitrogen. Finally, *500b* and *1000b* are the cases for 500 and 1000 bar injector rail pressure, controlled by the pressure set-point of the high-pressure fuel pump.

6.1.3 Liquid Length

The ECN recommended technique to measure liquid length is the Diffused Back Illumination (DBI) setup [187]. This technique has been selected among others [188] because it is self-calibrated and therefore enables comparison between different facilities without introducing differences based on threshold issues. However, the configuration of the heavy-duty optical engine used in the experiments is not suited for the implementation of this DBI setup. Therefore, the more classical Mie scattering setup alluded to above is used. The intensity profiles along the axis of the 3 sprays are collected, and the threshold is defined as 3% of the maximum value, similar to what is described in [189]. The distance measured on the image is then converted into a distance along the spray axes, since the image collected on the sensor only gives *projected* distances. The im-

Table 6.3: *Experimental initial conditions and properties of Spray B engine tests*

Case name	**SprayB**	**800K**	**1000K**	**15.2**	**13%**	**21%**	**500b**	**1000b**
Case ID	1	2	3	4	5	6	7	8
Temperature @ IVC [K]	380	340	454	400	392	396	397	390
Pressure @ IVC [bar]	2.25	2.01	2.61	1.54	2.27	2.26	2.28	2.28
Temperature @ TDC [K]	900	800	1000	900	900	900	900	900
Density @ TDC [kg/m^3]	22.8	22.8	22.8	15.2	22.8	22.8	22.8	22.8
Non-reacting O_2 [%]				7.5	7.5	7.5	7.5	7.5
Reacting O_2 [%]	15	15	15	15	13	21	15	15
Injection pressure [bar]	1500	1500	1500	1500	1500	1500	500	1000
Injected mass [mg/cycle]	3.68	3.68	3.68	3.68	3.68	3.68	2.06	2.98
Engine Speed [rpm]	1200	1200	1200	1200	1200	1200	1200	1200
Inj. start [CAD ATDC]	-2.5	-2.5	-2.5	-2.5	-2.5	-2.5	-2.5	-2.5
Inj. duration [CAD]	11	11	11	11	11	11	11	11

ages are acquired at 67.1kHz onto the red channel of a Phantom v611 complimentary metal oxide semiconductor (CMOS) camera. The field of view is 40×40 mm^2 at an image size of 128×128 pixels^2 (2.8 pixels/mm).

6.1.4 Vapor Penetration

Schlieren images are acquired of one penetrating Diesel jet passing between the cylinder head and piston window to determine vapor penetration under non-reacting conditions. A collimated beam is directed through the engine's upper viewport shown in Fig 6.1. A monochrome Phantom v7.1 CMOS camera is set to a frame rate of 25kHz and an exposure duration of 40μs (though the effective exposure duration is set by the LED pulse duration of 5μs), corresponding to 1 image each 0.29 CAD at 1200 revolutions per minute (RPM). The average penetration data compared in the results are computed from an ensemble average of thirty injections. The field of view is 26×26mm^2 at an image size of 256×256 pixels^2 (9.9 pixels/mm).

Because the optical access only permits the visualization of the spray between about 26mm and 50mm from the nozzle orifice, the processing proposed in [190] cannot be applied. Instead, the vapor penetration is defined as the furthest point of the spray border to the orifice. An example of a processed schlieren image is presented in Fig. 6.2. The blue line is the border of the spray. The red circle represents the point of the border

with the maximum distance to the orifice. Because the injector orifice is angled with respect to the projected image plane, the vapor penetration reported in the results has been adjusted (lengthened) to compensate. This compensation was computed assuming that the spray penetration maximum follows a 17.5^o down angle specified for Spray B.

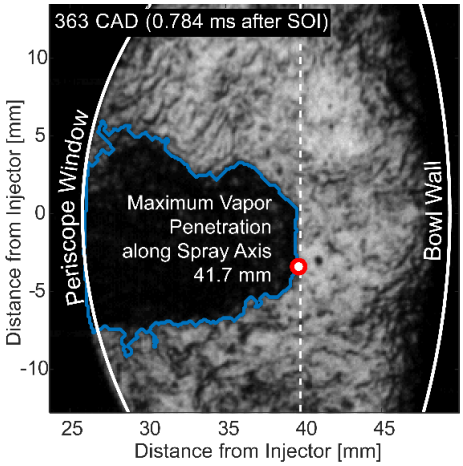

Figure 6.2: *Example of a processed schlieren image, for an ambient density of* $15.2kg/m^3$ *in non-reacting conditions. The blue line defines the frontier on the spray. The red circle is the position of the maximum vapor penetration.*

6.1.5 Start of Combustion, Heat Release Rate

Cylinder pressure is digitized and recorded at 1/4 degrees crank-angle (CAD) resolution, simultaneously with the acquisition of the optical data. The apparent heat release rate (AHRR) is calculated from filtered pressure data using an air-standard first-law analysis (e.g. Heywood [191]). The pressure data are smoothed using a Fourier series low-pass filter with a Gaussian roll-off function having a transmission of 100% from 0 to 800Hz and dropping to 1% at 3360Hz. These cut-off frequencies were selected to remove acoustic ringing in the cylinder pressure data, while retaining the general features of the AHRR. Using these filter parameters, the apparent start of combustion (SOC), indicated by the first zero-crossing of AHRR, is typically advanced from that for the unfiltered data up to 70μs, depending on the AHRR magnitude occurring during the premixed portion following SOC. Additionally, the peak of the premixed burn spike in the filtered AHRR is reduced by about a factor of 2, while its width is increased by a factor of 2. The apparent energy released during the premixed burn (area under the AHRR curve), however, is virtually unchanged by this filtering technique.

6.1.6 Length of Flame Lift-off

The OH^* chemiluminescence images are processed following the methodology proposed in [176, 192]. The axis of each spray is defined manually, and on each side of the spray centerline two lines are arbitrary selected, forming an angle of $\pm 5^o$ with the spray axis. The lift-off is determined along those 2 lines and averaged. An example of a processed image is presented in Fig. 6.3. Images are acquired at 7.2kHz with a monochrome Phantom v7.1 CMOS camera. The field of view is 60×60 mm^2 at an image size of 512×512 pixels^2 (8.5 pixels/mm).

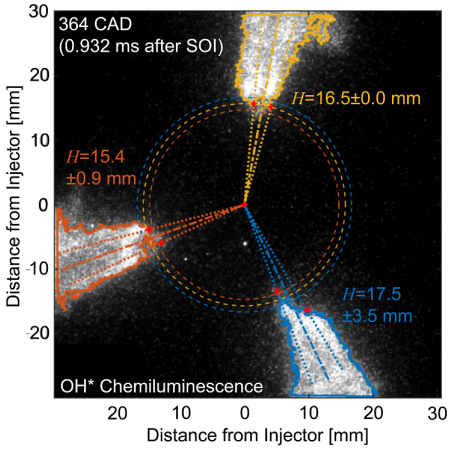

Figure 6.3: *Example of a processed OH^* chemiluminescence image, for an ambient density of 22.8kg/m^3, 15%O_2 and ambient temperature 1000K, 0.932ms after SOI.*

6.2 Numerical Simulation

6.2.1 Engine Mesh Generation

An automatic mesh generation tool has been developed and incorporated into the Lib-ICE code, which is based on the OpenFOAM® technology to create spray/flow-oriented and fully hexahedral grids [193]. On the basis of combustion chamber details and/or user specified parameters such as piston bowl points, injector direction, squish height, and valve lift diagram; body fitted grids are automatically generated to perform full-cycle or compression/combustion simulations. Spray-oriented grid assures less numerical diffusion during the liquid fuel spray calculations if LDEF (Lagrangian Droplet and Eulerian Flow) method is applied [44]. Due to the configuration of applied injector in Spray B experiments, spray-oriented grid generation is performed for one-third of

the Sandia optical engine. Grid details include 45,916 and 341,562 cells at TDC and BDC and with 48.7 and 11.2 for maximum and average mesh non-orthogonality. The average cell size is less than 1 mm and tests were previously performed to verify grid-independent results [44]. Figure 6.4 shows the generated spray-oriented grid for Sandia optical engine and Spray B simulations at TDC.

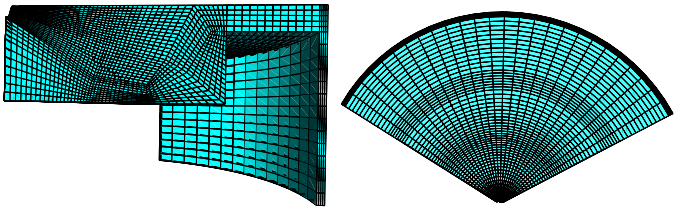

Figure 6.4: *Spray-oriented grid automatically generated for Sandia optical engine Spray B experiments.*

6.2.2 Initial and Boundary Conditions

Wall boundary layer treatment for heat transfer calculations is modeled by the Huh-Chang wall function [194]. Spray sub-models employed in this work are the same as in [44]: jet and droplet breakup were computed by the KHRT model, which accounts for both Kelvin-Helmholtz (KH) and Rayleigh-Taylor (RT) instabilities [158]. Concerning other sub-models used, droplet evaporation is computed on the basis of the D^2 law and the Spalding mass number while the Ranz-Marshall correlation was used to model heat transfer between liquid and gas phases.

6.2.3 Non-Reactive Engine Results and Experimental Validation

Experiments and numerical simulation results for the liquid and vapor penetration length of the Spray B cases are depicted in Fig.6.5 using the threshold considered in §4.1. Among the 8 cases, only the 1000K temperature liquid length falls outside one standard deviation from the mean liquid length. Although within the measurement standard deviation, liquid penetration is systematically over-predicted, except at the highest oxygen concentration. Vapor penetration mainly depends on the exchange of mass and momentum between liquid and gas phase and is enhanced slightly by turbulent diffusivity. Fig. 6.6 also compares spatial fuel vapor distribution and penetration

values of the 0.001 mixture fraction contour in the numerical simulations compared to the experimental schlieren images at 1.5, 2.5, 3.5, and 4.5 CAD ATDC. These engine crank angles are also marked as A, B, C, and D in the Fig. 6.5. From both Fig. 6.6 and Fig. 6.5 it can be seen that numerical simulations are capable or comparable predictions of vapor penetration and evaporated spray morphology comparing to the experiments.

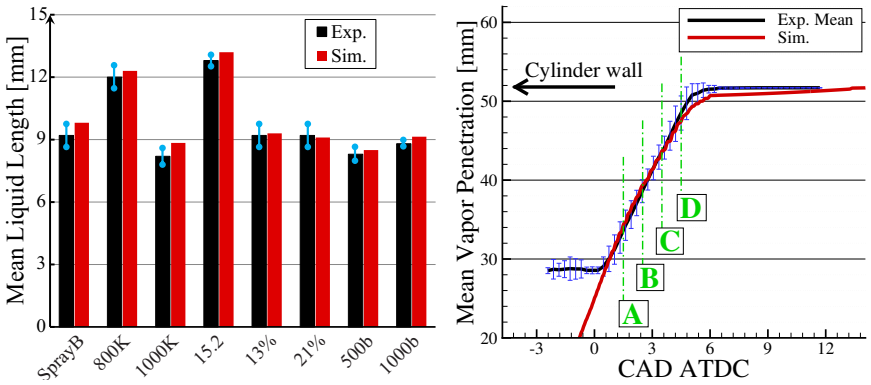

Figure 6.5: *Mean liquid and vapor penetration length comparisons of the cases for simulations and experiments in Sandia optical engine.*

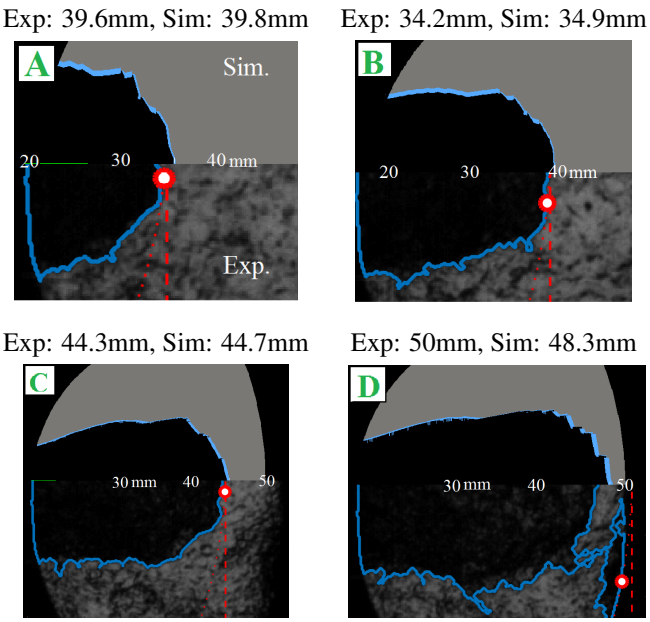

Figure 6.6: *Spatial distribution of fuel vapor of the Case 4 compared to experimental schlieren images for the times in Fig.6.5 .*

6.2.4 Reactive Engine Results, Model-to-Model and Model-to-Experiments Comparisons

n-dodecane oxidation is predicted in this work for both flamelet and well-mixed models by using the reduced chemical mechanism proposed by Yao et al. [177] which considers 54 chemical species. The very limited number of species and its capability to properly reproduce ignition delay and flame lift-off data at constant volume conditions makes it very suitable for combustion simulations in CI engines. Cases represented in Table 6.3 are grouped in subsections to separately show how the combustion process is affected by ambient temperature, ambient density, oxygen concentration and injection pressure. Thresholds below are used for definition of ignition delay time and flame lift-off calculations;

- **Ignition Delay:** Similar to the experiments, AHRR results of simulations are calculated using thermodynamic first-law analysis. The same approach used for the experimental filtering of the AHRR is applied on numerical results with adjusted frequencies due to lower CFD time-steps than experimental data intervals. Similar to the experiments, engine crank angle for the rise of AHRR form zero value is considered as ignition time and time from SOI to ignition is considered as ignition delay. This has to be mentioned that there is a need to define a unique parameter/method to calculate ignition delay from simulations. As an instance, maximum rate of rise of Favre-averaged temperature in [171] and rise of 400K in a CFD cell from initial temperature in [101] were used to quantify ignition delay. Both of these methods were used in the present work, however, significantly different ignition delay times were resulted. As it is mentioned, rise of AHRR form zero value is considered as ignition time in this study.

- **Length of Flame Lift-off:** In this study, flame lift-off is based on 14% of maximum OH radical as suggested in [195] for the applied chemical kinetics mechanism.

Ambient Temperature

Fig. 6.7 compares computed and experimental cylinder pressure and AHRR for the Cases 2, 1 and 3 with targeted TDC temperature of 800K, 900K, and 1000K. In experiments, the main effect of ambient temperature on combustion process seems to be related to the amount of fuel which burns during the so-called premixed combustion

phase. Case 2 having the lower TDC temperature presents the highest premixed peak which is still present in Case 1 and it almost disappears in Case 3. For all the three considered cases, simulations reproduce rather well the cylinder pressure trace, however a detailed analysis of AHRR traces allows to better compare the tested combustion models. Table 6.4 compares the ignition delay calculations of the applied models to the experiments.

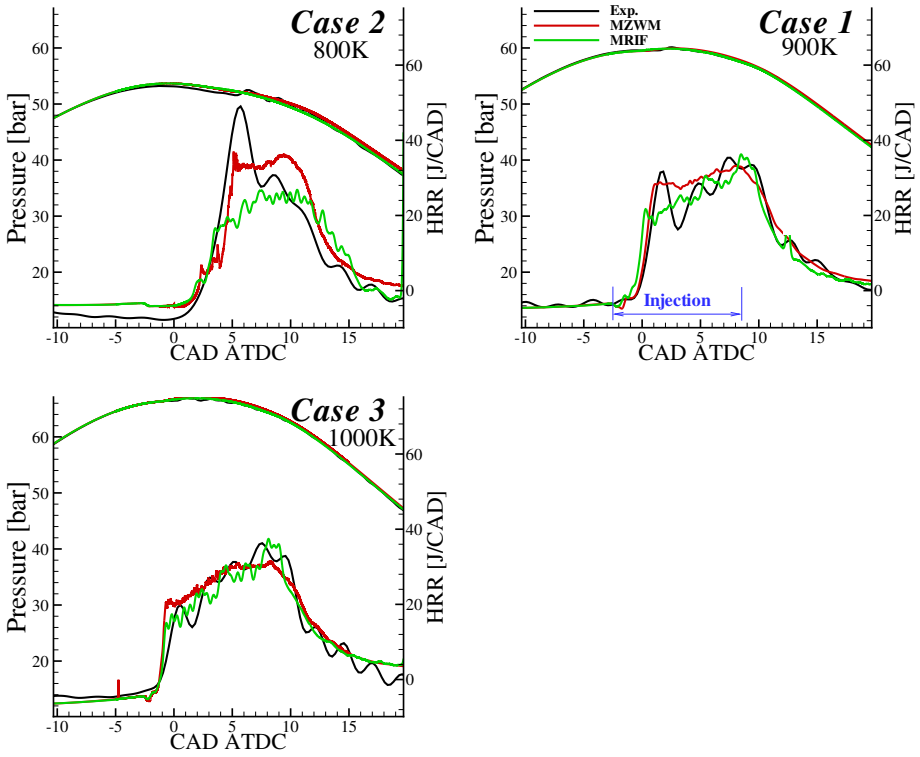

Figure 6.7: *Cylinder pressure and AHRR for MZWM and MRIF models compared to the experimental data of the Case 2, 1, and 3 with targeted TDC temperature of 800K, 900K, and 1000K, respectively.*

Table 6.4: *Experimental ignition delay time [μs] for different targeted TDC temperatures compared to the simulation results of MZWM and MRIF models.*

Case TDC Temp.	Exp.	Sim. MZWM	Sim. MRIF
800K	886 $\pm$34	845	601
900K	354 $\pm$19	345	321
1000K	159 $\pm$69	192	151

Several differences can be found between two models as stated below and then discussed, respectively:

1. Even if by a small amount, ignition delay time is always shorter in the MRIF model compared to MZWM model.

2. Magnitudes of the premixed burn are generally better predicted by the MZWM model.

3. Heat release during the diffusive combustion is better predicted by MRIF model and MZWM model over-predicts the AHRR.

4. AHRR computed by the MZWM model decrease earlier than MRIF model after end of injection.

Discussion 1. Ignition delay results of the models were shown in Table 6.4. Differences in ignition delay of the models can be mainly ascribed to the evolution of mixture fraction and its variance in the applied models. In MRIF, the scalar dissipation rate governing evolution of species and energy in the mixture fraction space depends on the mixture fraction variance $\widetilde{Z''^2}$ and turbulent mixing time k/ε. In particular, $\widetilde{Z''^2}$ generation is proportional to the magnitude of the mixture fraction gradient while destruction depends on the scalar dissipation rate. For the well-mixed model, a transformation from spatial coordinates (Cartesian *x, y, and z*-t) to the mixture fraction frame of reference (*Z*-t) shows that the corresponding scalar dissipation rate value for the well-mixed model is:

$$\chi = 2\frac{\mu_t}{Sc_{\widetilde{Z''^2}}}\left|\nabla Z\right|^2 \tag{6.1}$$

Compared to the χ value as determined in Eqn. 3.6 used by the MRIF, this is expected to have a different evolution during the injection phase and immediately after its finishing.

Before ignition, the main effect of turbulence is reducing the mixture fraction variance at the jet periphery. This is responsible for χ decreasing below the extinction value and thus enhances ignition. However, when the χ is reduced under the extinction limit, it is discussed that turbulence has less effects on ignition [196] and ignition is initiated from a mixture fraction so-called *Most Reactive mixture fraction* Z_{MR} with low scalar dissipation rate. Z_{MR} depends on: temperature of the

fuel, temperature of the oxidizer, and activation energy required for ignition [196]. In other words, although TCI does not explicitly affect ignition of Z_{MR}, turbulent sub-grid scale mixing helps reducing fuel rich spray periphery to the magnitude of Z_{MR}. As discussed in §5.2.5, embedded TCI through scalar dissipation rate in the flamelet concept, enhances mixing in the spray periphery and smooths the mixture fraction field faster than MZWM model even before ignition.

Discussion 2. After ignition, there is a premixed combustion phase (first peak in the AHRR diagrams). The MRIF model is not able to predict the premixed peak properly. During the premixed combustion phase when using multiple flamelets, it can occur that several flamelets still have scalar dissipation above the extinction limit, which reduces the premixed peak. This suggests the need to introduce suitable interaction models among flamelets. Premixed combustion phase is properly reproduced by the MZWM model due to its capability to account for spatial convection and diffusion in physical space. In MRIF model, however, flamelet equations are solved in the mixture fraction gradient direction and physical convection and diffusion are implicitly taken into account by mixture fraction and its variance transport in the CFD domain.

Discussion 3. There is a transient process after premixed combustion phase where the reactivity of the mixture shifts from the ignited mixture fractions mainly to Z_{St} (Stoichiometric Mixture Fraction) and then diffusive flame is going to be established. When the diffusive flame is established the time-derivative term in Eq. 3.10 vanishes. Under such conditions, the burning rate only depends on the mixing and scalar dissipation rate. If we again consider the transformation from spatial coordinates to the mixture fraction frame of reference, MZWM model has higher scalar dissipation rate due to not considering turbulence-chemistry interactions (last term in the RHS of Eq. 3.5) resulting in higher mixture fraction gradient. As in this stage (stoichiometric mixture fraction is ignited) discussed higher mixture fraction gradients of MZWM model result in very thin flame with high reactivity gradients. This can be seen in Fig. 6.8 that MZWM model has higher peak temperature as majority of mixture fractions are reacting in thermodynamic equilibrium state comparing to the MRIF model. This is not the case for MRIF model as reactivity is smoothed due to scalar dissipation rate as negative source term in Eq. 3.5 and the flame modeled by MRIF model has wider reactive brush than a

flame modeled by MZWM model. This is also can be seen by a mixture fraction-temperature diagram in Fig. 6.8. For an already established diffusive flame for the MRIF model there are more scattered ignited mixture fractions in between mixing line and thermodynamic equilibrium lines compared to the MZWM model. These intermediate thermodynamic states of the MRIF model were resulted in thickened reactive flame brush.

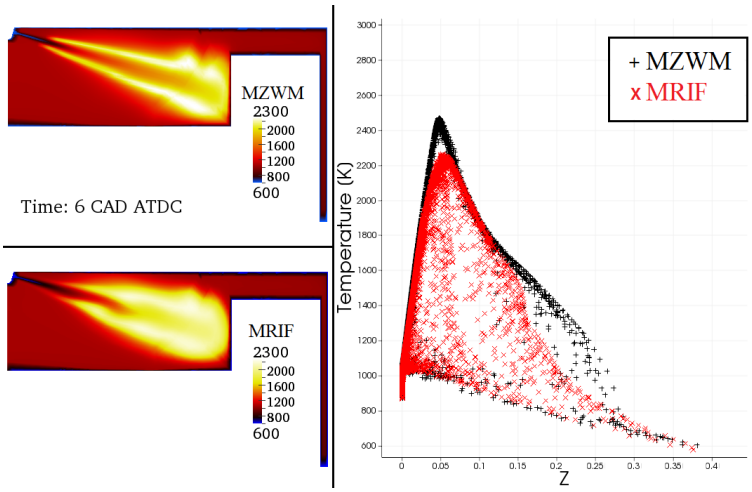

Figure 6.8: *MRIF and MZWM models results of Mixture fraction-Temperature diagram for the established diffusive flame of Case 3 at 6 CAD ATDC together with temperature contours ($Z_{St} = 0.054$).*

Discussion 4. At the end of injection, there is a fast decay of turbulence in the computational domain and this phenomenon is immediately detected by the equivalent scalar dissipation rate of the MZWM model. Hence, the burning rate decays immediately after injection ends. Compared to MZWM, decay of the burning rate is delayed by a couple of engine cranks when the MRIF model is used. This is mainly due to the fact that the sub-grid mixing is taken into account the scalar dissipation rate and this is responsible for its slower decay towards the end of injection.

Experimental and numerical results of MZWM and MRIF combustion models for the mean flame lift-off length of the Spray B experiments for different targeted TDC temperatures are shown in Fig.6.9. Since lift-off length is mainly related to the model capability to predict diffusion combustion. The flame lift-off length in the MZWM shows much larger sensitivity to temperature, over-shooting at lower temperature and

under-predicting at higher temperature. The MRIF model under-predicts the flame lift-off at 800K, but the 900K and 1000K lift-off length predictions lie within one standard deviation of the experimental result.

More representation of model-to-model comparison for lift-off length can be seen from Fig.6.10 for the spatial flame images based on OH contour. A threshold of 14% of maximum OH are used to locate the flame lift-off length. At 9 CAD ATDC (established diffusive flame) in the Fig.6.10 flame lift-off of the MRIF model is closer to the experimental value, whereas the MZWM model over-estimates.

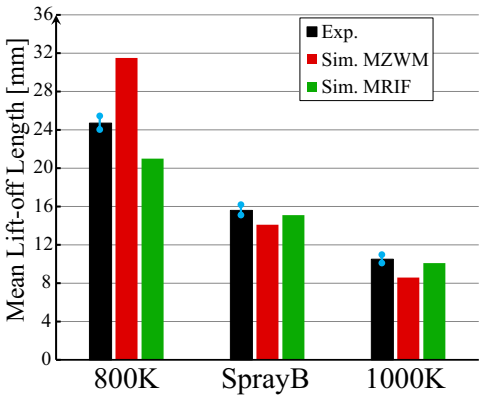

Figure 6.9: *Mean Flame lift-off length comparisons of MZWM and MRIF combustion models for Spray B experiments in different targeted TDC temperatures.*

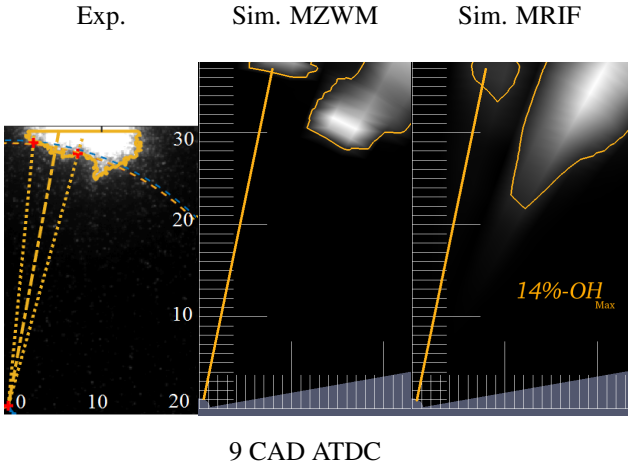

Figure 6.10: *Top view of the combustion chamber. Limits of diffusive flame at 9 CAD ATDC for Case 2 (origin in this figures is the location of the injector orifice).*

Ambient Density

Here, two different density values at SOI were considered: 22.8kg/m^3 for Case 1 and 15.2kg/m^3 for Case 4. Effects of density change will be dominated by differences in the fuel-air mixing process and momentum exchange. Fig. 6.5 shows an increase of 3 mm for the liquid penetration for the condition with lower ambient density. Fig. 6.11 plots the comparison between computed and experimental values of AHRR for Cases 1 and 4. Tab. 6.5 has the computed ignition delay times.

Table 6.5: *Experimental ignition delay time [μs] for low density and baseline case compared to the simulation results of MZWM and MRIF models*

Case Density	Exp.	Sim. MZWM	Sim. MRIF
15.2 Kg/m^3	612 $\pm$22	571	383
22.8 Kg/m^3	354 $\pm$19	345	321

Ignition delay both in experiments and simulations are reduced by increasing ambient gas density. This is due to higher evaporation and mixing taking place when liquid spray faced denser ambient gas and reduction of mixture fraction to the value of most reactive mixture fraction, Z_{MR}, is accelerated. At the lower density, ignition delay is under-predicted by both models. The sensitivity of MRIF to density is exaggerated, while ignition delay time from MZWM is in better agreement with experimental data. Both models predict a small positive AHRR almost immediately after SOI, while the experiment has a similar magnitude, it is phased about 2 CAD later. Considering that both liquid and vapor penetration are rather well predicted for Case 4, the underestimation of the ignition delay time by MRIF model such as the discussion in *Ambient Temperature* sub-section is mainly due to higher level of smoothing of mixture fraction variance in this model compared to the MZWM model. Fig. 6.12 compares predictions for the effect of ambient density on flame lift-off length. Based on the chosen threshold, the MZWM model under-predicts the lift off length at high-density and over-predicts the length at low density. The MRIF model is within one standard deviation at 22.8Kg/m^3 and slightly under-predicts the length for 15.2Kg/m^3 .

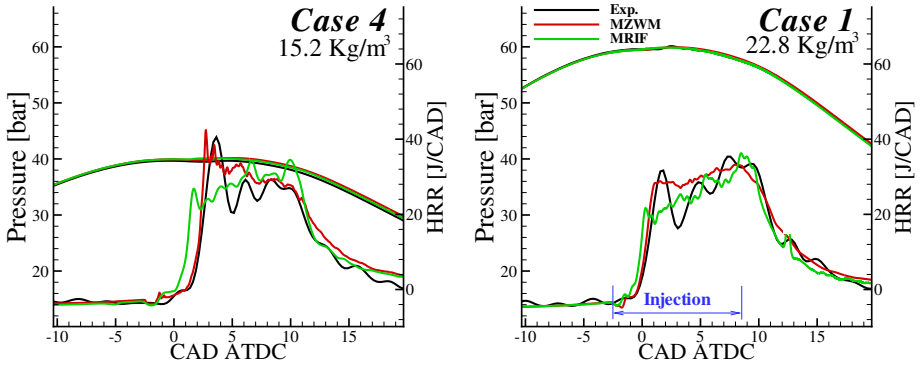

Figure 6.11: *Cylinder pressure and AHRR for MZWM and MRIF models compared to the experimental data of the Case 4 and 1 with targeted TDC density of 15.2Kg/m^3 and 22.8Kg/m^3, respectively.*

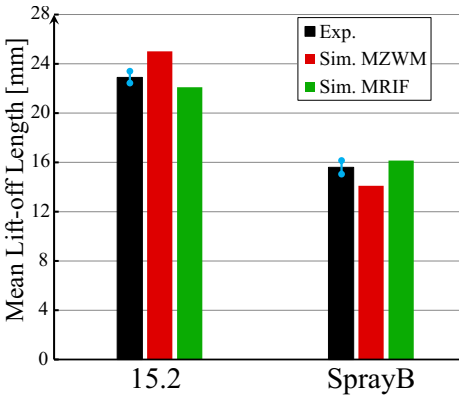

Figure 6.12: *Mean Flame lift-off length comparisons of MZWM and MRIF combustion models for Spray B experiments for lower density and baseline case.*

Flame Brush Comparison

Figure 6.13 represents the MRIF and MZWM model results of OH contours for Case 1 and Case 4 and scaled to the maximum and the applied threshold of 14% of maximum OH at 6 CAD ATDC. Liquid fuel particles are shown in white points and *Exp. LL* is the mean experimental liquid penetration length. Stoichiometric mixture fraction is shown by a solid black iso-line and *Exp. LOL* is the mean experimental flame lift-off length. It can be seen that MRIF model can comparably predict mean experimental lift-off length located on the iso-line of stoichiometric mixture fraction (solid black line). From OH contours it can be seen in low ambient density case larger liquid penetration length result in distant stabilization of the diffusive flame. Before

the ignition and due to Sandia optical engine bowl geometry, fuel vapor in low ambient density case is more accumulated on the radial direction of the spray axis. This is resulted in wider flame brush comparing to the high ambient density case. In case of model-to-model comparison, for both cases MZWM model predicts thinner and more reactive flame brush than MRIF model. The reason for this was discussed in the *Ambient Temperature* sub-section as MRIF resulted (due to considering TCI) in wider reactive mixture fraction span which is more consistent with what is expected for highly turbulent non-premixed flames observed in the experiments [101].

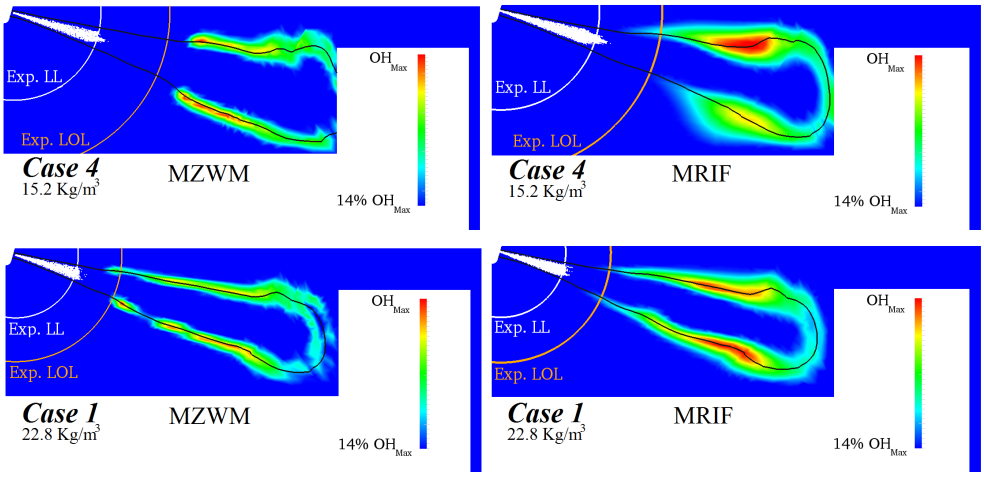

Figure 6.13: *OH contour of the Case 1 and Case 4 for MRIF and MZWM models at 6 CAD ATDC.*

Ambient O_2 Level

Figure 6.14 shows that AHRR is a little elevated by moving to $21\%O_2$. High over-prediction of the premixed burn for the highest O_2 level in MZWM model can be due to homogeneous reactor assumption in the well-mixed model and chemical heat release was intensified due to higher availability of O_2. During the mixing-controlled combustion phase, MRIF model better estimates the AHRR profile compared to MZWM . Increasing of the oxidizer level advances combustion as shown in ignition delay results in Table 6.6 where almost half of the time is needed for a mixture in Case 6 to ignite comparing to the baseline case. Due to the different flame structure assumption from the two models and consistently with what was found in previous sections, ignition delay time computed by MRIF is lower than the one estimated by the MZWM model.

Table 6.6: *Experimental ignition delay time [μs] for different O_2 levels compared to the simulation results of MZWM and MRIF models*

Case O_2 level	Exp.	Sim. MZWM	Sim. MRIF
13%	441 $\pm$12	465	355
15%	354 $\pm$19	345	321
21%	153 $\pm$21	221	115

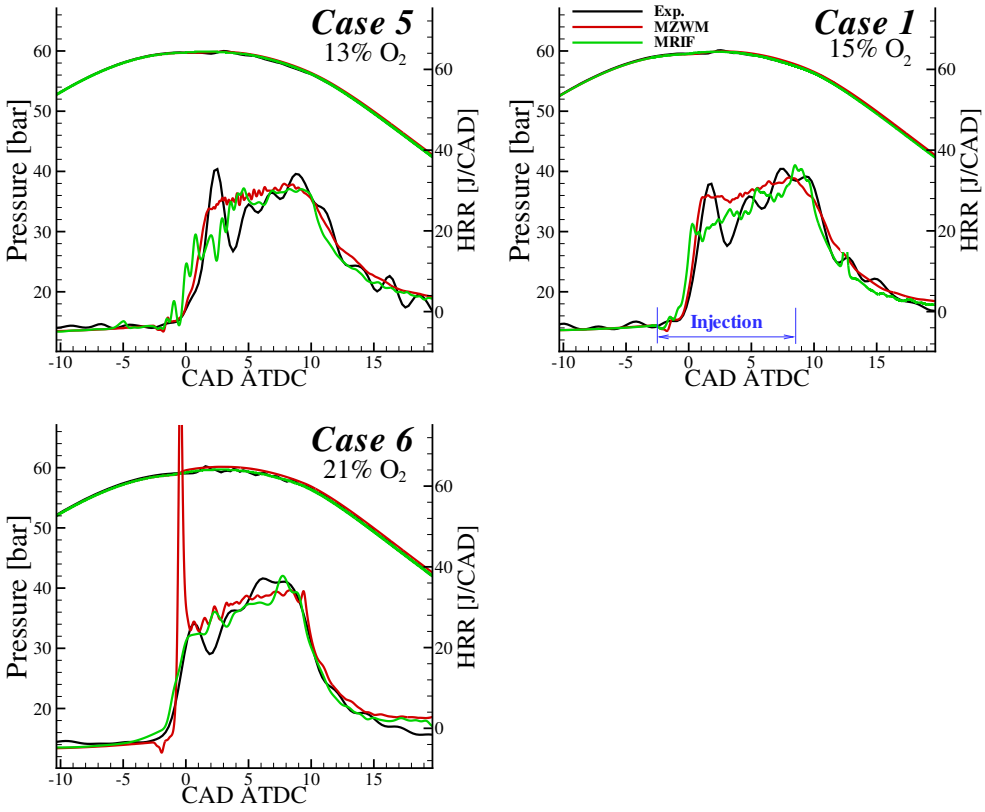

Figure 6.14: *Cylinder pressure and AHRR for MZWM and MRIF models for different O_2 levels compared to the experimental data.*

Flame lift-off for different O_2 levels in Fig. 6.15 show that both in experiments and simulations lower lift-off lengths result from increasing the O_2 level. MZWM model systematically under-predicts the lift-off length at all $\%O_2$ conditions. Without the influence of strain and extinction on the combustion progress, the MZWM model predicts more reactive mixtures and shortened flame lift-off length.

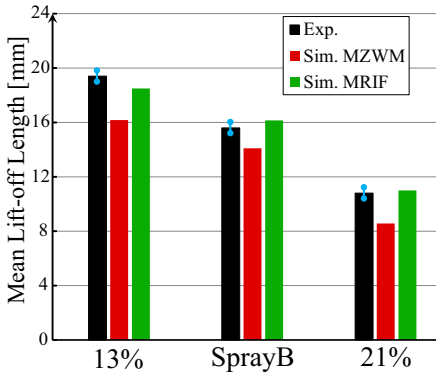

Figure 6.15: *Mean Flame lift-off length comparisons of different O_2 level for MZWM and MRIF combustion models for Spray B experiments.*

Injector Rail Pressure

Injection pressure affects the fuel-air mixing process and influences both ignition delay and flame lift-off values [171]. D'Errico et al. [197] were shown for constant volume chamber calculations that when increasing injection pressure, temporal evolution of the scalar dissipation rate reduces the ignition delay but, at the same time, the length at which flame stabilizes grows. In the early stages of the injection process, the region of where scalar dissipation rate is higher than the extinction value is larger for the low pressure conditions while the opposite happens during the quasi steady part of the injection process. Ignition delay data reported in Table. 6.7 confirms such experimental trend.

Table 6.7: *Experimental ignition delay time [μs] of different injector rail pressure compared to the simulation results of MZWM and MRIF models*

Case Inj. rail pres.	Exp.	Sim. MZWM	Sim. MRIF
500 bar	457 $\pm$32	310	251
1000 bar	384 $\pm$14	335	256
1500 bar	354 $\pm$19	345	321

In simulations, neither MZWM nor MRIF can properly reproduce experimental data. A possible reason for such discrepancy is the mesh size close to the nozzle, which is not fine enough to reproduce the scalar dissipation rate distribution in the near nozzle region. The use of a more refined grid will probably improve ignition delay prediction as function of injection pressure. During the mixing-controlled combustion phase, Fig. 6.16 illustrates that AHRR is always better predicted by the MRIF model.

The largest differences between MZWM and MRIF are mainly for Case 1 where injection pressure is the highest and, consequently, effects of turbulence on combustion will be more significant.

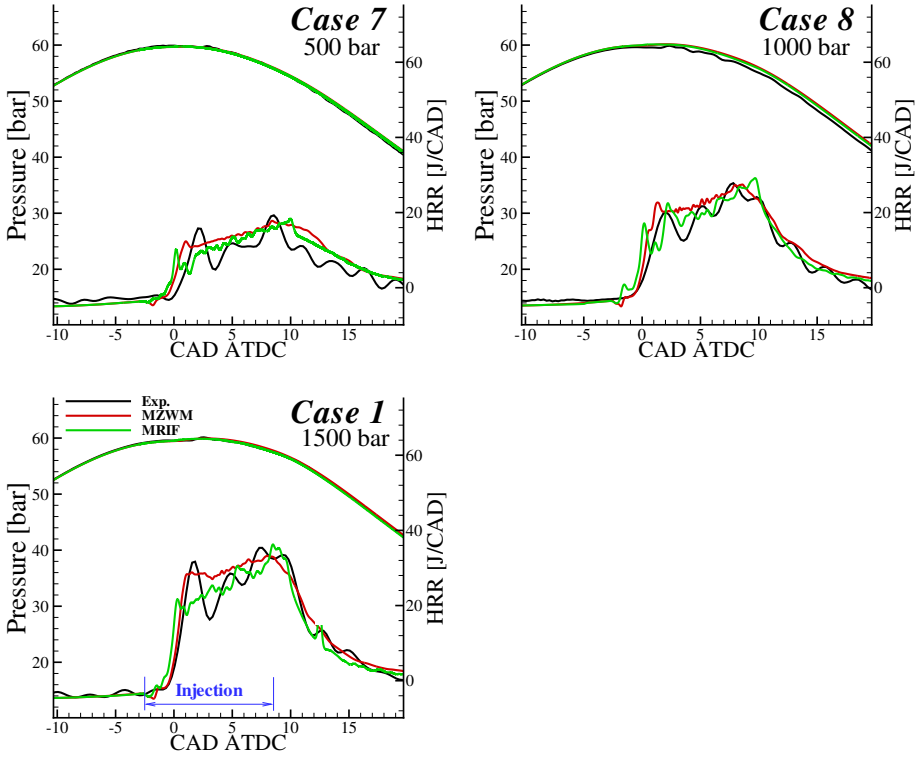

Figure 6.16: *Cylinder pressure and AHRR of different injector rail pressure for MZWM and MRIF models compared to the experimental data.*

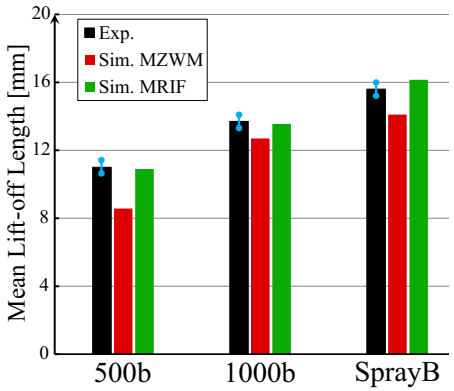

Figure 6.17: *Mean Flame lift-off length comparisons of different injector rail pressure for MZWM and MRIF combustion models for Spray B experiments.*

Concerning the flame lift-off length, Fig. 6.17, the MRIF model always predicts within the standard deviation of the experimental measurement. The lift-off is systematically under-predicted by the MZWM model, which also shows a stronger sensitivity to the lowest rail pressure than in either the experiment or MRIF model.

6.3 Conclusions

The availability of the large set of experimental data for ECN Spray B in Engines made it possible to compare simulations across a wide engine map with well controlled boundary conditions. The comparisons used identical approaches for mesh generation, and turbulence modeling. Attention was first dedicated to non-reacting conditions, where the dependency of steady-state liquid penetration as function of ambient temperature, density and injection pressure. Vapor penetration was also compared for the considered cases. These assessments indicated that the proposed turbulence modeling approach, a *k*-ε model, including the proposed correction on the $C_{\varepsilon 1}$ based on vessel simulations and applying spray-oriented grid, can reasonably reproduce the liquid and vapor penetrations.

The aim of this chapter was the assessment of the well-mixed reactor and flamelet modeling approaches for combustion process in Diesel engines. The trends in the results agree well a previous numerical study in this engine with a different injector and fuel, comparing predictions of combustion characteristics of ignition delay and AHRR using either well-mixed or flamelet based combustion models [155]. In both studies flamelet based models predict earlier ignition and more accurate flame lift-off predictions due to embedded turbulence-chemistry interactions.

This work extends the prior art through additional comparisons of liquid length, vapor penetration, in-cylinder pressure, AHRR, and quantification of the ignition delay and flame lift-off length. Flamelet method generally predicted shorter than measured ignition delays, but estimated flame lift-off length within the experimental uncertainty. The well-mixed model more accurately, though still slightly under-predicted, ignition delay relative to the measurements. During injection, the well-mixed model also predicted shorter flame lift-off lengths and a thin flame brush compared to MRIF model, which has implications for *different* prediction of soot and NO_x levels with this modeling approaches. Both combustion models reasonably estimated premixed burn magnitude and mean AHRR, with the flamelet model typically lower than the well-mixed

model between 0 and 15 CAD ATDC. However, both models fell well within the experimental uncertainty when considering the filtering applied.

Improvements in the prediction of the ignition delay, in particular on predicting effects of injection pressure, may be improved by increasing mesh resolution employed close to the nozzle. Results achieved in this Chapter were based on expert judgment of the correct thresholds to evaluate ignition delay and the flame lift-off. Further refinement of these choices, perhaps in conjunction with multiple simultaneous experimental diagnostics, such as heat release rate and optical imaging of ignition is a subject of prospective future studies.

CHAPTER 7

Low Temperature Combustion

In order to reduce greenhouse gas emissions and reliance on increasing fossil fuel demand, there is a need for strong drivers for increasing the fuel efficiency of passenger cars and power generation units utilizing combustion. Using Diesel engines in the vehicles is a cost-effective, easily implemented strategy for reducing fuel consumption and attendant CO_2 emissions. However, relatively high *NOx* and particulate matter emitted by Diesel engines increases their cost and raises environmental barriers that prevent their widespread market penetration. Consequently, research into automotive-class Diesel engines is focused on Low Temperature Combustion (LTC) techniques that can reduce emissions in-cylinder, without sacrificing engine efficiency and fuel consumption.

7.1 Low Temperature Combustion Approaches

Since introduction of Diesel engine emission standards that have forced applying after-treatment systems for *NOx* and Diesel Particulate Matter (PM), evolution of the Diesel combustion process has been significant. Advanced combustion strategies have at-

tempted to find an in-cylinder approach to either meet these emission standards and thus avoiding the need to use after-treatment or at the very least, to lower the performance demands required from after-treatment systems and thus reducing their cost and complexity. While the main focus of combustion system development has been to lower emissions of *NOx*, there is also significant interest to lower PM emissions. Many of these advanced combustion systems carry numerous handles such as Homogeneous Charge Compression Ignition (HCCI) [198–200], Premixed Charge Compression Ignition (PCCI) [201–203], and Partially Premixed Compression Ignition (PPCI) [204–207] engines that can meet strengthened emission regulations. HCCI was one of the early Diesel combustion concepts that differed from the conventional Diesel process to attract attention. As the name implies, the goal of early HCCI work was to achieve as homogeneous air-fuel mixture as possible before ignition similar to a conventional spark ignition engine. This can be achieved either by injecting fuel into the intake port or directly into the cylinder and allowing sufficient time between injection and ignition to allow complete mixing of air and fuel. The charge then ignites as it is heated by the compressed gases where no spark or other means of forced ignition is used. In order to address many of the challenges such as limited load range, controllability and knocking posed by HCCI, a number of other concepts have evolved from this homogeneous charge approach and in many cases, charge stratification was introduced. Since the term HCCI may no longer accurately describe many of these systems, the term LTC can be used as a general term to refer to these and other advanced combustion concepts because the overall goal is to lower combustion temperatures to advantageously alter the chemistry of *NOx* and/or soot formation. HCCI Diesel combustion using Diesel fumigation in the intake port was first described in 1958 [208]. Further work in the late 1970s [209, 210] reported stable spontaneous ignition in a two stroke gasoline engine with port fuelling that was attributed to the presence of active radicals. While the focus of many of these early publications was on light fuels (gasoline) in two stroke engines, later work described the same type of combustion with Diesel fuel in four stroke engines [198, 211].

7.2 HCCI Engine Combustion Modeling

HCCI is a thermal ignition process that initiates simultaneously at numerous sites before rapidly spreading throughout the combustion chamber [212]. HCCI ignition con-

trasts sharply with the turbulent flame propagation of SI engines and the mixing controlled combustion of CI Diesel engines. Ignition begins in slightly hotter spots formed due to non-uniformities in temperature or concentration [213]. Combustion then propagates as a pressure wave from these initial ignition points. The expansion of hot reaction products compresses and heats the unburned fuel and air that is adjacent to the initial ignition points. In general, numerical simulation of HCCI combustion is mainly rely on thermal load, ignition, and the applied chemistry [214]. Turbulence plays an indirect role in HCCI combustion. The role of turbulence is limited to controlling heat transfer to the cylinder walls, thereby establishing the temperature distribution in the cylinder. Both thermodynamic and CFD formulations can be applied using multi-zone approach. In thermodynamic models energy equation is the main governing conservation equation while in CFD all transport phenomena is taken into account. CFD methodology and formulation of the multi-zone chemistry model is represented in §3.2.1. HCCI experiments and simulations of Hessel et al. [212] is used in the following to reproduce the results using MZWM combustion model.

7.2.1 Experimental Setup and Operating Conditions

Hessel et al. [212] conducted the experiments on a Sandia National Laboratories research engine. The engine is based on the Cummins B-series, a typical medium-duty Diesel engine with the specifications given in Table 7.1. For all cases the engine speed is 1200rpm with fully premixed iso-octane in HCCI mode. Equivalence ratio was swept from 0.08 to 0.28 in steps of 0.02. For each case, intake temperature is adjusted to maintain the 50% heat release point at TDC.

Table 7.1: *Engine specifications and model inputs [212]*

Fuelling mode	Fully premixed
Bore × Stroke	102 × 120mm
IVC, EVO	-160, 120 CAD ATDC
Compression ratio	13.5
Swirl ratio	0.9
Engine speed	1200rpm
Intake temperature	468K-478K
Intake pressure	1.35bar

7.2.2 Mesh Generation and Boundary Conditions

To accelerate the HCCI simulations a two dimensional mesh is generated as it is shown in Fig.7.1 at TDC. Piston crevice shape was reconstructed based on Hessel's simulations [212].

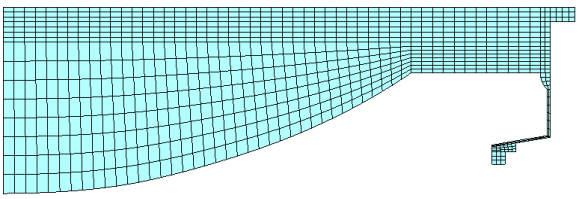

Figure 7.1: *2D grid for iso-octane HCCI engine at TDC*

To commence the simulations all engine variables such as compression ratio, engine speed, and turbulence and wall functions were kept constant and only equivalence ratio of the premixed iso-octane and air mixture was changed. Table 7.2 summarizes initial conditions considered in HCCI simulations.

Table 7.2: *Boundary and initial conditions for the HCCI Simulations*

Case	$\phi = 0.14$	$\phi = 0.20$	$\phi = 0.28$
Internal $Temp._{IVC}$ [K]	476	474	468
Piston Temp. [K]	428	440	452
Liner Temp. [K]	382	383	385
Head Temp. [K]	401	406	412
P_{IVC} [bar]	1.36	1.36	1.36
Fuel mass fraction	0.00884	0.01265	0.01774

7.2.3 HCCI Simulation Results

MZWM model applied to the HCCI simulations in the same way it is discussed in in §3.2.1. Chemical kinetics mechanism of Wallesten and Golovitchev [215] with 82 chemical species and 413 reactions were used. Figure 7.2 shows the experimental and numerical MZWM models pressure curves. It can be seen that MZWM has comparable results to the experiments in case of ignition time and magnitudes of peak pressure. It is also showing that by strengthening the air-fuel mixture (richer mixtures) cylinder pressure rise and peak values are increasing. However, there is not a significant change in the ignition time due to the applied intake temperature of the charge.

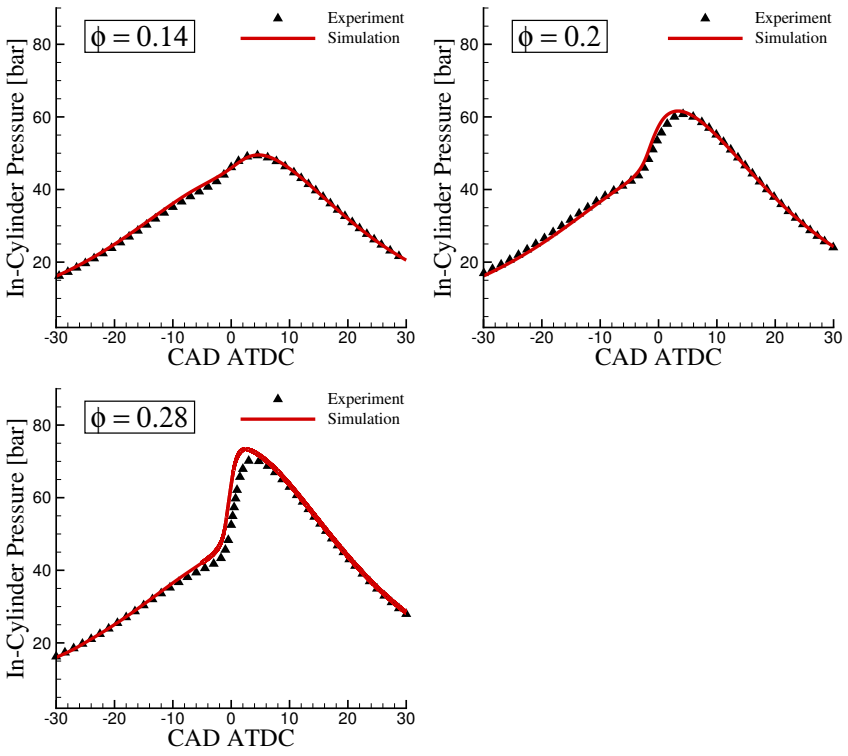

Figure 7.2: *In-cylinder experimental and numerical comparison of pressure for HCCI combustion for* $\phi = 0.14$*,* $\phi = 0.2$*, and* $\phi = 0.28$*.*

Reliable simulation results under HCCI mode is highly necessary when later PPCI simulations is going to be performed. It will be discussed that PPCI combustion occurs in stratified mixture and its evolution is similar to the premixed combustion as scalar dissipation rates within the computational domain are very low.

7.3 PPCI Engine Combustion Modeling

PPCI combustion is one of the LTC techniques is being actively investigated. LTC of PPCI mode enables significant reductions of both soot and *NOx* emissions, however, increases in unburned hydrocarbon (UHC) and *CO* emissions are often incurred. Comparing to HCCI mode, PPCI combustion provides better control on the ignition timing and noise reduction due to lowered rate of heat release which is very common in kinetically controlled HCCI combustion [16, 26, 206, 207]. In order to get insights of PPCI combustion, simulations of a light-duty Diesel engine operating under PPCI mode are conducted and results will be discussed in the following sections.

7.3.1 Experimental Setup and Operating Conditions

PPCI engine experiments were conducted in Eindhoven University of Technology on a light-duty Volvo D5 Diesel engine [216]. The engine was modified for optical access from cylinder side and bottom for investigating effects of the SOI on ignition sensitivity of PPCI. As images were taken from the bottom of the cylinder a flat glassy piston was used to provide optical access to the combustion chamber. Applied fuel for the experiments was PRF70 which is less reactive than conventional Diesel fuel. This less-reactive characteristic of the applied fuel extends the ignition delay at elevated loads of PPCI combustion. Engine specifications and operating conditions were shown in Table 7.3. The engine was motored at 1200 rpm by using a dynamometer. An artificial EGR system was used to dilute the intake air by adding nitrogen. Intake pressure and temperature were also controlled using a compressor and heater. Intake air temperature was slightly changed for different injection timings to have similar engine time of the second stage (main stage) ignition.

Table 7.3: *Engine specifications operating under PPCI mode [216]*

Bore × Stroke	81×93.2 mm
Connecting rod length	147 mm
Compression ratio	12.6:1
Swirl ratio	1.8
Speed	1200 rpm
Number of injector holes	7
Spray pattern included angle	140°
Intake pressure	1.2 bar
Intake temperature	350-380 K
Injected fuel mass	16 mg/cycle

To investigate effects of injection timing, SOI was swept from -100 to -20 CAD ATDC for three different single-injection strategies of 640 bar (Case A), 500bar (Case B), and 420bar (Case C) with injection duration of 5 CAD, 6 CAD, and 7 CAD, respectively. Experimentally, the engine was operated in a skip-fire mode (once every 10^{th} engine cycle) to reduce the required cleaning frequency of the optical piston and liner, and the risk of liner failure due to thermal and mechanical stresses. To assess the ignition sensitivity, SOI has been advanced and retarded for 2 CAD for each measurement point (2×19 extra measurement points) and CA50 variation has been measured for this small SOI differential. Izadi et al. [216] then defined the ignition sensitivity as

the ratio of CA50 (Crank Angle 50) differential to SOI differential and quantified it for the different injection timing experiments as shown in Fig. 7.3.

At intermediate SOI from -60 to -25 CAD, ignition sensitivity acts unexpectedly, particularly around -50 and -30 CAD where the combustion was advanced by retarding the injection timing [216]. Considering a hypothesis of "later injection, later combustion" for late injection timing, two unexpected regions were highlighted in Fig. 7.3. Izadi et al. discussed that early injection timing (-100 CAD) causes liquid fuel to hit the liner and by the end of injection, this liquid stain on the liner evaporates after some crank angle degrees. Due to experimental limitations, the glass piston had a larger crevice volume compared to the metal piston and this caused trapping of a considerable amount of evaporated fuel in the piston crevice which cannot participate in combustion. Spray-liner impinging reduces with further retarding the SOI due to elevated cylinder pressure at late engine crank angles. For injection timing from -60 to -45 CAD ATDC, there was the maximum amount of trapped fuel in the crevice volume due to piston position and injection angle, causing poor combustion efficiency and low ignition sensitivity. For injection later than -50 CAD ATDC, the liquid spray did not hit the liner. However, for injection from -35 to -25 CAD, liquid spray hit the piston crown in relatively cold thermal situations, causing poor mixing and low ignition sensitivity. These unexpected regions were shown in yellow areas in the Fig. 7.3.

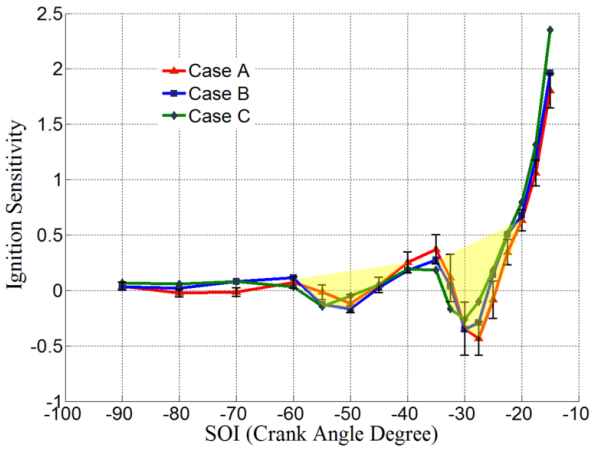

Figure 7.3: *Ignition sensitivity as a function of injection timing for different injection strategies of PPCI combustion for Case A, B, and C reported by Izadi et al. [216]*

Combustion stratification levels of the experimental cases for different start of injection times were shown in Fig.7.4. The methodology to calculate these stratification

levels was based on angular stratification driven from OH^* chemiluminescence images analyzed in a cylindrical coordinate system [216]. The intensity was radially averaged and plotted as a function of polar angle. Based on the minimum and maximum intensities combustion stratification was quantified for each operating conditions.

Experimental data shows that stratification of *Case C* was the highest among two other cases and this case was used to perform numerical simulations because its larger range of air-fuel stratification. In the numerical simulations no crevice flow model and blow-by were considered, although large crevice volume can possibly create blow-by and loss of mass. To minimize mentioned issues numerical simulations were conducted for start of injection at -80 and -40 CAD ATDC. Based on represented experimental data in Fig. 7.3, these injection timings were not in the highlighted zone with unexpected ignition sensitivity behavior. Hence, numerical study can mainly focus on the level of stratification of the cases.

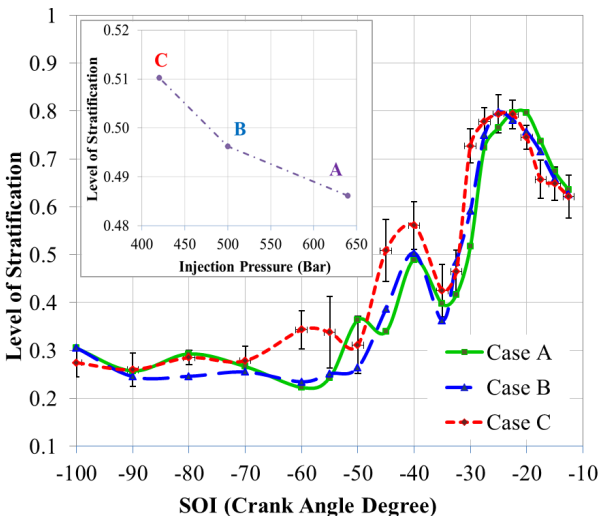

Figure 7.4: *Stratification level of PPCI combustion of Case A, B, and C as a function of injection timing reported in [216]*

7.3.2 Mesh Generation and Boundary Conditions

Mesh generation was carried out for the engine with the specification in Table 7.3 and it can be seen in Fig. 7.5 at TDC. A *Spray Oriented* sector grid was generated with considering the crevice volume (to match the engine compression ratio) and seven injector nozzles. Mesh generation was performed based on automatic grid generation tool [193]. This method of grid generation keeps the grid fixed on top of the combustion chamber

and aligned to the spray injection axis. Layers of the cells then can be added/removed below these fixed grids during the piston movements. For the PPCI combustion with very early injection timings, spray oriented grid will be very beneficial to have more accurate air-fuel mixing predictions. Periodic boundary condition was considered on side faces for the mesh. Cylinder head, piston, and liner wall temperatures were set to 420 K, 460 K, and 470 K, respectively. These temperature values were obtained by matching the trapped air mass in the simulations with air flow rate of the experiments and performing motoring simulations to accurately predict experimental motoring pressure curves.

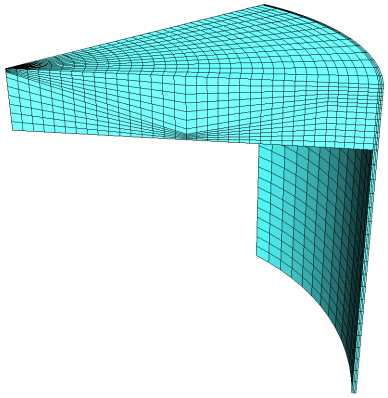

Figure 7.5: *Spray oriented sector grid for the PPCI engine combustion simulations at TDC*

7.3.3 Combustion Model

The Multi-Zone Well-Mixed combustion model (§3.2.1) was used as the combustion model and Liu's PRF mechanism [217] with 41 chemical species and 124 chemical reactions was used as reaction mechanism. Although sub-grid turbulent mixing is not considered in the MZWM model, when applied to PPCI combustion it was expected to provide a reasonable estimation of auto-ignition time and burning rate. In other words, comparing to the conventional Diesel combustion, as generally PPCI ignition occurs much later than end of injection, scalar dissipation rate in the air-fuel mixture drops to very low values and gets very close to well-mixed assumption. This is why many researchers reported that results of the models with embedded sub-grid scale turbulent mixing do not differ a lot when compared to the well-mixed combustion models [106, 218]. Nevertheless, for retarded PPCI injections, applying models such as MRIF with embedded TCI effect is necessary and matter of future research.

7.3.4 PPCI Simulation Results

Cylinder Pressure for Low and High Air-Fuel Mixture Stratification Level

Initially, in-cylinder pressure results of SOI -80 and -40 ATDC were compared with experimental data in Fig. 7.6. These two cases represent low and high mixture stratification levels as depicted in the experimental results of Fig.7.4. Figure 7.6 also shows that MZWM model is capable of acceptable predictions for the PPCI combustion with low and high level of air-fuel mixture stratification. It then would be worth studying the mechanism of combustion initiation and progress with noticeably different stratification levels.

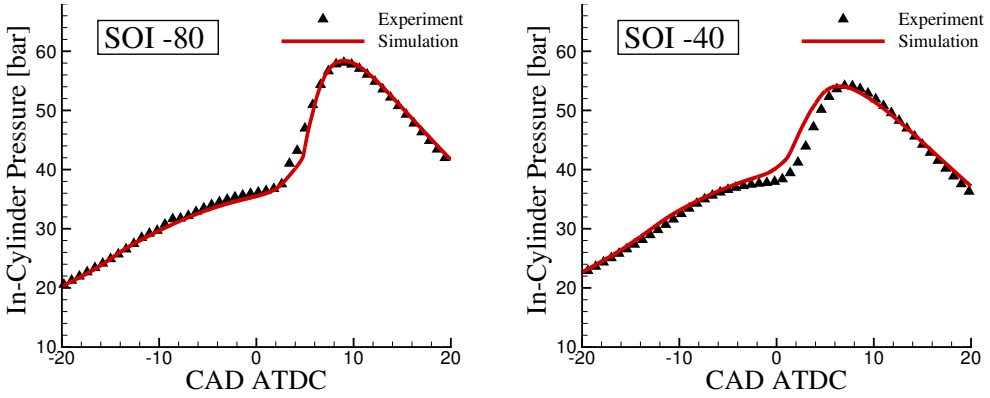

Figure 7.6: *In-cylinder pressure comprason with experimental data for SOI of -80 and -40 ATDC.*

OH^* Chemiluminescence as the Marker of the First Stage Ignition

In the experiments, chemiluminescence was captured which corresponds to OH^* as good indicator of the ignition process under PPCI engine condition. OH^* chemistry pathways were added to the applied chemical kinetics mechanism enabling introduction of OH^* mass fraction as a transportable scalar. Figure 7.7 represents images (top view) of the D5 engine combustion chamber at the time of the first stage ignition: -16 CAD ATDC for SOI -80 and -12 CAD ATDC for SOI -40. Magnitudes of OH^* were normalized to the maximum value in the experiments in each image and in the CFD simulations. MZWM model was able to predict spatial distribution of OH^* and its local peak compared to the experiments.

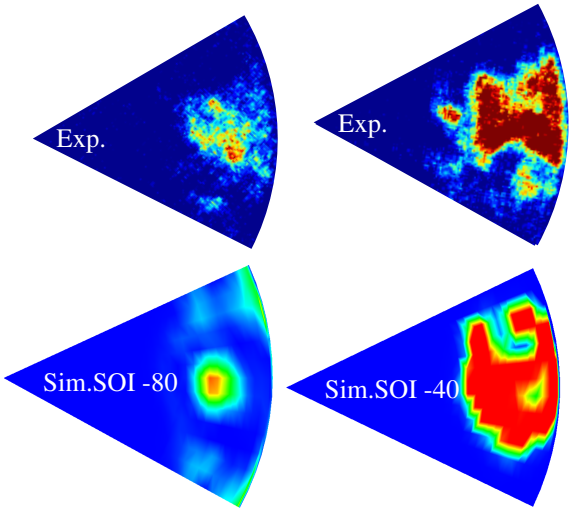

Figure 7.7: *Experimental and numerical OH^* distributions (scalaed to the maximum values for each image) at the sequence of the first stage ignition.*

7.3.5 Effects of Air-Fuel Stratification

Numerical results of AHRR was compared for the considered cases in Fig. 7.8. It can be noted that the time delay between first and second stage ignition was getting shorter by further retarding the start of injection from -80 to -40 CAD ATDC. In other words, it shows that combustion phases faster to the second and main stage heat release in higher air-fuel stratification case. The reason for this behavior will be discussed in flame structure, mixture fraction-temerature, diagrams.

Although it was not for the PPCI combustion, the behavior of inclination toward single stage ignition was also reported by Pei et al. [219] for highly stratified air-fuel charges, Spray A experiments [168], where almost no effects of double stage ignition and negative temperature coefficient region was observed in the numerical simulations. In PPCI combustion, observed differences of combustion phasing speeds toward second stage heat release can be considered as a key parameter to provide a better control on timing of the second stage heat release rate. Hence, the important task then would be generating a desired mixture stratification for different engine operating conditions.

Although Z is a conserved scalar, its higher magnitudes represents the air-fuel mixture strength. In the stratified mixtures availability of Z_{St}, due to its highest chemical reactivity, can alter the ignition and combustion phasing. In case of PPCI combustion,

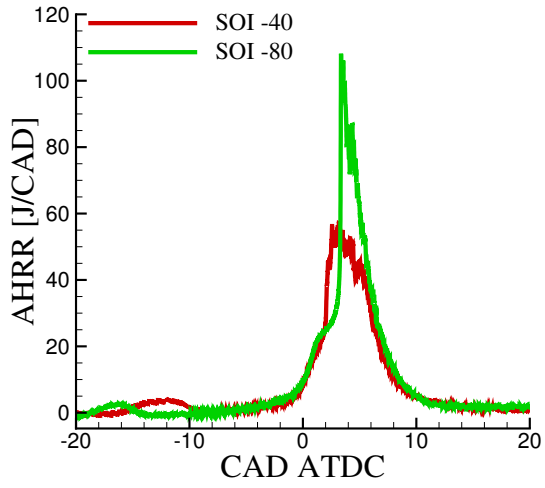

Figure 7.8: *AHRR comparison of SOI -80 and -40 as representators of low and high mixture stratification levels, respectively.*

flame structure diagrams can provide useful insights on ignition and combustion phasing and how they are correlated to the level of mixture stratification. Simulation results of mixture fraction versus temperature for SOI of -80 and -40 ATDC were shown in Fig.7.9 and Fig.7.10, respectively. Initially, it should be noted that there are range of mixture fractions (similar to a line) with temperature about 640K for SOI -80 and 700K for SOI -40 in Fig.7.9 and Fig.7.10. These mixture fractions are the fuel trapped in the piston crevice volume that will not participate in the combustion and discussions below do not take these mixture fraction into account. Moreover, temperature difference of these trapped mixture fractions in the crevice volume of the cases is due to the minor differences of the intake air temperature as stated in Table 7.3 for different injection timings.

For crank angle -20 ATDC, it can be seen that mixture fraction (not the ones in the crevice volume) in the low stratification case of SOI -80 (Fig.7.9) spans a narrower range compared to the high stratification case of SOI -40 (Fig.7.10). This is because of a very early injection in SOI -80, air and fuel had enough time to mix and form lean mixtures. For all shown engine times of SOI -80, mixture fractions are lower than Z_{St}=0.0558.

SOI -80: At early crank angles, it can be seen that compared to SOI -40, having more time for mixing, has caused a large amount of mixture fractions to have very similar temperature (around 750K). Relatively wide range of mixture fractions (from 0 to

0.035) simultaneously ignite and increase the temperature up to about 800K-900K as for first stage ignition around -16 CAD ATDC. Interestingly this occurs earlier for SOI -80 compared to SOI -40. Second stage ignition is around 5 CAD ATDC where temperature of the richer mixture fractions ($Z \approx 0.035$) suddenly elevates to above 2000K. And then reaction zone also spreads for leaner mixture fractions at the later engine times. It implies that engine time needed from first to second stage ignition is 21 engine crank angles for the case of SOI -80.

SOI -40: It can be seen both in Fig.7.10 and Fig.7.8 that first stage ignition for SOI -40 occurs later than SOI -80 around -12 CAD ATDC. The reason for this can be attributed to the retarded injection timing of SOI -40 where cooling due to evaporation affects SOI -40 more than than SOI -80. As mentioned, the range of ignitable mixture fractions before ignition for SOI -40 is almost double the value in SOI -80 due to lowered premixing. This has created mixtures richer than Z_{St}=0.0558 which will result in higher reaction rates if the needed activation energy can be provided by compression.

After the first stage ignition, availability of these richer mixture fractions with higher reactivity, as it was also mentioned in the discussion of the Fig.7.8, noticeably shortens the time from first stage to second stage ignition. This is also shown in Fig.7.11 for CH_2O mass fractions at 5 CAD ATDC as indicator for second stage ignition. It can be seen that due to availability of richer mixture fractions, higher CH_2O is resulted for SOI -40 which shortens the transition time from first stage to second stage ignition. It represents that engine time needed from first to second stage ignition is 17 engine crank angles for the case of SOI -40. This is an important outcome of applying stratified air-fuel charges bringing in additional and effective controlling parameter which is not available in the HCCI engines.

On the other hand, for SOI -80 a large number of mixture fractions at $Z \approx 0.03$ have higher CH_2O mass fractions than SOI -40. This is because larger amount of fuel undergo the second stage ignition in SOI -80 which can be seen in the mixture fraction contours of Fig.7.12. This also causes a higher heat release rate peak in Fig.7.8 for SOI -80.

Explained second stage ignition characteristics of the cases can also shown in the temperature and mixture fraction contours in Fig.7.12.

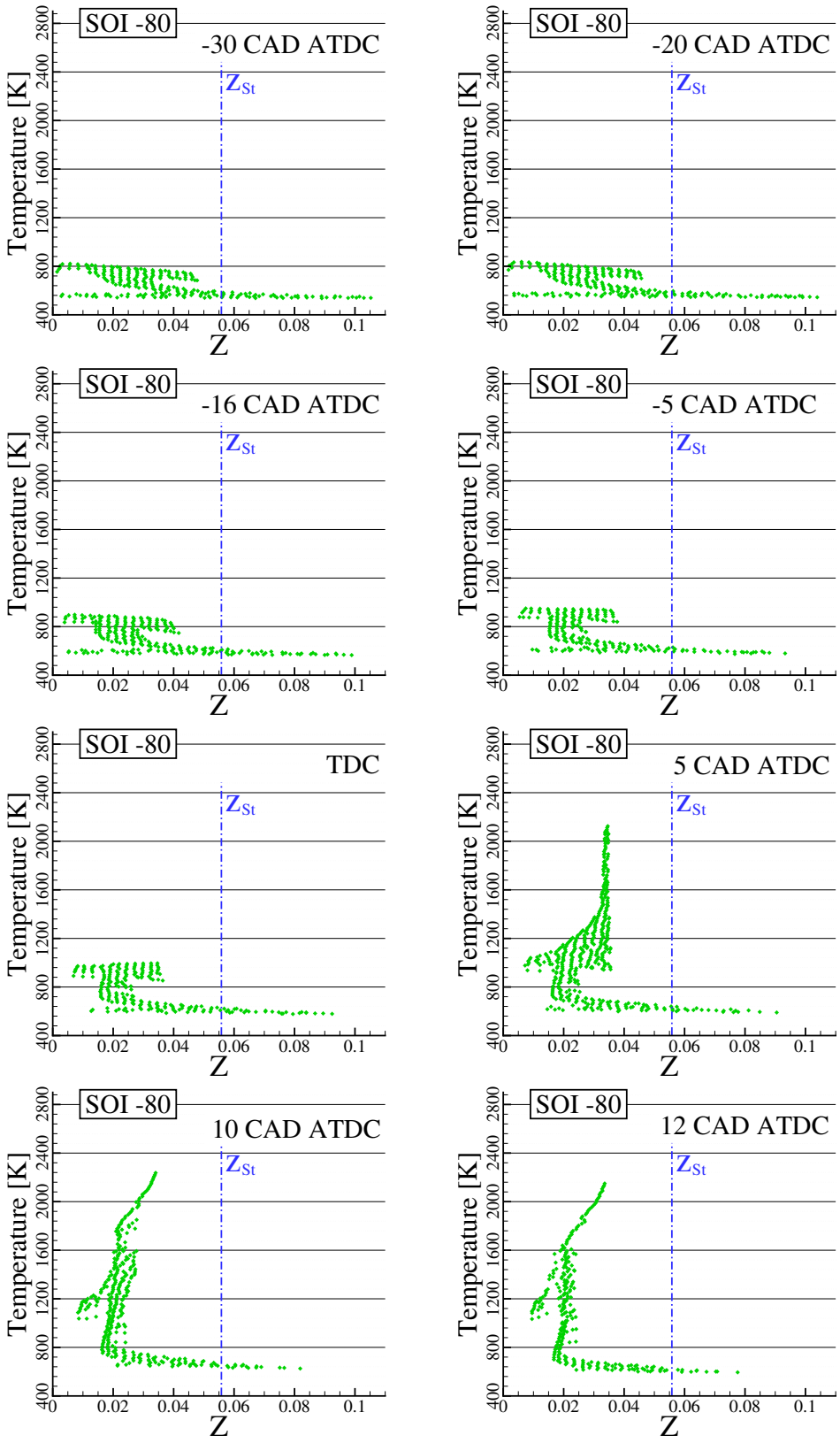

Figure 7.9: *Z-T diagram of flame structure for the low air-fuel mixture stratification case of SOI -80 for shown engine times.* Z_{St}*=0.0558.*

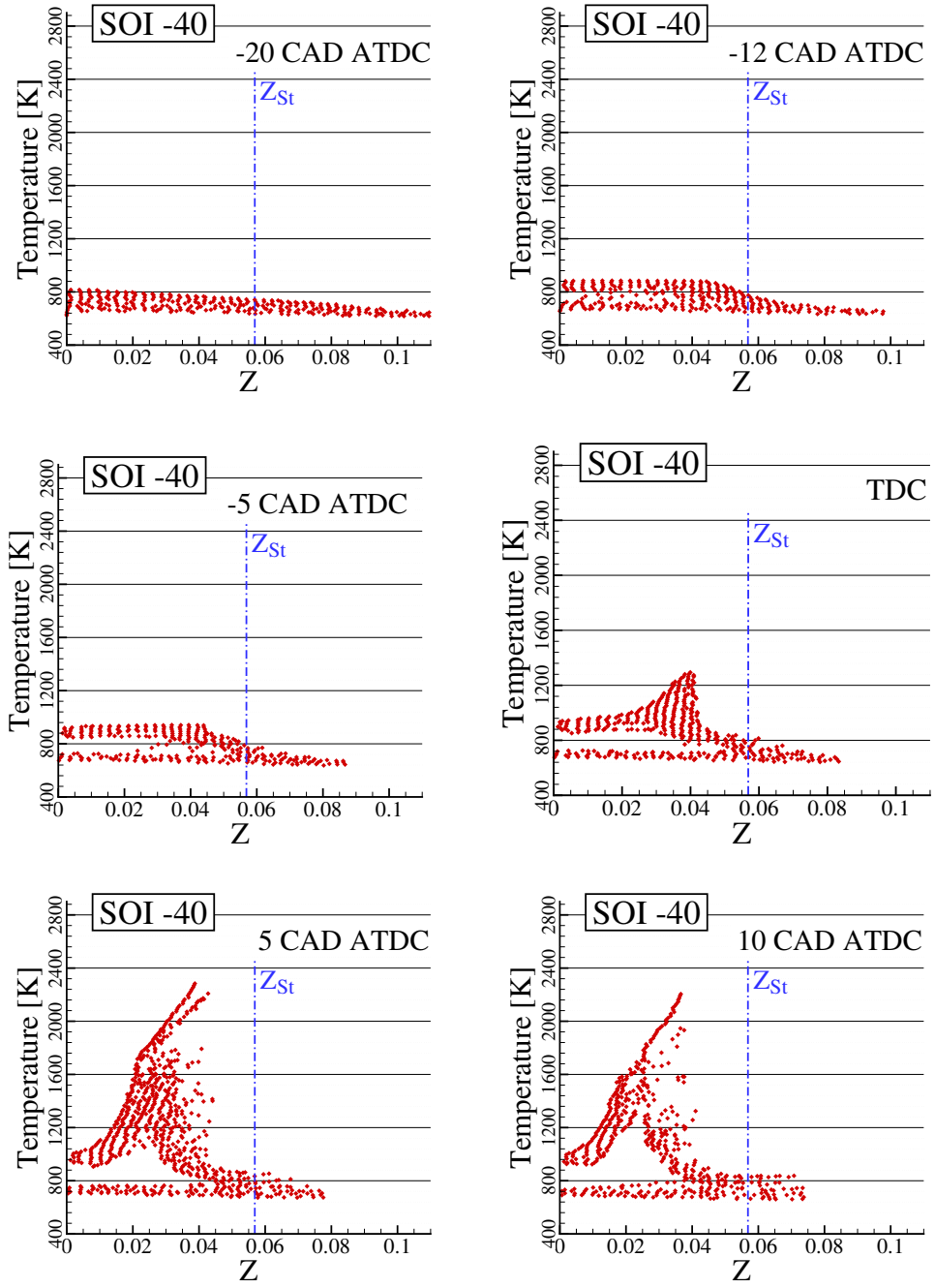

Figure 7.10: *Z-T diagram of flame structure for the high air-fuel mixture stratification case of SOI -40 for shown engine times.* Z_{St}*=0.0558.*

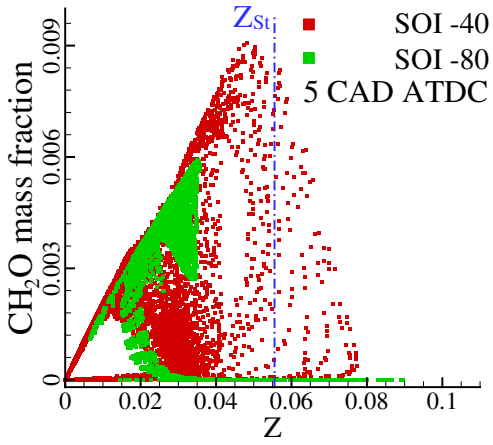

Figure 7.11: *CH_2O mass fractions of SOI -80 and SOI -40 for the whole CFD domain at 5 CAD ATDC (Second stage ignition).*

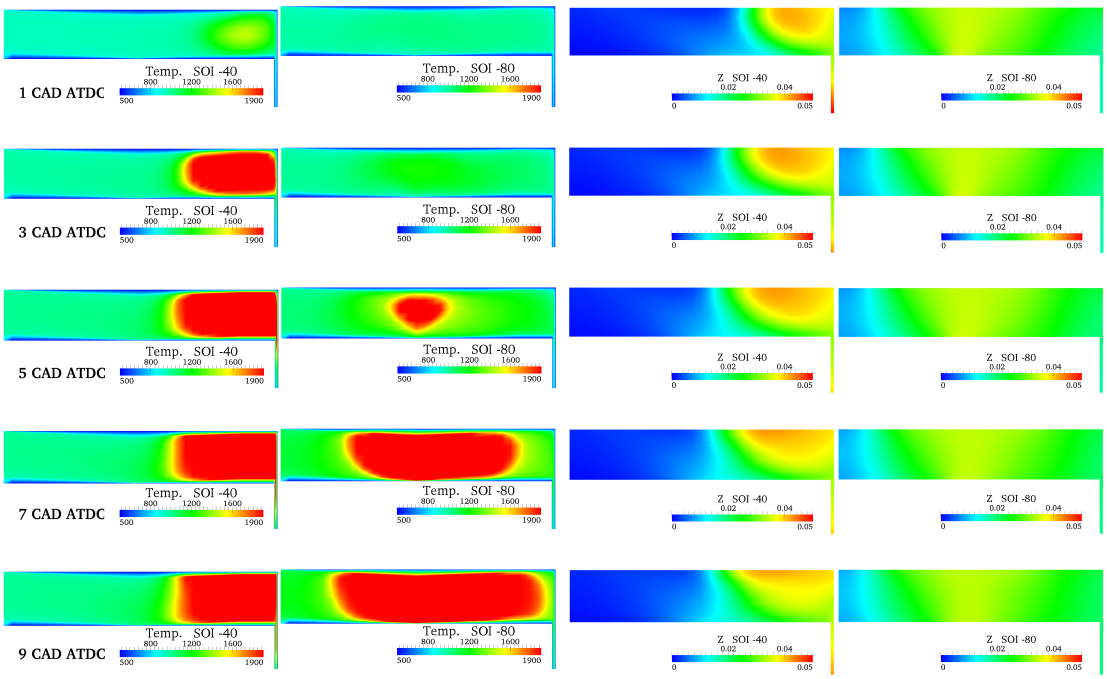

Figure 7.12: *Temperature and mixture fraction contours of SOI -40 and SOI -80 at 1, 3, 5, 7, and 9 CAD ATDC*

In Fig.7.12 a high temperature spot is formed in SOI -40 at 1 CAD ATDC, whereas the temperature contour for the SOI -80 is almost uniform around 1000K after first ignition stage. The reason for earlier formation of this hot spot in SOI -40 can be discussed by locally richer mixture fraction of this region in Fig.7.12 and higher reactivity of these rich mixture fractions which increases the combustion phasing speed for SOI -40. It can also be seen from the mixture fraction contours that due to spray angle and early injection, evaporated fuel in SOI -80 had more time to mix and diffuse to the combustion chamber than SOI -40 creating larger amount of ignitable fuel. As discussed. this was the main reason on higher AHRR peak and CH_2O mass fractions for SOI -80 at second stage ignition.

7.4 Conclusions

At first, HCCI engine simulations were performed to make a transition to the PPCI combustion as the main goal of this Chapter. PPCI engine experiments and simulations of the LTC concept were then performed on a CI optical engine. Two cases of the low and high air-fuel mixture stratification levels were considered. Low and high air-fuel stratification levels were experimentally achieved by early (SOI -80 ATDC) and late (SOI -40 ATDC) injection timings. Experimental results show that injection around -80 CAD has less ignition sensitivity to SOI compared to injection around -40 CAD because of lower level of stratification which was confirmed by analysis of OH^* images. Numerical validation studies of the PPCI engine was then performed for the considered cases. Well-Mixed combustion model is used as PPCI combustion occurs in nearly homogeneous mixtures. After getting acceptable results for in-cylinder pressure, and local distribution of OH^* within the combustion chamber of the PPCI engine, attention was given to evolution of the first and second stage ignitions and combustion phasing speed. Firstly, it was found that with the assumption of similar timing for the second stage ignition provided by intake air heating, first stage ignition occurs earlier for lower air-fuel stratification case. Secondly, high air-fuel stratification will cause in faster shift from the first stage ignition to second stage ignition of the PRF70 fuel. This was discussed to be due to higher reactivity of the mixture in high air-fuel stratification case. Combustion phasing from first to second stage ignition took 21 CAD for SOI -80, whereas for SOI -40 this was 17 CAD. It was concluded that by generating more stratified mixtures and providing needed activation energy by engine thermal load, it would

possible to have control on timing of the second stage ignition and combustion phasing speed of a PPCI engine. This study only considered low and high air-fuel stratification levels and more extensive engine experiments and simulations are needed to define a map of a PPCI engine based on injection timing (air-fuel stratification), engine IMEP or emissions, and engine operating conditions. This was considered as a future research.

CHAPTER 8

Final Conclusions and Future Work

8.1 Summary of the Conclusions

It was discussed in the introduction that Diesel combustion still is going to have a role in transportation and power generation units due to its practical significance and superior fuel consumption aspects. In this light, modeling tasks of Diesel combustion is also ongoing research worldwide. This is due to the nature of Diesel combustion that involves many thermo-physical phenomena and there is a need to enhance a large number of sub-models. Although simplified numerical studies can be conducted in constant volume vessels such as ECN Spray A, real engine environment adds in additional difficulties and more interfering phenomena which cannot be neglected such as swirling and squishing flows of the chamber, handling boundary conditions of fixed and moving walls, complex heat transfer, spray and flame interactions with the piston wall, and etc.

This thesis is among the first attempts in case of *combustion phasing analysis* of the Spray A configuration, *real engine* simulation of the Spray B configuration with wide range of experimental validation, and detailed mathematical and physical reasoning of the *model-to-model* differences in case of applying or neglecting contribution of the

sub-grid scale turbulent mixing (Turbulence Chemistry Interactions) in non/partially-premixed turbulent combustion.

Followings are the principal findings of this thesis for the research on reactive high pressure liquid sprays:

- Identification and parametrization of the conceptual Diesel combustion phases is a perquisite of any fundamental study under non/partially premixed turbulent combustion of reacting sprays. This was discussed that the key elements of Diesel combustion: *Ignition Delay* and *Length of Flame Lift-off* are characteristics of *Premixed Combustion* and *Diffusive Combustion* phases, respectively. It is found that pressure rise rate and apparent heat release rate can be used as a global parameters both in the experiments and in the numerical simulation to identify ignition and separate phases of the Diesel combustion. This will help to comprehensively explain transient Diesel spray flame from the sequence of start of liquid fuel injection till the time for established diffusive flame. Conceptual representation of the ignition and combustion of non/partially-premixed turbulent combustion of the reacting sprays by Peters [25] were shown as the numerical results in the combustion phasing analysis of the Chapter 5. It was concluded that there is a shift of reaction zone from leaner mixture fractions (Z_{MR}, so-called Most Reactive mixture fraction) of the *baseline* Spray A conditions in the Diesel spray periphery to the rich mixture fractions in the tip of the spray. This will generate initial rise in the pressure rise rate diagram. Pressure rise rate then reduces as reaction zone burns the premixed fuel which is prepared during the ignition delay time but then again increases as combustion phases from the premixed to the diffusive combustion. It will then plateaus once the diffusive flame is fully established and progress of the combustion is then depends on mixing of fuel and oxidizer. In such a condition, as stoichiometric mixture fraction is already ignited, reactive zone then proceeds in high temperature diffusive combustion manner. This is the place TCI plays a significant role and the models that neglect TCI, are generally unable to provide acceptable predictions for the heat release rate and flame structure and lift-off.

- Ignition of the liquid reactive sprays is the matter of intense research and still a lot needed to be done as there is a complex interplay of turbulence, spray evaporation, and chemistry pathways for the ignition to occur. Under non/partially-premixed turbulent combustion, ignition starts from the Z_{MR} which by definition does not

affected by turbulence but by air and fuel temperatures and their oxidation activation energy. It is found that although this characteristics holds for the Z_{MR}, the path to ignite the Z_{MR} depends on sub-grid scale turbulent mixing. First observation for this finding is discussed in the comparative combustion model results of ECN Spray A and Spray B configurations in Chapter 5 and Chapter 6, respectively. It has been represented that for all operating conditions which generated by varying the ambient temperature, density, oxidizer level, and injection pressure, including TCI will result in earlier ignition compared to the well-mixed model. To make mathematical comparisons between models with and without TCI there is a need to transform the coordinated to one frame of reference and discuss the model formulation differences there. In order to this, well-mixed model is transformed from spatial coordinates (Cartesian *x, y, and z*-t) to the mixture fraction frame of reference (*Z*-t) and it has been shown that corresponding scalar dissipation rate value for the well-mixed model is $\chi = 2\frac{\mu_t}{Sc\widetilde{Z''^2}}\left|\nabla Z\right|^2$ which is formulated in species mass fraction transport equation. Compared to the χ value as determined in $\chi = C_\chi \frac{\varepsilon}{k}\widetilde{Z''^2}$ and used by the MRIF model, this is expected to have a different evolution during the injection and immediately after its finishing. Embedded TCI in MRIF model in reaction space more rapidly reduces the scalar dissipation rate below the extinction values and enables local ignitions in very lean mixture fractions, but in flammability limits, in jet periphery and small heat release of this local ignition will result in flow dilatation. It has been shown that due to flow dilatation effect, transport of mixture fraction will be altered. It was shown that mixture fraction field in the MRIF model with embedded TCI effects was more smoothed or had locally lower variances compared to the transport of mixture fraction in the well-mixed model. All these were happening even before premixed rise of mean PRR and this is why ignition of the Z_{MR} is implicitly rely on turbulence and sub-grid scale turbulent mixing.

- It has been found that in the case of combustion phasing from the sequence of the ignition to the fully established diffusive flame, TCI again plays a significant role. Model-to-model comparisons with including or neglecting TCI showed that once the main ignition is triggered and mean PRR is undergone the premixed phase rise, well-mixed model (without TCI) tends to have faster speeds to reach thermodynamic equilibrium than MRIF model (with TCI). Ignited mixture fractions in the

well-mixed model were experiencing higher chemistry rates than the MRIF. This has been caused in faster transition of the ignition to the diffusive phase of Diesel combustion in the well-mixed model. In other words, TCI of the MRIF model promotes the conditions for initiation of the main ignition resulting in lower ignition delay times, however, it limits the reaction rates and the temperature rise after the main ignition and decelerates the speed of combustion phasing.

- It has been also represented that apart from physical models such as for turbulent mixing and its interactions with chemical time scales, reaction rates determined from the chemical kinetics mechanisms will alter the results for ignition delay time and flame lift-off. It has been shown that the choice of chemical kinetics mechanism can alter the sequence of ignition, combustion phasing, and reactive flame brush of the spray flames. This is showing that due to application of different methodologies to reduce the mechanisms from a detailed reaction mechanism, large dependencies can be created if later these reduced reaction mechanisms wanted to be applied in CFD simulations. In case of Spray A and Spray B configurations, there is a need to develop and validate reaction mechanisms in higher validity range of temperature and equivalence ratio and more importantly in elevated pressures similar to IC engine applications.

- In the last part of the thesis attention was given to the HCCI and PPCI engine simulations of the low temperature combustion concepts. It was highlighted that HCCI combustion is difficult to control due to very intense pressure rise and heat release rate. PPCI combustion can be more applicable in terms of controllability and working under wide range of engine operating conditions. It was shown in the numerical results that by getting more stratified mixtures, PPCI combustion can results in lower heat release rates and more favorable combustion where a wide range of air-fuel stratification was achieved by different start of injection timings. Comparing to the conventional Diesel combustion, there was no stoichiometric mixture fractions in the combustion chamber at time of first or second stage ignitions. This would reduce the combustion peak temperature. However, it was found that having larger range of lean mixture fractions in highly stratified air-fuel chargers will reduce the PRR and heat release rate comparing to the lowered stratified conditions. On the other hand, the amount of stratified mixture which is prepared during the ignition delay can play a significant role on rate of heat release

and peak pressure. It was also found that by further getting closer to mixtures with higher air-fuel stratification levels, the time between first and second stage heat release shortens. This can also be accounted as a practical control parameter for the PPCI engine optimization perspectives.

8.2 Future Work

Research on non/partially-premixed spray flames can be directed in many different aspects and some of them are listed as future work below.

- It would be worth study to see the speed of combustion phasing, starting from a value of mixture fraction and stabilizing on stoichiometric mixture fraction, and shifting of the reaction zone in mixture fraction space using the DNS studies and then compare this shifting speed to the model with/without considering TCI. This also can be resulted in very useful insights in the case of model development and enhancing the way turbulent mixing interacts with chemistry.

- Unlike gaseous non-premixed combustion, liquid fuel non-premixed combustion needs further research on the effect of droplet size reduction and heat reduction due to evaporation. Cooling effect due to evaporation needed to be considered in mixture fraction and its variance transport. Many studies tried to include these effects in physical and reaction spaces of the flamelet models such as RIF. Still there is demand to more comprehensive closures due to evaporation and liquid particle or ligament diameter reduction effects on mixture fraction, its variance, and scalar dissipation rate and subsequently on combustion.

- Although introduced TCI effects in the MRIF model has been resulted in large enhancements of ignition and flame lift-off results, scalar dissipation rate introduced by RIF model does not have an ultimate formulation for transient Diesel spray combustion. Despite the fact that β-PDF can give better statistical representation of the effect of scalar dissipation rate, its definition in the RIF model considered to be uniform throughout the whole flame and no conditional and fluctuating characteristics were applied. Conditional Moment Closure [220–222] or Multiple Mapping Conditioning [223–225] methods can be very good mathematical framework to take into account effects of conditional variables in turbulent non-premixed combustion modeling studies.

- Engine optimization and control based studies and needed acceleration of the simulation time can be considered a very important motive factor for the ongoing research. Large number of chemical species and reactions in the chemical kinetics mechanisms and their integration in system of stiff ODE are still resulting in massive computational power/time over head. Application of the different tabulation method such as FGM [112] and ILDM [117] to tabulate the chemical kinetics output and later link it to CFD through definition of *progress variable* is foreseeable future for IC engine computational studies. However, still large amount of research is going on in this area as application of progress variable approach for non/partially-premixed combustion needs further comprehensive study. The main advantage of these methods is significantly reducing the engine simulation times.

- In case of Low Temperature Combustion of the PPCI engine, it is highly needed to perform very accurate experiments with very good control over engine initial and boundary conditions. This is because LTC modes are very sensitive to the engine thermal load and injection strategies. Liquid wall film formation and trapped fuel mass in the piston crevice volume should be highly avoided to make comparable set of data. In case of numerical simulations, selection of the combustion model for these operating conditions is the matter of debate. This is because PPCI combustion in case of mixture strength and ranges of scalar dissipation rate is somewhere between Diesel and HCCI modes.

List of Acronyms

AHRR	Apparent Heat Release Rate	ATDC	After Top Dead Center
BDC	Bottom Dead Center	CAD	Crank Angle Degree
CFD	Computational Fluid Dynamics	DNS	Direct Numerical Simulation
DOI	Duration of Injection	ECN	Engine Combustion Network
EGR	Exhaust Gas Re-circulation	GDI	Gasoline Direct Injection
HCCI	Homogeneous Charge Compression Ignition	HRR	Heat Release Rate
IC	Internal Combustion	LDEF	Lagrangian Droplet Eulerian Flow
LES	Large Eddy Simulation	LOL	Lift-off Length
LTC	Low Temperature Combustion	MRIF	Multiple Representative Interactive Flamelet
MZWM	Multi-Zone Well Mixed	NO_x	Oxides of Nitrogen
PM	Particulate Matter	PPCI	Partially Premixed Compression Ignition
PRF	Primary Reference Fuel	PRR	Pressure Rise Rate
RANS	Reynolds Averaged Navier Stokes	RCCI	Reactivity Controlled Compression Ignition
SOI	Start of Injection	SOC	Start of Combustion
TDC	Top Dead Center	TCI	Turbulence Chemistry Interactions
WM	Well Mixed	UHC	Unburnt Hydro-Carbons

Bibliography

[1] Rolf D Reitz. Directions in internal combustion engine research. *Combustion and Flame*, 1(160):1–8, 2013.

[2] H An, WM Yang, A Maghbouli, J Li, SK Chou, and KJ Chua. Performance, combustion and emission characteristics of biodiesel derived from waste cooking oils. *Applied energy*, 112:493–499, 2013.

[3] WM Yang, H An, SK Chou, KJ Chua, B Mohan, V Sivasankaralingam, V Raman, A Maghbouli, and J Li. Impact of emulsion fuel with nano-organic additives on the performance of diesel engine. *Applied energy*, 112:1206–1212, 2013.

[4] Magdi Khair and Dale L McKinnon. Performance evaluation of advanced emission control technologies for diesel heavy-duty engines. Technical report, SAE technical paper, 1999.

[5] John E Dec and Robert E Canaan. Plif imaging of no formation in a di diesel engine. Technical report, SAE Technical Paper, 1998.

[6] Z-M Cao, Koichi Nishino, S Mizuno, and K Torii. Piv measurement of internal structure of diesel fuel spray. *Experiments in fluids*, 29(1):S211–S219, 2000.

[7] Julien Lacoste, Cyril Crua, Morgan Heikal, Dave Kennaird, and Martin Gold. Pda characterisation of dense diesel sprays using a common-rail injection system. Technical report, SAE Technical Paper, 2003.

[8] R Minetti, M Carlier, M Ribaucour, E Therssen, and LR Sochet. A rapid compression machine investigation of oxidation and auto-ignition of n-heptane: measurements and modeling. *Combustion and Flame*, 102(3):298–309, 1995.

[9] Mark A Patterson and Rolf D Reitz. Modeling the effects of fuel spray characteristics on diesel engine combustion and emission. Technical report, SAE Technical Paper, 1998.

[10] W Ethan Eagle, Louis-Marie Malbec, and Mark PB Musculus. Measurements of liquid length, vapor penetration, ignition delay, and flame lift-off length for the engine combustion network "spray b" in a 2.34 l heavy-duty optical diesel engine. *SAE International Journal of Engines*, 9(2016-01-0743):910–931, 2016.

[11] Seref Soylu. Examination of combustion characteristics and phasing strategies of a natural gas hcci engine. *Energy conversion and management*, 46(1):101–119, 2005.

[12] Scott B Fiveland and Dennis N Assanis. Development and validation of a quasi-dimensional model for hcci engine performance and emissions studies under turbocharged conditions. Technical report, SAE Technical paper, 2002.

[13] NP Komninos, DT Hountalas, and DA Kouremenos. Development of a new multi-zone model for the description of physical processes in hcci engines. Technical report, SAE Technical Paper, 2004.

[14] T. Poinsot and D. Veynante. *Theoretical and Numerical Combustion*. Edwards, 2005.

[15] Sandia Engine Combustion Network Database. http://www.ca.sandia.gov/ecn, 2015.

[16] Mark PB Musculus, Paul C Miles, and Lyle M Pickett. Conceptual models for partially premixed low-temperature diesel combustion. *Progress in Energy and Combustion Science*, 39(2):246–283, 2013.

[17] Mark PB Musculus. Multiple simultaneous optical diagnostic imaging of early-injection low-temperature combustion in a heavy-duty diesel engine. Technical report, SAE Technical Paper, 2006.

[18] H.G. Weller, G. Tabor, H. Jasak, and C. Fureby. A Tensorial Approach to CFD using Object Orientated Techniques. *Computers in Physics*, Vol. 12(No. 6):620, 1998.

[19] T. Lucchini, G. D'Errico, F. Brusiani, and G. Bianchi. A Finite-Element Based Mesh Motion Technique for Internal Combustion Engine Simulations. *COMODIA 2008*, MS2-3, 2008.

[20] G. Montenegro, A. Onorati, F. Piscaglia, and G. D'Errico. Integrated 1d-multid fluid dynamic models for the simulation of ice intake and exhaust systems. *SAE Paper*, 2007-01-0495, 2007.

[21] Gareth Williams. *Combustion theory*. Citeseer, 1985.

[22] Kenneth K Kuo. *Principles of combustion*. Wiley New York et al., 1986.

[23] Stephen B Pope. Turbulent flows, 2001.

[24] Henk Kaarle Versteeg and Weeratunge Malalasekera. *An introduction to computational fluid dynamics: the finite volume method*. Pearson Education, 2007.

[25] N. Peters. *Turbulent Combustion*. Cambridge University Press, 2000.

[26] Mouldi Chrigui, James Gounder, Amsini Sadiki, Assaad R Masri, and Johannes Janicka. Partially premixed reacting acetone spray using les and fgm tabulated chemistry. *Combustion and flame*, 159(8):2718–2741, 2012.

[27] Yuanjiang Pei, Bing Hu, and Sibendu Som. Large-eddy simulation of an n-dodecane spray flame under different ambient oxygen conditions. *Journal of Energy Resources Technology*, 138(3):032205, 2016.

[28] Ville Vuorinen et al. Les of certain droplet size effects in fuel sprays. *Aalto-yliopiston teknillinen korkeakoulu*, 2010.

[29] Song-Charng Kong, Craig D Marriott, Rolf D Reitz, and Magnus Christensen. Modeling and experiments of hcci engine combustion using detailed chemical kinetics with multidimensional cfd. Technical report, SAE Technical paper, 2001.

[30] Sangjin Hong, Margaret S Wooldridge, Hong G Im, Dennis N Assanis, and Heinz Pitsch. Development and application of a comprehensive soot model for 3d cfd reacting flow studies in a diesel engine. *Combustion and Flame*, 143(1):11–26, 2005.

[31] F Payri, J Benajes, X Margot, and A Gil. Cfd modeling of the in-cylinder flow in direct-injection diesel engines. *Computers & fluids*, 33(8):995–1021, 2004.

[32] Amin Maghbouli, Rahim Khoshbakhti Saray, Sina Shafee, and Jafar Ghafouri. Numerical study of combustion and emission characteristics of dual-fuel engines using 3d-cfd models coupled with chemical kinetics. *Fuel*, 106:98–105, 2013.

[33] Amin Maghbouli, Wenming Yang, Hui An, Jing Li, Siaw Kiang Chou, and Kian Jon Chua. An advanced combustion model coupled with detailed chemical reaction mechanism for di diesel engine simulation. *Applied energy*, 111:758–770, 2013.

[34] Amin Maghbouli, Sina Shafee, Rahim Khoshbakhti Saray, Wenming Yang, Vahid Hosseini, and Hui An. A multi-dimensional cfd-chemical kinetics approach in detection and reduction of knocking combustion in diesel-natural gas dual-fuel engines using local heat release analysis. *SAE International Journal of Engines*, 6(2013-01-0865):777–787, 2013.

[35] Amin Maghbouli, Tommaso Lucchini, Gianluca D'Errico, Angelo Onorati, Louis-Marie Malbec, Mark PB Musculus, and W Ethan Eagle. Parametric comparison of well-mixed and flamelet n-dodecane spray combustion with engine experiments at well controlled boundary conditions. Technical report, SAE Technical Paper, 2016.

[36] Hendrik Tennekes and John Leask Lumley. *A first course in turbulence*. MIT press, 1972.

[37] Günter Merker, Christian Schwarz, Gunnar Stiesch, and Frank Otto. *Simulating combustion: simulation of combustion and pollutant formation for engine-development*. Springer Science & Business Media, 2005.

[38] R. Torelli. *Novel approaches for CFD modeling of Diesel engines* . PhD thesis, Politecnico di Milano, 2015.

[39] Alan Williams. *Combustion of liquid fuel sprays*. Butterworth-Heinemann, 2013.

[40] AG Gerber and MJ Kermani. A pressure based eulerian–eulerian multi-phase model for non-equilibrium condensation in transonic steam flow. *International Journal of Heat and Mass Transfer*, 47(10):2217–2231, 2004.

[41] AA Mostafa and HC Mongia. On the modeling of turbulent evaporating sprays: Eulerian versus lagrangian approach. *International Journal of Heat and Mass Transfer*, 30(12):2583–2593, 1987.

[42] T. Lucchini, G. D'Errico, and D. Ettorre. Numerical investigation of the spray-mesh-turbulence interactions for high-pressure, evaporating sprays at engine conditions. *International Journal of Heat and Fluid Flow*, 32:pp. 285–297, 2011.

[43] S Singh, RD Reitz, MPB Musculus, and T Lachaux. Validation of engine combustion models against detailed in-cylinder optical diagnostics data for a heavy-duty compression-ignition engine. *International Journal of Engine Research*, 8(1):97–126, 2007.

[44] A. Maghbouli, T. Lucchini, G. D'Errico, and A. Onorati. Effects of grid alignment on modeling the spray and mixing process in direct injection diesel engines under non-reacting operating conditions. *Applied Thermal Engineering*, 91:pp. 901–912, 2015.

[45] R. D. Reitz. *Computer modeling of sprays. Spray Technology short course*. Uni WM, Pittsburgh, PA, May 7 1996.

[46] Fikret Yüksel and Bedri Yüksel. The use of ethanol–gasoline blend as a fuel in an si engine. *Renewable energy*, 29(7):1181–1191, 2004.

[47] Frank M Bowman and John H Seinfeld. Atmospheric chemistry of alternate fuels and reformulated gasoline components. *Progress in energy and combustion science*, 21(5):387–417, 1995.

[48] Eva Garcia, Miriam Laca, Elena Pérez, Angel Garrido, and Julián Peinado. New class of acetal derived from glycerin as a biodiesel fuel component. *Energy & fuels*, 22(6):4274–4280, 2008.

[49] Gerhard Knothe and Kevin R Steidley. Kinematic viscosity of biodiesel fuel components and related compounds. influence of compound structure and comparison to petrodiesel fuel components. *Fuel*, 84(9):1059–1065, 2005.

[50] A Bader, P Keller, and C Hasse. The influence of non-ideal vapor-liquid equilibrium on the evaporation of ethanol/iso-octane droplets. *International Journal of Heat and Mass Transfer*, 64:547–558, 2013.

[51] A Bader, P Keller, C Hasse, and B Meyer. The influence of non-ideal vapor-liquid-equilibrium on vaporization of multicomponent hydrocarbon fuels. *ICLASS 2012, 12th Triennial International Conference on Liquid Atomization and Spray Systems, Heidelberg, Germany, September 2-6*, 2012.

[52] Yuri M Wright, Ourania-Nektaria Margari, Konstantinos Boulouchos, Giorgio De Paola, and Epaminondas Mastorakos. Experiments and simulations of n-heptane spray auto-ignition in a closed combustion chamber at diesel engine conditions. *Flow, turbulence and combustion*, 84(1):49–78, 2010.

[53] Valeri I Golovitchev, N Nordin, R Jarnicki, and J Chomiak. 3-d diesel spray simulations using a new detailed chemistry turbulent combustion model. Technical report, SAE Technical Paper, 2000.

[54] Henry J Curran, Paolo Gaffuri, William J Pitz, and Charles K Westbrook. A comprehensive modeling study of n-heptane oxidation. *Combustion and flame*, 114(1):149–177, 1998.

[55] H Barths, H Pitsch, and N Peters. 3d simulation of di diesel combustion and pollutant formation using a two-component reference fuel. *Oil & Gas science and technology*, 54(2):233–244, 1999.

[56] Quan-De Wang, Jing-Bo Wang, Juan-Qin Li, Ning-Xin Tan, and Xiang-Yuan Li. Reactive molecular dynamics simulation and chemical kinetic modeling of pyrolysis and combustion of n-dodecane. *Combustion and Flame*, 158(2):217–226, 2011.

[57] Subhasish Bhattacharjee and Daniel C Haworth. Simulations of transient n-heptane and n-dodecane spray flames under engine-relevant conditions using a transported pdf method. *Combustion and Flame*, 160:2083–2102, 2013.

[58] S Som, DE Longman, Z Luo, M Plomer, and T Lu. Three dimensional simulations of diesel sprays using n-dodecane as a surrogate. In *Fall technical meeting of the eastern states section of the combustion institute*, 2011.

[59] Olivier Herbinet, Paul-Marie Marquaire, Frédérique Battin-Leclerc, and René Fournet. Thermal decomposition of n-dodecane: Experiments and kinetic modeling. *Journal of analytical and applied pyrolysis*, 78(2):419–429, 2007.

[60] Anthony A Amsden, PJ O'rourke, and TD Butler. Kiva-ii: A computer program for chemically reactive flows with sprays. Technical report, Los Alamos National Lab., NM (USA), 1989.

[61] Dennis N Assanis, Zoran S Filipi, Scott B Fiveland, and Michalis Syrimis. A predictive ignition delay correlation under steady-state and transient operation of a direct injection diesel engine. *Journal of Engineering for Gas Turbines and Power*, 125(2):450–457, 2003.

[62] Seyed Mohammad Mousavi, Rahim Khoshbakhti Saray, Kamran Poorghasemi, and Amin Maghbouli. A numerical investigation on combustion and emission characteristics of a dual fuel engine at part load condition. *Fuel*, 166:309–319, 2016.

[63] Stephen R Turns et al. *An introduction to combustion*, volume 287. McGraw-hill New York, 1996.

[64] James H Espenson. *Chemical kinetics and reaction mechanisms*. McGraw-Hill, 1981.

[65] Sidney William Benson et al. *Foundations of chemical kinetics*. McGraw-Hill, 1960.

[66] Arthur Frost and Ralph Pearson. Kinetics and mechanism. *The Journal of Physical Chemistry*, 65(2):384–384, 1961.

[67] Peter N Brown, George D Byrne, and Alan C Hindmarsh. Vode: A variable-coefficient ode solver. *SIAM journal on scientific and statistical computing*, 10(5):1038–1051, 1989.

[68] Scott D Cohen and Alan C Hindmarsh. Cvode, a stiff/nonstiff ode solver in c. *Computers in physics*, 10(2):138–143, 1996.

[69] Alan C Hindmarsh. Serial fortran solvers for ode initial value problems. *URL: http://www. llnl. gov/-CASC/odepack [cited October 18, 2005]*, 2002.

[70] Roland Borghi. Turbulent combustion modelling. *Progress in Energy and Combustion Science*, 14(4):245–292, 1988.

[71] Frédérique Battin-Leclerc, John M Simmie, and Edward Blurock. *Cleaner combustion*. Springer, 2013.

[72] Max Bodenstein and SC Lind. *Geschwindigkeit der Bildung des Bromwasserstoffs aus seinen Elementen*. Engelmann, 1906.

[73] K Seshadri and N Peters. The inner structure of methane air flames. *Combustion and Flame*, 81(2):96–118, 1990.

[74] LONG Liang, Rolf D Reitz, Claudia O Iyer, and Jianwen Yi. Modeling knock in spark-ignition engines using a g-equation combustion model incorporating detailed chemical kinetics. Technical report, SAE Technical Paper, 2007.

[75] Martin Oberlack, Holger Wenzel, and Norbert Peters. Symmetries and averaging of the g-equation for premixed combustion. In *TSFP DIGITAL LIBRARY ONLINE*. Begel House Inc., 2001.

[76] J Piana, D Veynante, S Candel, and T Poinsot. Direct numerical simulation analysis of the g-equation in premixed combustion. In *Direct and Large-Eddy Simulation II*, pages 321–330. Springer, 1997.

[77] M Boger, D Veynante, H Boughanem, and A Trouve. Direct numerical simulation analysis of flame surface density concept for large eddy simulation of turbulent premixed combustion. In *Symposium (International) on Combustion*, volume 27, pages 917–925. Elsevier, 1998.

[78] ER Hawkes and RS Cant. A flame surface density approach to large-eddy simulation of premixed turbulent combustion. *Proceedings of the Combustion Institute*, 28(1):51–58, 2000.

[79] IG Shepherd. Flame surface density and burning rate in premixed turbulent flames. In *Symposium (International) on Combustion*, volume 26, pages 373–379. Elsevier, 1996.

[80] John E Dec. A conceptual model of di diesel combustion based on laser-sheet imaging. Technical report, SAE technical paper, 1997.

[81] Patrick F Flynn, Russell P Durrett, Gary L Hunter, Axel O zur Loye, OC Akinyemi, John E Dec, and Charles K Westbrook. Diesel combustion: an integrated view combining laser diagnostics, chemical kinetics, and empirical validation. *LLNL*, 1999.

[82] SP Burke and TEW Schumann. Diffusion flames. *Industrial & Engineering Chemistry*, 20(10):998–1004, 1928.

[83] RW Bilger. Turbulent flows with nonpremixed reactants. In *Turbulent reacting flows*, pages 65–113. Springer, 1980.

[84] P Domingo and L Vervisch. Triple flames and partially premixed combustion in autoignition of non-premixed turbulent mixtures. In *Symposium (International) on Combustion*, volume 26, pages 233–240. Elsevier, 1996.

[85] D Martinez-Ruiz, J Urzay, AL Sanchez, A Linan, and FA Williams. Dynamics of thermal ignition of spray flames in mixing layers. *Journal of Fluid Mechanics*, 734:387–423, 2013.

[86] Ruiqin Shan and Tianfeng Lu. Ignition and extinction in perfectly stirred reactors with detailed chemistry. *Combustion and Flame*, 159(6):2069–2076, 2012.

[87] Epaminondas Mastorakos. Ignition of turbulent non-premixed flames. *Progress in Energy and Combustion Science*, 35(1):57–97, 2009.

[88] E Mastorakos, TA Baritaud, and TJ Poinsot. Numerical simulations of autoignition in turbulent mixing flows. *Combustion and Flame*, 109(1):198–223, 1997.

[89] Amable Linan. The asymptotic structure of counterflow diffusion flames for large activation energies. *Acta Astronautica*, 1(7-8):1007–1039, 1974.

[90] PA Lakshminarayanan and Yoghesh V Aghav. *Modelling diesel combustion*. Springer Science & Business Media, 2010.

[91] Dennis L Siebers and Brian Higgins. Flame lift-off on direct-injection diesel sprays under quiescent conditions. Technical report, SAE Technical Paper, 2001.

[92] Nancy J Brown, Kenneth L Revzan, and Michael Frenklach. Detailed kinetic modeling of soot formation in ethylene/air mixtures reacting in a perfectly stirred reactor. In *Symposium (International) on Combustion*, volume 27, pages 1573–1580. Elsevier, 1998.

[93] Mehdi Jangi, Rickard Solsjo, Bengt Johansson, and Xue-Song Bai. On large eddy simulation of diesel spray for internal combustion engines. *International Journal of Heat and Fluid Flow*, 53:68–80, 2015.

[94] Song-Charng Kong, Amar Patel, Qi Yin, Adam Klingbeil, and Rolf D Reitz. Numerical modeling of diesel engine combustion and emissions under hcci-like conditions with high egr levels. Technical report, SAE Technical Paper, 2003.

[95] Caroline L Genzale, Rolf D Reitz, and David D Wickman. A computational investigation into the effects of spray targeting, bowl geometry and swirl ratio for low-temperature combustion in a heavy-duty diesel engine. Technical report, SAE Technical Paper, 2007.

[96] Song-Charng Kong, Yong Sun, and Rolf D Rietz. Modeling diesel spray flame liftoff, sooting tendency, and nox emissions using detailed chemistry with phenomenological soot model. *Journal of Engineering for Gas Turbines and Power*, 129(1):245–251, 2007.

[97] Takaaki Kitamura and Takayuki Ito. Mixing-controlled, low temperature diesel combustion with pressure modulated multiple-injection for hsdi diesel engine. *SAE International Journal of Engines*, 3(2010-01-0609):461–478, 2010.

[98] YZ Zhang, EH Kung, and DC Haworth. A pdf method for multidimensional modeling of hcci engine combustion: effects of turbulence/chemistry interactions on ignition timing and emissions. *Proceedings of the Combustion Institute*, 30(2):2763–2771, 2005.

[99] Heinz Pitsch. Large-eddy simulation of turbulent combustion. *Annu. Rev. Fluid Mech.*, 38:453–482, 2006.

[100] RP Lindstedt and EM Vaos. Transported pdf modeling of high-reynolds-number premixed turbulent flames. *Combustion and Flame*, 145(3):495–511, 2006.

[101] S. Bhattacharjee and D. C. Haworth. Simulations of transient n-heptane and n-dodecane spray flames under engine-relevant conditions using a transported PDF method. *Combustion and Flame*, 160(10):2083–2102, 2013.

[102] M Zhu, KNC Bray, O Rumberg, and B Rogg. Pdf transport equations for two-phase reactive flows and sprays. *Combustion and flame*, 122(3):327–338, 2000.

[103] FX Demoulin and R Borghi. Assumed pdf modeling of turbulent spray combustion. *Combustion science and technology*, 158(1):249–271, 2000.

[104] C Hergart, Hardo Barths, and N Peters. Modeling the combustion in a small-bore diesel engine using a method based on representative interactive flamelets. Technical report, SAE Technical Paper, 1999.

[105] Prithwish Kundu, Yuanjiang Pei, Mingjie Wang, Raju Mandhapati, and Sibendu Som. Evaluation of turbulence-chemistry interaction under diesel engine conditions with multi-flamelet rif model. *Atomization and Sprays*, 24(9), 2014.

[106] Song-Charng Kong, Hoojoong Kim, Rolf D Reitz, and Yongmo Kim. Comparisons of diesel pcci combustion simulations using a representative interactive flamelet model and direct integration of cfd with detailed chemistry. *Journal of Engineering for Gas Turbines and Power*, 129(1):252–260, 2007.

[107] G. D'Errico, T. Lucchini, F. Contino, Mehdi Jangi, , and X-S. Bai. Comparison of well-mixed and multiple representative interactive flamelet approaches for diesel spray combustion modelling. *Combustion Theory and Modelling*, 18, 2014.

[108] Charles D Pierce and Parviz Moin. Progress-variable approach for large-eddy simulation of non-premixed turbulent combustion. *Journal of Fluid Mechanics*, 504:73–97, 2004.

[109] Ken Bray, Pascale Domingo, and Luc Vervisch. Role of the progress variable in models for partially premixed turbulent combustion. *Combustion and Flame*, 141(4):431–437, 2005.

[110] Matthias Ihme, Chong M Cha, and Heinz Pitsch. Prediction of local extinction and re-ignition effects in non-premixed turbulent combustion using a flamelet/progress variable approach. *Proceedings of the Combustion Institute*, 30(1):793–800, 2005.

[111] Matthias Ihme and Yee Chee See. Prediction of autoignition in a lifted methane/air flame using an unsteady flamelet/progress variable model. *Combustion and Flame*, 157(10):1850–1862, 2010.

[112] JA Van Oijen, FA Lammers, and LPH De Goey. Modeling of complex premixed burner systems by using flamelet-generated manifolds. *Combustion and Flame*, 127(3):2124–2134, 2001.

[113] Cemil Bekdemir, Bart Somers, and Philip de Goey. Dns with detailed and tabulated chemistry of engine relevant igniting systems. *Combustion and Flame*, 161(1):210–221, 2014.

[114] Cemil Bekdemir, Erik Rijk, Bart Somers, Philip de Goey, and Bogdan Albrecht. On the application of the flamelet generated manifold (fgm) approach to the simulation of an igniting diesel spray. Technical report, SAE Technical Paper, 2010.

[115] Charles David Pierce. *Progress-variable approach for large-eddy simulation of turbulent combustion*. PhD thesis, Citeseer, 2001.

[116] Matthias Ihme, Lee Shunn, and Jian Zhang. Regularization of reaction progress variable for application to flamelet-based combustion models. *Journal of Computational Physics*, 231(23):7715–7721, 2012.

[117] Benoit Fiorina, Romain Baron, Olivier Gicquel, D Thevenin, Stéphane Carpentier, Nasser Darabiha, et al. Modelling non-adiabatic partially premixed flames using flame-prolongation of ildm. *Combustion Theory and Modelling*, 7(3):449–470, 2003.

[118] Vincent Fichet. *Modélisation de la combustion du gaz naturel par réseaux de réacteurs avec cinétique chimique détaillée*. PhD thesis, Ecole Centrale Paris, 2008.

[119] X. Yang, A. Solomon, and T. Kuo. Ignition and Combustion Simulations of Spray-Guided SIDI Engine using Arrhenius Combustion with Spark-Energy Deposition Model. *SAE Paper*, 2012-01-0147, 2012.

[120] S.C. Kong, Y. Sun, and R. D. Reitz. Modeling Diesel Spray Flame Liftoff, Sooting Tendency, and NO_x Emissions Using Detailed Chemistry With Phenomenological Soot Model. *Journal of Engineering for Gas Turbines and Power*, 129:pp. 245–251, 2007.

[121] S. Som, D. E. Longman, Z. Luo, M. Plomer, and T. Lu. Three dimensional simulations of diesel sprays using n-dodecane as a surrogate. *Fall technical meeting of the eastern states section of the combustion institute*, 2011.

[122] M.A. Singer and S.B. Pope. Exploiting ISAT to solve the equations of reacting flow. *Combustion Theory and Modelling*, Vol. 8:pp. 361–383, 2004.

[123] F. Contino, H. Jeanmart, T. Lucchini, and Gianluca D'Errico. Coupling of in situ adaptive tabulation and dynamic adaptive chemistry: An effective method for solving combustion in engine simulations. *Proceedings of the Combustion Institute*, 33, 2011.

[124] M. Embouazza, D. C. Haworth, and N. Darabiha. Implementation of Detailed Chemical Mechanisms Into Multidimensional Cfd Using in Situ Adaptive Tabulation: Application to HCCI Engines. *SAE Paper*, 2002-01-2773, 2002.

[125] F. Contino, T. Lucchini, G. D'Errico, C. Duynslaegher, V. Dias, and H. Jeanmart. Simulations of advanced combustion modes using detailed chemistry combined with tabulation and mechanism reduction techniques. *SAE International Journal of Engines*, 5(2012-01-0145):185–196, 2012.

[126] M. S. Aceves, D. L. Flowers, C. K. Westbrook, J. R. Smith, W. Pitz, R. Dibble, M. Christensen, and B. Johansson. A multi-zone model for prediction of HCCI combustion and emissions. *SAE Paper*, 2000-01-0327, 2000.

[127] A Babajimopoulos, DN Assanis, DL Flowers, SM Aceves, and RP Hessel. A fully integrated cfd and multi-zone model with detailed chemical kinetics for the simulation of pcci engines. 15th international multidimensional engine modeling users' group meeting. *Detroit, MI, USA*, 2005.

[128] J. Reveillon and L. Vervisch. Spray vaporization in nonpremixed turbulent combustion modeling: a single droplet model. *Combustion and flame*, 121 no. 1:pp. 75–90, 2000.

[129] C. W. Hasse. A two-dimensional flamelet model for multiple injections in diesel engines. *PhD. Thesis*, Cuvillier Verlag, 2004.

[130] H. Barths, C. Hasse, and N. Peters. Computational fluid dynamics modelling of non-premixed combustion in direct injection diesel engines. *International Journal of Engine Research*, 1 (3):pp. 249–267, 2000.

[131] N. Peters. Laminar Flamelet Concepts in Turbulent Combustion. *21st Symposium on Combustion (Int)*, pages pp. 1231–1250, 1986.

[132] H. Pitsch, H. Barths, and N. Peters. Three-dimensional modeling of nox and soot formation in dl-diesel engines using detailed chemistry based on the interactive flamelet approach. *SAE transactions*, 105(4), 1996.

[133] N. Peters. Laminar diffusion flamelet models in non-premixed turbulent combustion. *Progress in energy and combustion science*, 01.07.1996-31.12.1996, 1997.

[134] T. Hellstrom. Rif implementation and testing. *Technical Report*, 10(3):319–339, 1984.

[135] H. Lehtiniemi, Y. Zhang, R. Rawat, and F. Mauss. Efficient 3-d cfd combustion modeling with transient flamelet models. *SAE technical paper*, 2008-01-0957, 2008.

[136] Baumgarten C. *Mixture formation in internal combustion engines*. Springer, 2006.

[137] Guiyang Zhang, Xinqi Qiao, Xuelong Miao, Jianhai Hong, and Jinbao Zheng. Effects of highly dispersed spray nozzle on fuel injection characteristics and emissions of heavy-duty diesel engine. *Fuel*, 102:666–673, 2012.

[138] Clément Chartier, Ulf Aronsson, Öivind Andersson, Rolf Egnell, and Bengt Johansson. Influence of jet–jet interactions on the lift-off length in an optical heavy-duty di diesel engine. *Fuel*, 112:311–318, 2013.

[139] J Li, WM Yang, H An, A Maghbouli, and SK Chou. Effects of piston bowl geometry on combustion and emission characteristics of biodiesel fueled diesel engines. *Fuel*, 120:66–73, 2014.

[140] C. L. Genzale, R. D. Reitz, and M. P. B. Musculus. Effects of Piston Bowl Geometry on Mixture Development and Late-Injection Low-Temperature Combustion in a Heavy-Duty Diesel Engine. *SAE Paper*, 2008-01-1330, 2008.

[141] Sung Wook Park. Optimization of combustion chamber geometry for stoichiometric diesel combustion using a micro genetic algorithm. *Fuel Processing Technology*, 91(11):1742–1752, 2010.

[142] Shengli Wei, Feihu Wang, Xianyin Leng, Xin Liu, and Kunpeng Ji. Numerical analysis on the effect of swirl ratios on swirl chamber combustion system of di diesel engines. *Energy Conversion and Management*, 75:184–190, 2013.

[143] Daniele Farrace, Michele Bolla, Yuri M Wright, and Konstantinos Boulouchos. Predicting in-cylinder soot in a heavy-duty diesel engine for variations in soi and tdc temperature using the conditional moment closure model. *SAE International Journal of Engines*, 6(2013-24-0016):1580–1593, 2013.

[144] Yusuke Imamori, Kenji Hiraoka, Shinsuke Murakami, Hiroyuki Endo, Christopher J Rutland, and Rolf D Reitz. Effect of mesh structure in the kiva-4 code with a less mesh dependent spray model for di diesel engine simulations. *SAE International Journal of Engines*, 2(2009-01-1937):1764–1776, 2009.

[145] Yuanhong Li, Qingluan Xue, Song-Charng Kong, Zheng Xu, Jianwen Yi, and David J Torres. Parallel computing of kiva-4 using adaptive mesh refinement. Technical report, SAE Technical Paper, 2009.

[146] Yuanhong Li and Song-Charng Kong. Integration of parallel computation and dynamic mesh refinement for transient spray simulation. *Computer Methods in Applied Mechanics and Engineering*, 198(17):1596–1608, 2009.

[147] Qingluan Xue and Song-Charng Kong. Development of adaptive mesh refinement scheme for engine spray simulations. *Computers & Fluids*, 38(4):939–949, 2009.

[148] Andreas M Lippert, Shengming Chang, Sasanka Are, and David P Schmidt. Mesh independence and adaptive mesh refinement for advanced engine spray simulations. Technical report, SAE Technical Paper, 2005.

[149] Ming Jia, Maozhao Xie, Tianyou Wang, and Zhijun Peng. The effect of injection timing and intake valve close timing on performance and emissions of diesel pcci engine with a full engine cycle cfd simulation. *Applied Energy*, 88(9):2967–2975, 2011.

[150] Ming Jia, Yaopeng Li, Maozhao Xie, and Tianyou Wang. Numerical evaluation of the potential of late intake valve closing strategy for diesel pcci (premixed charge compression ignition) engine in a wide speed and load range. *Energy*, 51:203–215, 2013.

[151] Rahul Jhavar and Christopher J Rutland. Effects of mixing on early injection diesel combustion. Technical report, SAE Technical Paper, 2005.

[152] Li Cao, Amit Bhave, Haiyun Su, Sebastian Mosbach, Markus Kraft, Antonis Dris, and Robert M McDavid. Influence of injection timing and piston bowl geometry on pcci combustion and emissions. *SAE International Journal of Engines*, 2(2009-01-1102):1019–1033, 2009.

[153] Wanhua Su and Haozhong Huang. Study of fuel distribution on diesel pcci combustion by development of a new characteristic-time combustion model. *SAE International Journal of Fuels and Lubricants*, 1(2008-01-1605):957–969, 2008.

[154] N. Nordin. *Complex Chemistry Modeling of Diesel Spray Combustion*. PhD thesis, Chalmers University of Technology, Department of Thermo Fluid Dynamics, 2001.

[155] Satbir Singh, Rolf D Reitz, and Mark P. B. Musculus. Comparison of the Characteristic Time (CTC), Representative Interactive Flamelet (RIF), and Direct Integration with Detailed Chemistry Combustion Models against Optical Diagnostic Data for Multi-Mode Combustion in a Heavy-Duty DI Diesel Engine. *SAE Paper*, 2003-01-0725, 2006.

[156] Satbir Singh, Rolf D Reitz, and Mark PB Musculus. 2-color thermometry experiments and high-speed imaging of multi-mode diesel engine combustion. Technical report, SAE Technical Paper, 2005.

[157] KY Huh and AD Gosman. A phenomenological model of diesel spray atomization. In *Proceedings of the international conference on multiphase flows*, volume 2, pages 515–518, 1991.

[158] R. D. Reitz. Modeling Atomization Processes In High Pressure Vaporizing Sprays. *Atomization and Spray Technology*, Vol. 3:pp. 309–337, 1987.

[159] GM Faeth. Mixing, transport and combustion in sprays. *Progress in Energy and Combustion Science*, 13(4):293–345, 1987.

[160] Neerav Abani, Achuth Munnannur, and Rolf D Reitz. Reduction of numerical parameter dependencies in diesel spray models. *Journal of Engineering for Gas Turbines and Power*, 130(3):032809, 2008.

[161] Caroline L Genzale, Rolf D Reitz, and Mark PB Musculus. Effects of spray targeting on mixture development and emissions formation in late-injection low-temperature heavy-duty diesel combustion. *Proceedings of the combustion institute*, 32(2):2767–2774, 2009.

[162] Caroline L Genzale, Rolf D Reitz, and Mark PB Musculus. Optical diagnostics and multi-dimensional modeling of spray targeting effects in late-injection low-temperature diesel combustion. *SAE International Journal of Engines*, 2(2009-01-2699):150–172, 2009.

[163] Eberhard Von Berg, Wilfried Edelbauer, Ales Alajbegovic, Reinhard Tatschl, Martin Volmajer, Breda Kegl, and Lionel C Ganippa. Coupled simulations of nozzle flow, primary fuel jet breakup, and spray formation. *Journal of engineering for gas turbines and power*, 127(4):897–908, 2005.

[164] N Mitroglou, M Gavaises, JM Nouri, and C Arcoumanis. Cavitation inside enlarged and real-size fully transparent injector nozzles and its effect on near nozzle spray formation. In *Proceedings of the DIPSI Workshop 2011. Droplet Impact Phenomena & Spray Investigations*, pages 33–45. Dip. Ingegneria industriale. Università degli studi di Bergamo, 2011.

[165] E v Berg, A Alajbegovic, D Greif, A Poredos, R Tatschl, E Winklhofer, and LC Ganippa. Primary break-up model for diesel jets based on locally resolved flow field in the injection hole. *Zaragoza*, 9:11, 2002.

[166] Lionel Christopher Ganippa, Göran Bark, Sven Andersson, and Jerzy Chomiak. Cavitation: a contributory factor in the transition from symmetric to asymmetric jets in cross-flow nozzles. *Experiments in Fluids*, 36(4):627–634, 2004.

[167] Ming Jia, Maozhao Xie, Hong Liu, Wei-Haur Lam, and Tianyou Wang. Numerical simulation of cavitation in the conical-spray nozzle for diesel premixed charge compression ignition engines. *Fuel*, 90(8):2652–2661, 2011.

[168] http://www.sandia.gov/ecn/index.php.

[169] Y. Pei, M. J. Davis, L. M. Pickett, and S. Som. Engine combustion network (ECN): global sensitivity analysis of Spray A for different combustion vessels. *Combustion and Flame*, 162:2337–2347, 2015.

[170] S. Ayyapureddi, U. Eguz, C. Bekdemir, L. M. T. Somers, and L. P. H. De Goey. Application of the FGM Method to Spray A Conditions of the ECN database. *In 12th Triennial international conference on liquid atomization and spray systems (ICLASS 2012), Heidelberg, Germany*, 2012.

[171] Y. Pei, E. R. Hawkes, S. Kook, G. M. Goldin, and T. Lu. Modelling n-dodecane spray and combustion with the transported probability density function method. *Combustion and Flame 162, no. 5*, pages pp. 2006–2019, 2015.

[172] S. Som, D. E. Longman, Z. Luo, M. Plomer, and T. Lu. Three dimensional simulations of diesel sprays using n-dodecane as a surrogate. *n Fall technical meeting of the eastern states section of the combustion institute*, 2011.

[173] Luo Zhaoyu, Sibendu Som, S. Mani Sarathy, Max Plomer, William J. Pitz, Douglas E. Longman, and Tianfeng Lu. Development and validation of an n-dodecane skeletal mechanism for spray combustion applications. *Combustion theory and modelling*, 18. no. 2:187–203, 2014.

[174] Brian Higgins, Dennis L Siebers, and Allen Aradi. Diesel-spray ignition and premixed-burn behavior. Technical report, SAE Technical Paper, 2000.

[175] Peter M Lillo, Lyle M Pickett, Helena Persson, Oivind Andersson, and Sanghoon Kook. Diesel spray ignition detection and spatial/temporal correction. *SAE International Journal of Engines*, 5(2012-01-1239):1330–1346, 2012.

[176] Dennis L. Siebers and B. Higgins. Flame lift-off on direct-injection diesel sprays under quiescent conditions. *SAE Technical Paper 2001-01-0530*, 2001.

[177] T. Yao, Y. Pei, B.J. Zhong, S. Som, and T. Lu. A Hybrid mechanism for n-dodecane combustion with optimized low-temperature chemistry. *9th US National Combustion Meeting. Cincinnati. OH*, 114IC-0055, 2015.

[178] Chemistry Department of Politecnico di Milano. http://www.chem.polimi.it.

[179] Pickett Lyle M., Caroline L. Genzale, Gilles Bruneaux, Louis-Marie Malbec, Laurent Hermant, Caspar Ask Christiansen, and Jesper Schramm. Comparison of diesel spray combustion in different high-temperature, high-pressure facilities. *SAE International Journal of Engines 3. no. 2*, pages 156–181, 2010.

[180] Pickett Lyle M., Julien Manin, Caroline L. Genzale, Dennis L. Siebers, Mark PB Musculus, and Cherian A. Idicheria. Relationship between diesel fuel spray vapor penetration/dispersion and local fuel mixture fraction. *SAE International Journal of Engines 4. no. 2011-01-0686*, pages 764–799, 2011.

[181] M. Maarten, B. Somers, J. Johnson, J. Naber, S. Lee, L. M. Malbec, and G. Bruneaux et al. Engine Combustion Network (ECN): Characterization and comparison of boundary conditions for different combustion vessels. *Atomization and Sprays*, 22, 2012.

[182] M. Bardi, R. Payri, L. M. Malbec, G. Bruneaux, L. M. Pickett, J. Manin, T. Bazyn, and Caroline Genzale. Engine combustion network: comparison of spray development, vaporization, and combustion in different combustion vessels. *Atomization and Sprays*, 22, 2012.

[183] G. D'Errico, T. Lucchini, S. Merola, and C. Tornatore. Application of a thermodynamic model with a complex chemistry to a cycle resolved knock prediction on a spark ignition optical engine. *International Journal of Automotive Technology*, Vol. 13(3):389–399, 2012.

[184] F. J. Salvador, J. Gimeno, J. M. Pastor, and Marti-Aldarav. Effect of turbulence model and inlet boundary condition on the Diesel spray behavior simulated by an Eulerian Spray Atomization (ESA) model. *International Journal of Multiphase Flow*, 65, 2014.

[185] W. E. Eagle, L. M. Malbec, and M. P. B. Musculus. Measurements of liquid length, vapor penetration, ignition delay, and flame lift-off length for the Engine Combustion Network 'Spray B' in a 2.34L Optical Heavy-Duty Diesel Engine. *SAE paper*, 2016-01-0743, 2016.

[186] M. P. B. Musculus. Multiple simultaneous optical diagnostic imaging of early-injection low-temperature combustion in a heavy-duty diesel engine. *SAE Paper*, 2006-01-0079, 2006.

[187] SANDIA Engine Combustion Network. sandia.gov/ecn/cvdata/expdiag/liqlenspraya.php, 2015.

[188] Lyle M. Pickett, Caroline L. Genzale, Julien Manin, Louis-Marie Malbec, and Laurent Hermant. Measurement uncertainty of liquid penetration in evaporating diesel sprays. *ILASS Americas, 23rd Annual Conference on Liquid Atomization and Spray Systems*, 2011.

[189] Dennis L. Siebers. Scaling liquid-phase fuel penetration in diesel sprays based on mixing-limited vaporization. *SAE Technical Paper 1999-01-0528*, 1999.

[190] Jeffrey Naber and Dennis L. Siebers. Effects of gas density and vaporization on penetration and dispersion of diesel sprays. *SAE Technical Paper 960034*, 1996.

[191] J. B. Heywood. *Internal Combustion Engine Fundamentals*. McGraw-Hill, 1988.

[192] B. Higgins and Dennis L. Siebers. Measurement of the flame lift-off location on di diesel sprays using oh chemiluminescence. *SAE Technical Paper 2001-01-0918*, 2001.

[193] T. Lucchini, A. Della Torre, G. D'Errico, G. Montenegro, M. Fiocco, and A. Maghbouli. Automatic Mesh Generation for CFD Simulations of Direct-Injection Engines. *SAE Paper*, 2015-01-0376, 2015.

[194] K. Y. Huh, I. P. Chang, and J. K. Martin. A comparison of boundary layer treatments for heat transfer in IC engines. *SAE Paper*, 900252, 1990.

[195] E.R. Hawkes. Engine combustion network workshop two: Ignition and lift-off session, 2012.

[196] E. Mastorakos, T. A. Baritaud, and T. J. Poinsot. Numerical simulations of autoignition in turbulent mixing flows. *Combustion and Flame*, 109(1):198–223, 1997.

[197] G. D'Errico, T. Lucchini, A. Onorati, and G. Hardy. Computational fluid dynamics modeling of combustion in heavy-duty diesel engines. *International Journal of Engine Research*, 1468087414561276, 2014.

[198] Robert H Thring. Homogeneous-charge compression-ignition (hcci) engines. Technical report, SAE Technical paper, 1989.

[199] Rudolf H Stanglmaier and Charles E Roberts. Homogeneous charge compression ignition (hcci): benefits, compromises, and future engine applications. Technical report, SAE Technical Paper, 1999.

[200] Ali Yousefzadi Nobakht, R Khoshbakhi Saray, and Arash Rahimi. A parametric study on natural gas fueled hcci combustion engine using a multi-zone combustion model. *Fuel*, 90(4):1508–1514, 2011.

[201] Derek A Splitter, Reed M Hanson, Rolf D Reitz, Vittorio Manente, Bengt Johansson, et al. Modeling charge preparation and combustion in diesel fuel, ethanol, and dual-fuel pcci engines. *Atomization and Sprays*, 21(2), 2011.

[202] Ali Mohammadi, Hiroshi Kawanabe, Takuji Ishiyama, Masahiro Shioji, and Atsushi Komada. Study on combustion control in natural-gas pcci engines with ozone addition into intake gas. Technical report, SAE Technical Paper, 2006.

[203] Taro Aoyama, Yoshiaki Hattori, Jun'ichi Mizuta, and Yasuo Sato. An experimental study on premixed-charge compression ignition gasoline engine. Technical report, SAE Technical paper, 1996.

[204] Vittorio Manente, Bengt Johansson, and Per Tunestal. Partially premixed combustion at high load using gasoline and ethanol, a comparison with diesel. Technical report, SAE Technical Paper, 2009.

[205] Christof Noehre, Magnus Andersson, Bengt Johansson, and Anders Hultqvist. Characterization of partially premixed combustion. Technical report, SAE Technical Paper, 2006.

[206] Duksang Kim, Isaac Ekoto, William F Colban, and Paul C Miles. In-cylinder co and uhc imaging in a light-duty diesel engine during ppci low-temperature combustion. *SAE International Journal of Fuels and Lubricants*, 1(2008-01-1602):933–956, 2008.

[207] Fan Zhang, Hongming Xu, Jun Zhang, Guohong Tian, and Gautam Kalghatgi. Investigation into light duty dieseline fuelled partially-premixed compression ignition engine. *SAE International Journal of Engines*, 4(2011-01-1411):2124–2134, 2011.

[208] M Alperstein, WB Swim, and PH Schweitzer. Fumigation kills smoke–improves diesel performance. Technical report, SAE Technical Paper, 1958.

[209] Shigeru Onishi, Souk Hong Jo, Katsuji Shoda, Pan Do Jo, and Satoshi Kato. Active thermo-atmosphere combustion (atac)-a new combustion process for internal combustion engines. Technical report, SAE Technical paper, 1979.

[210] Masaaki Noguchi, Yukiyasu Tanaka, Taro Tanaka, and Yukihisa Takeuchi. A study on gasoline engine combustion by observation of intermediate reactive products during combustion. Technical report, SAE Technical Paper, 1979.

[211] Paul M Najt and David E Foster. Compression-ignited homogeneous charge combustion. Technical report, SAE Technical paper, 1983.

[212] Randy P Hessel, David E Foster, Salvador M Aceves, M Lee Davisson, Francisco Espinosa-Loza, Daniel L Flowers, William J Pitz, John E Dec, Magnus Sjöberg, and Aristotelis Babajimopoulos. Modeling iso-octane hcci using cfd with multi-zone detailed chemistry; comparison to detailed speciation data over a range of lean equivalence ratios. Technical Report 2008-01-0047, SAE Technical Paper, 2008.

[213] J. Warnatz, U. Maas, and R. W. Dibble. *Combustion*. Springer Verlag, 2000.

[214] A Yousefzadi Nobakht, R Khoshbakhi Saray, and G Soleimani Astiar. Optimization of gri-mech 3.0 mechanism using hcci combustion models and genetic algorithm. *International Journal of Engineering, Transactions A: Basics*, 24(2):155–168, 2011.

[215] J. Wallesten and V. Golovitchev. Detailed Chemistry Laminar Flame Speed Calculations for Iso-Octane-Air Mixtures. *Internal Report 02/03, Department of Thermo and Fluid Dynamics, Chalmers University of Technology*, 2002.

[216] Mohammad Izadi Najafabadi, Nico Dam, Bart Somers, and Bengt Johansson. Ignition sensitivity study of partially premixed combustion by using shadowgraphy and oh* chemiluminescence methods. Technical report, SAE Technical Paper, 2016.

[217] Yao-Dong Liu, Ming Jia, Mao-Zhao Xie, and Bin Pang. Enhancement on a skeletal kinetic model for primary reference fuel oxidation by using a semidecoupling methodology. *Energy & Fuels*, 26(12):7069–7083, 2012.

[218] Pinaki Pal, SeungHwan Keum, and Hong G Im. Assessment of flamelet versus multi-zone combustion modeling approaches for stratified-charge compression ignition engines. *International Journal of Engine Research*, 17(3):280–290, 2016.

[219] Yuanjiang Pei, Evatt R Hawkes, Michele Bolla, Sanghoon Kook, Graham M Goldin, Yue Yang, Stephen B Pope, and Sibendu Som. An analysis of the structure of an n-dodecane spray flame using tpdf modelling. *Combustion and Flame*, 168:420–435, 2016.

[220] RW Bilger. Conditional moment closure for turbulent reacting flow. *Physics of Fluids A: Fluid Dynamics (1989-1993)*, 5(2):436–444, 1993.

[221] Alex Y Klimenko and Robert William Bilger. Conditional moment closure for turbulent combustion. *Progress in energy and combustion science*, 25(6):595–687, 1999.

[222] G Kim, S Kang, Y Kim, RW Bilger, and MJ Cleary. Conditional moment closure and transient flamelet modelling for detailed structure and no x formation characteristics of turbulent nonpremixed jet and recirculating flames. *Combustion Theory and Modelling*, 11(4):527–552, 2007.

[223] A Yu Klimenko and SB Pope. The modeling of turbulent reactive flows based on multiple mapping conditioning. *Physics of Fluids (1994-present)*, 15(7):1907–1925, 2003.

[224] MJ Cleary, AY Klimenko, J Janicka, and M Pfitzner. A sparse-lagrangian multiple mapping conditioning model for turbulent diffusion flames. *Proceedings of the Combustion Institute*, 32(1):1499–1507, 2009.

[225] Fatemeh Salehi, Matthew J Cleary, and Assaad R Masri. A sensitivity analysis for sparse-lagrangian mmc in simulations of a n-dodecane reacting jet. Technical report, SAE Technical Paper, 2016.